Electromagnetic Field Sensing with Rydberg Atoms in Vapor Cells

by

Lu Ma

A dissertation submitted in partial fulfillment
of the requirements for the degree of
Doctor of Philosophy
(Physics)
in the University of Michigan
2021

Doctoral Committee:

Professor Georg Raithel, Chair
Professor Paul Berman
Professor Timothy Chupp
Professor Lu Li
Professor Stephen Rand

Lu Ma

lukema@umich.edu

ORCID iD: 0000-0002-4396-098X

This work is dedicated to my grandparents,
for their unconditional love and
the wonderful memories they left for me.

Acknowledgments

I have often dreamed about the moment I will earn my degree and how thrilling it will be. Now, the time has truly come. But I am not as excited as I had imagined before. It is not because the COVID-19 pandemic has forced us to exercise the whole procedures online and I had to talk to a computer screen alone in my apartment, not to mention miss the hot coffees and delicate snacks for friends, colleagues and committee members. I am less exhilarated because it strikes me that this moment is not all about my own endeavors or the success to earn the degree. It becomes increasingly clear to me that, to get to this point, I am actually in debt to many people for their help and support. Unfortunately, to some of them, I will not even get a chance to pay back forever.

I would like to take the opportunity here to express my gratitude to the instructors and professors who generously carried me along the journey of learning science and researching in physics. Without their commitment to nourishing young minds, I certainly won't be here to write this dissertation. Among all of them, I'd like to specially thank my Phd advisor and mentor, Professor Georg Raithel. It is Prof. Raithel who introduced me to the wonderful lands of Rydberg physics and it is him who looked after my intellectual growth. His irradiant knowledge and enthusiasm let me believe that learning a small amount everyday will make a difference in a most unexpected way. Just as he always says "Pay attention to details and never give up".

Last but not least, I also owe a great deal to my family for their unwavering support and love. I hope I have not let them down so far. In addition to my parent, I would like to thank my wife, Dr. Lu Chen, who I met during the darkest days when I was pursuing this degree. Her kindness and understanding are beacons that always light my path when encouragement and confidence are so desperately needed. I look forward a wonderful marriage and an exciting life together with you.

TABLE OF CONTENTS

LIST OF FIGURES

LIST OF TABLES

LIST OF APPENDICES

ABSTRACT

Research of hot atomic vapor systems has a long history. In the 1930s, Rydberg spectral lines were measured in hot gases and later published in *II Nuovo Cimento* by Edoardo Amaldi and Emilio Gino Segrè. Recently, much-improved technologies, such as lasers, microwaves and digital/analog control systems, have led to exciting progress in this reviving field. Due to its cryogenic-free and vacuum-free deployment potential, room-temperature and quantum-enabled sensing devices using gaseous atoms have become a popular research topic, and engineering such devices has received considerable attention. Proof-of-principle experiments have been performed demonstrating new ideas such as atomic-optical clocks, quantum-enhanced motion sensors, next-generation magnetometers, Rydberg enabled microwave sensors, single photon optical switches, quantum memories, etc.

This thesis focuses on my work related to electromagnetic-field sensing using Rydberg atoms in vapor cells, where Rydberg atoms are excited and detected by electromagnetically induced transparency (EIT) spectroscopy. I first investigate the detection of strong magnetic fields ($\sim$ 1 T) in the Paschen-Back regime. The diamagnetic (quadratic) response of the Rydberg levels makes the atoms sensitive to small fluctuations in field strength on a large background. By implementing an isotope-mixed cell, we demonstrate accurate measurement of a field near 0.7 T with a relative uncertainty of $\pm 0.12\%$.

Many Rydberg-enabled radio frequency (RF) and microwave (MW) sensing applications require a capability of zeroing or intentional tuning of small DC electric fields inside the vapor cell. For this purpose, I explore an in-situ DC electric-field sensing and tuning method without using any bulk or thin film electrodes. I find that the photoelectric effect on the vapor cell walls (with invisible, atomic Rb aggregate layers covering the surfaces) can generate tuning fields up to 0.8 V/cm, with an inhomogeneity of about 2%. The spatial

distribution of these fields can be directly monitored by quadratic Stark shifts of the Rydberg atoms. This work may inspire new approaches for DC-field control in miniaturized, metal-free atomic vapor-cell devices.

Like many other quantum measurements on hot gaseous samples, short interaction time and other technical decoherence processes are the major factors which limit the precision and, in certain cases, the accuracy of the metrological results. In order to study these effects in the context of EIT, I performed an EIT experiment using a Λ-type quantum system consisting of the hyperfine ground states and the first excited electronic state of the Rb atoms contained in a buffer-gas-free thermal vapor cell without anti-relaxation coating. Technical line-broadening effects due to inhomogeneity of stray magnetic fields, laser frequency jitter, transverse beam intensity distribution, interaction time distribution, and atom-wall/impurity gas collisions are studied. Experimental results and numerical simulations are compared. These results provide crucial information and quantitative insights for vapor cell sensor design.

The development of compact and multi-functional spectroscopy vapor cells is widely considered to be a critical engineering step towards manufacturing field-deployable sensors for real life applications. My R&D efforts towards fabrication of glass spectroscopy cells with integrated, highly-conductive silicon components are presented in the last part of my thesis. I explored various technical challenges and successfully developed a proof-of-principle prototype from scratch. The device allows the application of electric fields inside the cell for particle trapping and for tuning Rydberg transitions. Further, the highly-conductive silicon components enable microwave polarization filtering for microwave sensing applications, plasma-physics studies, etc. Preliminary experimental data and simulations are presented. Technical details are included for future reference.

In summary, in my thesis I report on a comprehensive study of several spectroscopic and field sensing applications of Rydberg and ground-state atoms in vapor cells, as well as forays into novel methods to engineer vapor cells with embedded electrodes.

CHAPTER 1

Introduction

This thesis focuses on my work related to electromagnetic-field sensing using Rydberg atoms [1] in vapor cells. Signals from the Rydberg atoms in the gas phase are detected by the method of electromagnetically induced transparency (EIT) spectroscopy [2, 3]. EIT has been implemented in both cold atomic gases [4, 5] and in room-temperature vapor cells [3, 6] as a nondestructive optical detection technique for Rydberg-atom spectroscopy.

In the first chapter, for the broad interest of general readers, I start with an introduction to two sensing technologies using atomic vapor cells. Next, I introduce three frequently encountered unique aspects with regard to performing Rydberg-EIT spectroscopy in a gaseous sample.

In Chapters 2–3, I present some important experimental and theoretical findings that have accumulated over years of Rydberg physics research. This knowledge of Rydberg physics enables us to make accurate and quantitative calculations about the quantum properties of Rydberg atoms. These calculations are the bedrock for establishing realistic semi-classical simulations for various sensing applications.

Chapters 4–7 of this thesis focus on the reviews of four major research activities throughout my PhD training. Details about the designs and technical approaches are documented for future reference. Experimental findings are also presented and discussed. For completeness, some details are provided in an appendix.

1.1 Metrology Using Atomic Vapor Cells

Light-matter quantum-state entanglement and manipulation have been a research focus in the condensed-matter and AMO community for many years [7, 8]. Since the invention of laser cooling and trapping technologies, a majority of the research efforts have been focused on cold atomic systems. This is partially due to the availability of prolonged interaction times in these systems and the wide range of quantum physics phenomena that

can be studied. The success of coherently preparing and precisely manipulating physical systems at a quantum level [9, 10, 11, 12] has led us to the dawn of a new era for applications based on laws of quantum mechanics. These applications range from fundamental quantum-based sensors [13, 14, 15, 16, 17] and transducers [18, 19, 20] to higher-level quantum networks [21] suitable for quantum communications, quantum simulation and computing [22, 23, 24].

In contrast to a laser-cooled atomic sample, the atoms in a gaseous vapor phase cover a wide range of Doppler shifts and possess a short interaction time with the external fields. However, these features do not limit them to finding their way into the metrology applications that require high sensitivity and high precision. For readers with a broad interest, I begin by introducing two metrology technologies that involve hot atomic vapors contained in room-temperature spectroscopy cells.

1.1.1 Vapor Cell Magnetometers

The first example I would like to discus is optical magnetometers. These devices are capable of sensing magnetic fields by measuring the optical absorptive and dispersive properties of atoms. The sensitivity is on the order of 10^{-15} T Hz$^{-1/2}$ for some of the state-of-the-art devices. The idea of using atoms as magnetometers has a history of nearly half a century since the discovery of optical pumping. Glass vapor cells filled with alkali and/or noble gases are implemented in these devices. Information about the magnetic fields is encoded in the atoms' spin motions in the fields.

There are numerous techniques for measuring atomic spin. One commonly used method is measuring the optical rotation of the light that propagates through the vapor. This technique is also known as optical polarimetry. For devices involving Alkali atoms, light with wavelengths close to the D1 or D2 transitions is widely used [25].

Like many other quantum measurements, the sensitivity of the vapor cell magnetometers is limited by spin relaxations. Various physical processes affect the relaxation of the spin in both the transverse direction (T2 type) and the longitudinal direction (T1 type). They include but are not limited to spin-destruction collisions among alkali, buffer-gas and quenching-gas atoms, wall collisions, spin-exchange collisions, and magnetic field gradient-induced dephasing, etc.

In addition to these technical processes which limit the sensitivity, there are three fundamental sources of noises that limit the signal-to-noise ratio [26]. These noises originate from the quantum nature of the system. First, the finite number of atoms involved in each measurement gives rise to the spin-projection noise [27]. Second, photon shot noise is

ubiquitous in all atom-light interactions. Third, the light-shift noise [28] produced by the AC Stark shifts fluctuations, constitutes the last fundamental quantum noise. A detailed pedagogical summary of these noise effects can be found in Ref. [25].

Despite these fundamental limits, there have been tremendous developments in atomic magnetometers over the last decade. These advances are driven by the technological improvements in measuring equipment and by refinements in producing better quality vapor cells. New cell technologies are essential to prolonging the ground-state relaxation times. State-of-the-art atomic magnetometers (spin-exchange relaxation-free (SERF)) have achieved sensitivities that rival or even surpass the superconducting quantum interference device (SQUID)-based magnetometers [29, 27] not to mention their intrinsic advantage of cryogenic-free operation conditions.

1.1.2 Rydberg-atom Enabled RF/Microwave Sensing

The second example I would like to introduce has a relatively short history, where hot Rydberg atoms are used as atomic sensors for radio frequency (RF)/microwave (MW) electric fields [14]. The Rydberg atoms are prepared and detected using EIT spectroscopy. The RF/MW electric fields couple a nearby Rydberg state and cause transitions out of the EIT system. Since the EIT signals are sensitive to disturbances, such as phase modulation, population modulation, or energy shifts, we can detect the amplitude and phase of the RF/MW by comparing the EIT signals with and without RF/MW [30, 31].

In a relatively strong RF/MW field, EIT signals show Autler-Townes splittings. The amount of the splitting is directly proportional to the field amplitude. This spectrospic information can be used to measure the RF/MW fields strength. For small field strengths where the Autler-Townes splittings are smaller than the EIT signal width, a heterodyne-sensing technique has been demonstrated. By using a strong microwave-dressed Rydberg state researchers have achieved a sensitivity at a level of tens of $\mathrm{nVcm^{-1}Hz^{-1/2}}$ [15].

In addition to its high sensitivity, Rydberg EIT has also been shown to be robust against white noise inherent in any RF/MW sources [32]. Researchers even made a radio using this technique [33].

Due to the well-developed understanding of Rydberg physics, Rydberg EIT in room-temperature vapor cells has been considered as a new atom-based, SI-traceable and self-calibrated method for an RF/MW measurement standard [14].

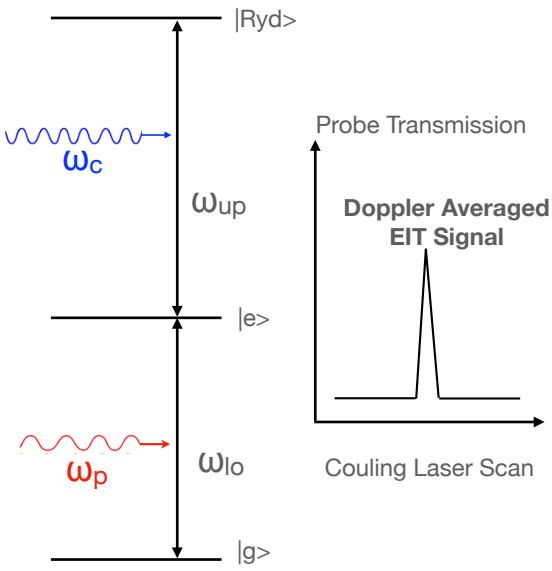

Figure 1.1: Simplified three-level ladder structure for a Rydberg EIT system. ω_p and ω_c represent the angular frequencies of the probe laser and coupling laser, respectively. The energy difference between state $|g\rangle$ and $|e\rangle$ is $\hbar\omega_{lo}$. The energy difference between state $|e\rangle$ and $|Ryd\rangle$ is $\hbar\omega_{up}$. A transmission increase of the probe laser can be observed when the two-photon resonance condition is met (see text for details).

1.2 Doppler Effect in a Wavelength Mismatched Ladder System

Unlike cold atomic systems where atoms are cooled to below sub-mK temperatures, the average velocity of the atoms in a room-temperature spectroscopy cell is usually up to about five orders of magnitude larger than that of cold atoms. In addition to the much larger average velocity, the width of the velocity distribution is also wider than that of laser-cooled atoms by the same factor. This wide distribution, together with the Doppler shifts, brings both challenges and opportunities for performing EIT spectroscopy which requires a coherent and nonlinear optical excitation [34, 35].

In the next three subsections, I would like to emphasize three unique effects related to fast-moving atoms in the context of the Rydberg EIT ladder system. Some of them are not intuitively apparent, but all play important roles in analyzing and understanding spectroscopic signals.

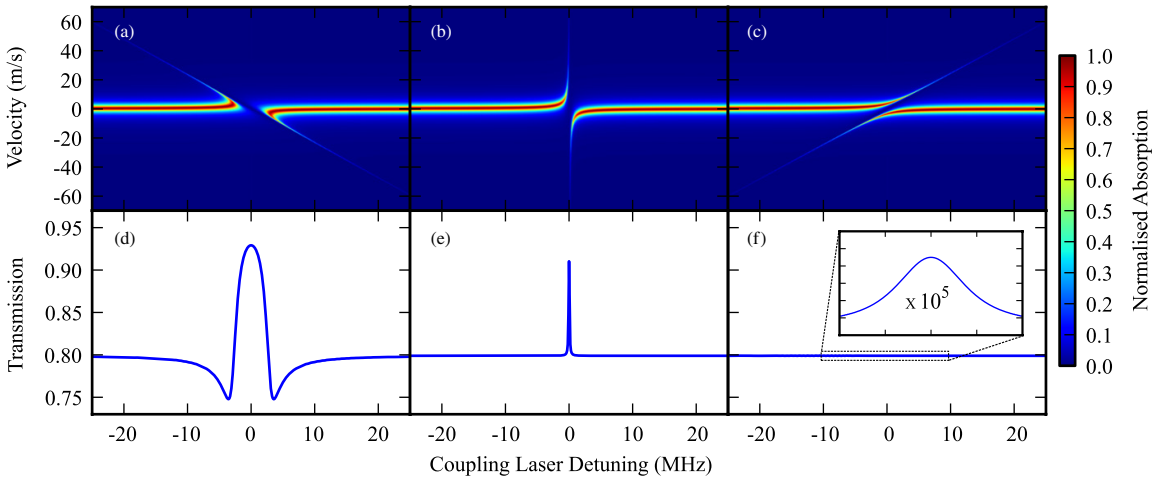

Figure 1.2: Adapted from Ref. [36].Wavelength dependence of the EIT. Top: absorption coefficient per velocity class for (a) $\lambda_p = \frac{4}{3}\lambda_c$ ($\lambda_p > \lambda_c$), (b) $\lambda_p = \lambda_c$ and (c) $\lambda_p = \frac{2}{3}\lambda_c$ ($\lambda_p < \lambda_c$). Bottom (d)–(f): Doppler-averaged probe laser transmission signal corresponding to (a)–(c).

1.2.1 Signal Strength and Doppler Averaging

A Rydberg-EIT system can be simplified to a three-level ladder structure, as shown in Fig. 1.1. A Rydberg atom in the state $|Ryd\rangle$ is coupled by the two-photon coherent excitation scheme where the probe laser couples the ground $|g\rangle$ and the short-lived intermediate state $|e\rangle$, and the coupling laser couples $|e\rangle$ to the relatively long-lived Rydberg state $|Ryd\rangle$. Both probe laser angular frequency, ω_p, and coupling laser angular frequency, ω_c, can be tuned independently. In most of the Rydberg EIT experiments, one of the two laser frequencies are fixed and the other is scanned. The EIT happens when the probe and coupling laser frequencies satisfy the two-photon resonance condition shown in Eq. 1.1:

$$(\omega_c + \boldsymbol{v} \cdot \boldsymbol{k}_c) + (\omega_p + \boldsymbol{v} \cdot \boldsymbol{k}_p) = \omega_{up} + \omega_{lo} \tag{1.1}$$

where $\boldsymbol{k}_c$ and $\boldsymbol{k}_p$ are the wave vectors of the probe and coupling lasers. The $\boldsymbol{v} \cdot \boldsymbol{k}$ terms account for the Doppler shifts.

In thermal experiments, both probe and coupling laser frequencies are tuned to be near-resonant, i.e., $\omega_p \approx \omega_{lo}$ and $\omega_c \approx \omega_{up}$. Under such a condition, Eq. 1.1 dictates that the probe and the coupling laser have to propagate in opposite directions in order to cancel out most of the Doppler-shift mismatch when k_p and k_c differ significantly. For the case of Rb, probe laser wavelength $\lambda_p \approx 780$nm and coupling laser wavelength $\lambda_c \approx 480$nm are commonly used. This geometrical requirement on the excitation scheme can be drastically relaxed in cold atom experiments due to the fact that $\boldsymbol{v} \approx 0$.

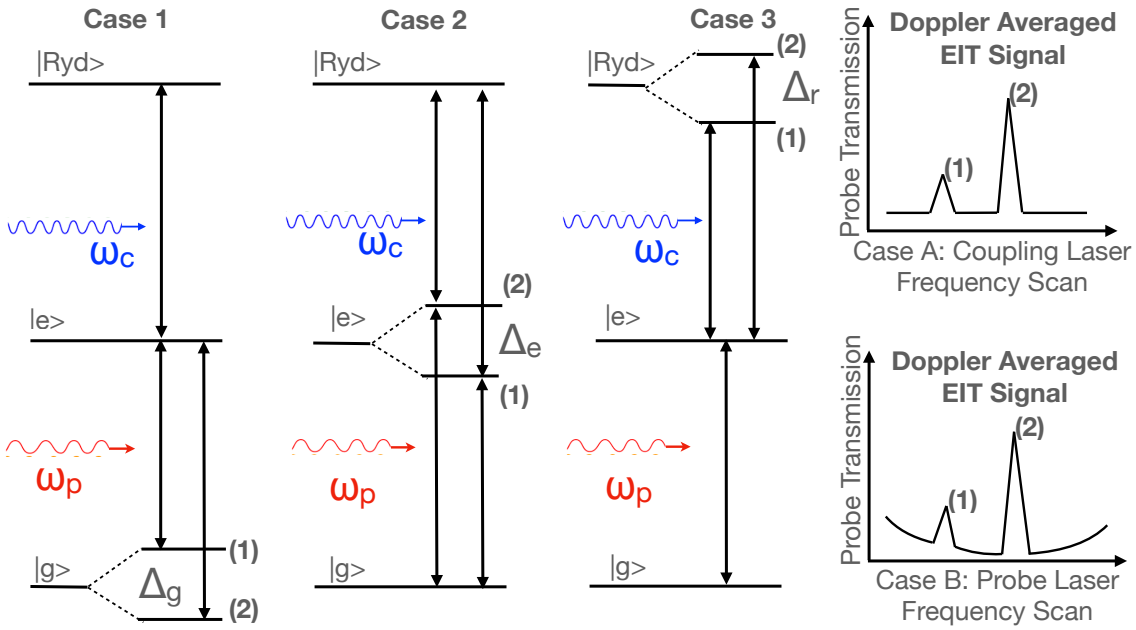

Figure 1.3: Illustration of a toy model where two EIT resonances are observed due to sub-level splitting/shift of ground state $|g\rangle$ (Case 1), intermediate state $|e\rangle$ (Case 2) or Rydberg state $|e\rangle$ (Case 3). Two laser scan configurations (Case A and Case B; see text for details) are shown on the right. Resonance (1) is assigned to the signal on the red-detuning side of the resonance (2) in both cases. Note that in Case 1, resonance (1) is associated with the upper level in the ground state manifolds, whereas in Cases 2 and 3, it is associated with the lower level in the respective manifolds.

In addition, due to the wide distribution of $\boldsymbol{v}$, the resonant laser frequencies satisfying Eq. 1.1 are different for atoms of different velocity. The measurable transmission signal of the probe laser has to be averaged over the entire ensemble of atoms of all possible velocities. Depending on the probe and coupling laser wavelengths, such an averaging process (reffered as Doppler averaging) has a dramatic effect on the EIT signal strength. Fig. 1.2 compares the EIT signal strengths for cases in which the wavelength of the two transitions are mismatched. The signal strength is reduced significantly when the one-photon Doppler shift $\Delta_{1ph} = k_p v_z$ has the same sign as the two-photon Doppler shift $\Delta_{2ph} = (k_p - k_c)v_z$.

1.2.2 Frequency Scaling Factors for Measured Resonances

For detecting of electromagnetic fields, Rydberg-EIT line shifts or splittings are usually measured. Due to the wavelength mismatch, these measured shifts/splittings do not directly correspond to the energy shifts/splittings of the underlying quantum states. The measured

shifts/splittings need to be scaled before they can be used to find the correct electromagnetic field strength.

In addition, the energy-level structures of real atoms are more complicated than those of a three-level system. Even in zero electromagnetic fields, spin-orbit couplings in the Rydberg state $|Ryd\rangle$ and hyperfine structures of the intermediate state $|e\rangle$ cause splittings of the EIT resonance. Multiple EIT resonances can usually be observed within the frequency scan range of a laser. Each of these is associated with a sub-three-level structure for a specific velocity group that satisfies the resonance condition shown in Eq. 1.2 and Eq. 1.3:

$$\omega_c - \omega_{up} + \frac{v_z}{c}\omega_c = 0 \tag{1.2}$$

$$\omega_p - \omega_{lo} - \frac{v_z}{c}\omega_p = 0 \tag{1.3}$$

where $\hbar\omega_{lo}$in this case represents the energy difference between two lower states in the sub-three-level structure and $\hbar\omega_{up}$ represents the energy difference between the upper two states. The sign difference of the Doppler terms is due to the fact that the probe and coupling laser propagate in opposite directions along the z-axis.

The scaling factors can be derived from Eq. 1.2 and Eq. 1.3. Let us consider a toy model where only two EIT resonances are present. As shown in Fig. 1.3, the two resonances can be associated with either the subatomic structures of the ground state $|g\rangle$ (e.g., Zeeman splitting/shifts of the magnetic sub-levels), of the intermediate state $|e\rangle$ (e.g.,hyperfine structure splittings) or of the Rydberg state $|Ryd\rangle$ (e.g., fine structure splittings or Stark shifts).

More interestingly, it turns out that these scaling factors take different values depending on which one of the two lasers is scanning. In Case A, the probe laser frequency is fixed, and the coupling laser frequency scans. In Case B, the probe laser frequency scans, and the coupling laser frequency is fixed. These scaling factors are summarized in Tab. 1.1 and are derived in the following:

In Case A, it is helpful to rewrite Eq. 1.2 and Eq. 1.3 as follows:

$$\omega_c^{(*)} = \omega_{up}^{(*)} - \frac{v_z^{(*)}}{c}\omega_c^{(*)} \tag{1.4}$$

$$\frac{v_z^{(*)}}{c} = \left(\omega_p - \omega_{lo}^{(*)}\right)\frac{1}{\omega_p} \tag{1.5}$$

where superscript $(*) = (1)$ or (2) has been added to reflect the two adjacent resonances as

Table 1.1: EIT resonance frequency scaling factors in a wavelength-mismatched ladder system

	Ground Sate Case 1	Intermediate State Case 2	Rydberg State Case 3
Case A (probe fixed, coupling scans)	$\frac{\lambda_p}{\lambda_c}$	$1-\frac{\lambda_p}{\lambda_c}$	1
Case B (probe scans, coupling fixed)	1	$1-\frac{\lambda_c}{\lambda_p}$	$\frac{\lambda_c}{\lambda_p}$

shown in Fig. 1.3.

After substituting Eq. 1.5 into Eq. 1.4, the coupling laser frequency tuning $\Delta^{(1,2)}\omega_c$ needed, moving from resonance 1 to resonance 2, can be found as

$$\begin{aligned}
\Delta^{(1,2)}\omega_c &= \omega_c^{(1)} - \omega_c^{(2)} \\
&= \left[\omega_{up}^{(1)} - \omega_{up}^{(2)}\right] - \left[\left(\omega_p - \omega_{lo}^{(1)}\right)\frac{\omega_c^{(1)}}{\omega_p} - \left(\omega_p - \omega_{lo}^{(2)}\right)\frac{\omega_c^{(2)}}{\omega_p}\right] \\
&= \begin{cases} \left[\omega_{lo}^{(1)} - \omega_{lo}^{(2)}\right]\frac{\lambda_p}{\lambda_c} = -\Delta_g\frac{\lambda_p}{\lambda_c} & \text{case A1} \\ \left[\omega_{up}^{(1)} - \omega_{up}^{(2)}\right] + \left[\omega_{lo}^{(1)} - \omega_{lo}^{(2)}\right]\frac{\lambda_p}{\lambda_c} = \Delta_e\left(1-\frac{\lambda_p}{\lambda_c}\right) & \text{case A2} \\ \left[\omega_{up}^{(1)} - \omega_{up}^{(2)}\right] = -\Delta_r & \text{case A3} \end{cases}
\end{aligned} \tag{1.6}$$

where Δ_g is the ground state splitting in Case A1, Δ_e is the intermediate state splitting and Δ_r is the Rydberg splitting in Case A2 and A3. Note that the splittings either caused by fine or hyperfine interaction or external magnetic fields are, in general, much less than ω_p, and therefore, the following approximation has been used in the last step of Eq. 1.6:

$$\frac{\omega_c^{(1)}}{\omega_p} \simeq \frac{\omega_c^{(2)}}{\omega_p} \simeq \frac{\lambda_p}{\lambda_c} \tag{1.7}$$

In Case B, the probe laser is scanning and the coupling laser frequency is held fixed. It is convenient to rewrite Eq. 1.2 and Eq. 1.3 as

$$\frac{v_z^{(*)}}{c} = -\left(\omega_c - \omega_{up}^{(*)}\right)\frac{1}{\omega_c} \tag{1.8}$$

$$\omega_p^{(*)} = \omega_{lo}^{(*)} + \frac{v_z^{(*)}}{c}\omega_p^{(*)} \tag{1.9}$$

Similar to Case A, after substituting Eq. 1.8 in Eq. 1.9 the frequency tuning $\Delta^{(1,2)}\omega_p$ of the probe laser needed, moving from resonance 1 to resonance 2, can be found to be:

$$\begin{aligned}
\Delta^{(1,2)}\omega_p &= \omega_p^{(1)} - \omega_p^{(2)} \\
&= \left[\omega_{lo}^{(1)} - \omega_{lo}^{(2)}\right] + \left[-\left(\omega_c - \omega_{up}^{(1)}\right)\frac{\omega_p^{(1)}}{\omega_c} + \left(\omega_c - \omega_{up}^{(2)}\right)\frac{\omega_p^{(2)}}{\omega_c}\right] \\
&= \begin{cases} \left[\omega_{lo}^{(1)} - \omega_{lo}^{(2)}\right] = -\Delta_g & \text{case B1} \\ \left[\omega_{lo}^{(1)} - \omega_{lo}^{(2)}\right] + \left[\omega_{up}^{(1)} - \omega_{up}^{(2)}\right]\frac{\lambda_c}{\lambda_p} = -\Delta_e\left(1 - \frac{\lambda_c}{\lambda_p}\right) & \text{case B2} \\ \left[\omega_{up}^{(1)} - \omega_{up}^{(2)}\right]\frac{\lambda_c}{\lambda_p} = -\Delta_r\frac{\lambda_c}{\lambda_p} & \text{case B3} \end{cases}
\end{aligned} \tag{1.10}$$

As shown by Eq. 1.6 and Eq. 1.10, depending on which laser is scanning, the measured frequency differences between EIT resonances have to be scaled to match the atomic energy levels splittings. This is a direct consequence of the wavelength mismatch. During the Doppler averaging process, multiple velocity groups contribute to each EIT resonance observed, and the Doppler shifts pull the line center in opposite directions (see Fig. 1.2). The results shown in Tab. 1.1 still hold.

In addition, these relations can also be used to calibrate the laser scanning parameters if the atomic level splittings are known.

1.2.3 Probability Distribution of the Interaction Time

Due to the fast velocities of thermal atoms in room-temperature vapor cells, the interaction time of an atom with laser fields is short compared to the lifetime of the Rydberg states utilized in the Rydberg-EIT experiments. This is especially true in the cases where laser beams are tightly focused in order to achieve sufficiently high Rabi frequencies.

The limited interaction time causes additional spectroscopic line broadenings of measured signals. This affects the resolution of the field measurements. The magnitude of the interaction-time line-broadening can generally be estimated by the inverse of the averaged interaction time, which is the time atoms spend flying across the laser beams.

The estimation mentioned above is widely used in cold atomic beam experiments where the atoms usually have a well-defined velocity and direction. In a room-temperature vapor cell, this is not true. A slightly more detailed model is needed to capture effects given the random nature of the atomic motions.

For an interaction-time dependent observable, $O(t)$, in general, the experimentally measured value, $\overline{O}$, is an average over the probability density distribution of the time of

flight, $\mathcal{P}_{tof}(t)$, given by:

$$\overline{O} = \int O(t)\mathcal{P}_{tof}(t)\mathrm{d}t \tag{1.11}$$

The time of flight distribution density, $\mathcal{P}_{tof}(t)$, can be determined as a weighted average of the interaction time distribution density function $K(t;l)$ with a given trajectory length l:

$$\mathcal{P}_{tof}(t) = \int_0^{l_{max}} K(t;l)P_{trj}(l)\mathrm{d}l \tag{1.12}$$

The weighting factor $P_{trj}(l)\mathrm{d}l$ represents the probability of finding a trajectory with length l in an ensemble of atom trajectories.

The exact form of $\mathcal{P}_{tof}(t)$ depends on the degrees of freedom of the atomic motion and the geometry of the container. A hypothetical 2D model where analytic results can be easily obtained for $K(t;l)$ and $P_{trj}(l)$, while not most useful, provides physical insight. A real 3D situation will be discussed later.

The thermal atomic motion is described by the Maxwell-Boltzmann distribution, as shown in Eq. 1.13:

$$f_{3D}(v)\mathrm{d}v_x\mathrm{d}v_y\mathrm{d}v_z = \left(\frac{m}{2\pi k_B T}\right)^{3/2} \exp\left(-\frac{mv^2}{2k_B T}\right)\mathrm{d}v_x\mathrm{d}v_y\mathrm{d}v_z \tag{1.13}$$

where atom velocity amplitude $v = \sqrt{v_x^2 + v_y^2 + v_z^2}$. If we denote the transverse velocity as $v_\perp = \sqrt{v_x^2 + v_y^2}$ and integrate Eq. 1.13 over v_z and the azimuthal angle φ, we can find the velocity distribution of $v_\perp$ in 2D as:

$$f_{2D}(v_\perp)\mathrm{d}v_\perp = \frac{m}{k_B T} \exp\left(-\frac{mv_\perp^2}{2k_B T}\right) v_\perp \mathrm{d}v_\perp \tag{1.14}$$

In room-temperature vapor cells used in most Rydberg-EIT experiments, the vapor pressure and the atomic density are very low. The mean free path is usually much larger than the vapor cell dimension. Therefore, we assume the atoms merely experience collisions when they fly through the laser beams. (Note that this assumption barely holds in atomic vapor cells with significant buffer/quenching gas pressure.) Under such assumptions, for a given flight distance l, the following probability must be held equal:

$$f_{2D}(v_\perp)\mathrm{d}v_\perp = K_{2D}(t;l)\mathrm{d}t \tag{1.15}$$

Then $K_{2D}(t;l)$ follows as

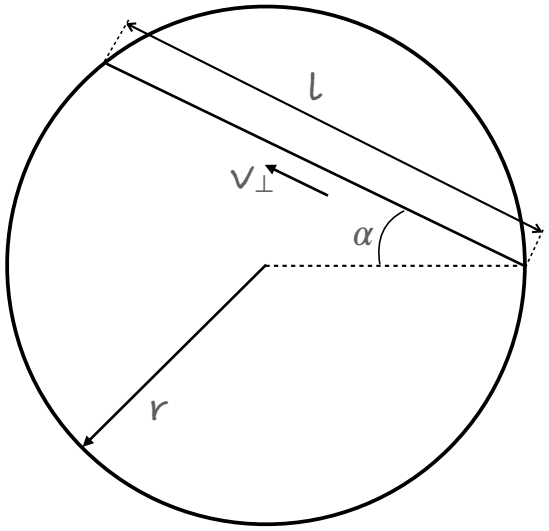

Figure 1.4: sketch for a flight path in a 2D cell.

$$K_{2D}(t;l) = \frac{m}{k_B T} \exp\left(-\frac{m}{2k_B T}\frac{l^2}{t^2}\right)\frac{l^2}{t^3} \tag{1.16}$$

where the following change of variables has been used:

$$v_\perp t = l \tag{1.17}$$

$$t|\mathrm{d}v_\perp| = v_\perp|\mathrm{d}t| \tag{1.18}$$

In order to fully specify the time-of-flight probability density distribution, $\mathcal{P}_{tof}$ in Eq. 1.12, we need to find the probability distribution $P_{trj}(l)$ for a given trajectory length l. Under the no-collision assumption, this quantity depends on the geometry of the physical cell. For the spirit of a 2D model, let us consider a fictional 2D cell with azimuthal symmetry as shown in Fig. 1.4. Under such construction, atoms fly into the cell from the circumsference specified by some geometrical parameters labeled in Fig. 1.4.

In a 2D system where Eq. 1.14 holds, the probability of finding a trajectory of length l, $P_{trj}(l)|\mathrm{d}l|$, after some thoughts, should be:

$$P_{trj}(l)|\mathrm{d}l| = \cos\alpha|\mathrm{d}\alpha| \tag{1.19}$$

where α is the angle to the normal on the wall as shown in Fig. 1.4. Note that the $\cos\alpha$ factor, rather than a uniform (i.e., α independent) factor, used in Eq. 1.19 is essential. This

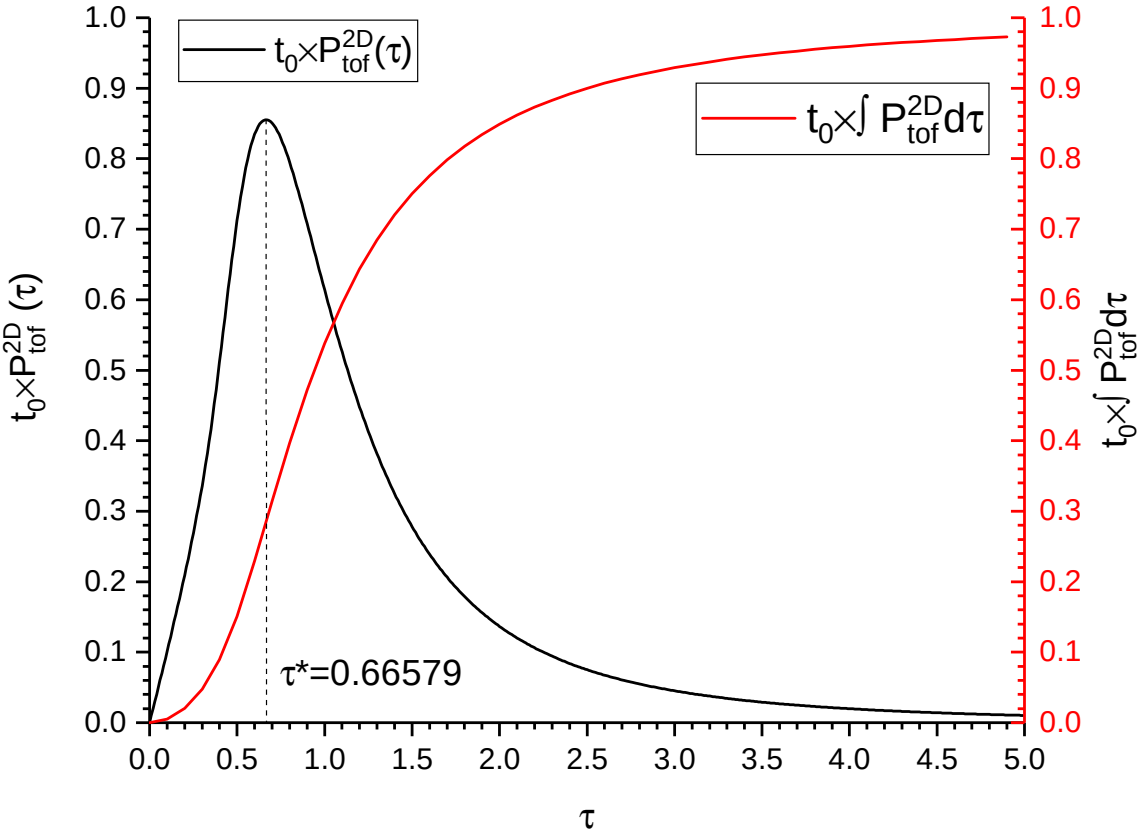

Figure 1.5: Numerical illustration of probability density Eq. 1.22 (black curve) and its integrated probability distribution (red curve). The absolute values are scaled by the characteristic time t_0.

factor ensures a Maxwell-like velocity distribution (shown by Eq. 1.14) inside the cell.

Using $l = 2r\cos\alpha$ and after some variable changes, we can find:

$$P_{trj}(l) = \frac{l}{2r\sqrt{4r^2 - l^2}} \tag{1.20}$$

where r is the radial of the cell.

Therefore, in a 2D model, the time-of-flight probability density distribution can be found as:

$$\mathcal{P}_{tof}^{2D}(t) = \int_0^{2r} \mathrm{d}l \frac{m}{k_B T} \exp\left(-\frac{m}{2k_B T}\frac{l^2}{t^2}\right)\frac{l^3}{t^3}\frac{1}{2r\sqrt{4r^2 - l^2}} \tag{1.21}$$

If we define $v_0 = \sqrt{2k_BT/m}$, $t_0 = 2r/v_0$ and $\tau = t/t_0$, we can write the integral in Eq. 1.21 in a dimensionless fashion. Not surprisingly, we find that $\mathcal{P}_{tof}^{2D}(t)$ scales like $\sim 1/t_0$ as:

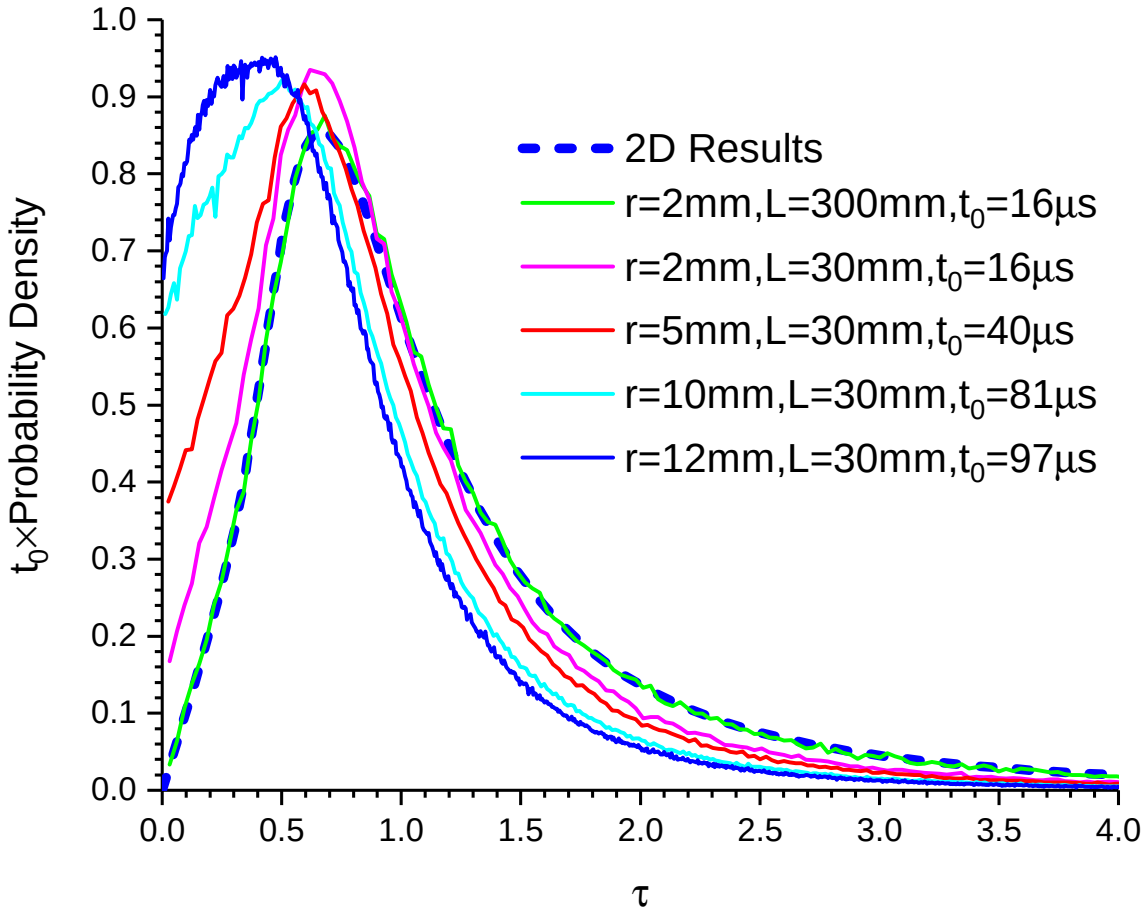

Figure 1.6: Scaled probability density distribution of the time of flight inside a cylindrical interaction region with different different geometrical parameters.

$$\mathcal{P}_{tof}^{2D}(\tau) = \frac{2}{t_0}\int_0^1 \mathrm{d}x \exp\left(-\frac{x^2}{\tau^2}\right)\left(\frac{x}{\tau}\right)^3 \frac{1}{\sqrt{1-x^2}} \tag{1.22}$$

Eq. 1.22 is plotted in Fig. 1.5. Numerical data show that the density distribution $\mathcal{P}_{tof}^{2D}(t)$ peaks at the most probable time of flight $t \simeq 0.67 t_0$.

The analytic result mentioned above for the 2D scenario does not take the longitudinal (along the laser propagation direction) motion of the atoms into account. This assumption works well when the geometry of the laser beam has a small diameter-to-length ratio.

For a realistic 3D model, motions between the two end windows of the vapor cell need to be considered. Theoretical/analytic analyses that incorporate longitudinal effects in a terminated cell are complex [37].

A numerical Monte Carlo investigation is relatively straightforward for a 3D cylindrical vapor cell in which the atoms can move freely in 3D. The cell volume is terminated by the two end windows. Most of the model trajectories start/end on the cylindrical side

walls of the cell, but the model also includes trajectories in which atoms start/end on the end window;, there are, of course, mixed cases. Typical results can be found in Fig. 1.6.

The simulation results for cases in which the diameter to length ratio is large indicate significant deviations from the 2D model (Eq. 1.21) in the region of small τ. We can see there are significant contributions near $\tau = 0$, and the peak for the most probable interaction time becomes less prominent in these cases. The green line in Fig. 1.6 shows that the 3D simulation approaches the 2D model result when the diameter-to-length ratio becomes small enough.

CHAPTER 2

Rydberg States of Rubidium Atoms

Powered by laser cooling and coherent spectroscopy technologies [38, 39], Rydberg atoms have demonstrated great potential in areas ranging from classical microwave and THz-wave field sensing and detection [40, 41, 42, 43, 12] to the production and readout mechanisms of non-classical states of light [44, 45, 46, 47]. They are widely considered to be a valuable building block [48, 49] for quantum-based technologies because of their strong coupling to external electromagnetic fields [50] and tunable interactions [51, 52]. The successful implementation of EIT in vapor cells has sparked new ideas for making quantum-enabled devices such as atomic-optical clocks [53], sensitive motion sensors [13], magnetometers [54, 55], microwave sensing devices [14], etc.

In this chapter, I summarize some important properties of the Rb Rydberg atoms, which are closely related to the Rydberg-EIT spectroscopy.

2.1 General Properties and n-Scaling Laws

Rydberg atoms have been one of the most studied subjects in the atomic research fields in the past a few decades. Their unique properties, such as the large orbital size of the valence electron, large transitional dipole moments, strong interactions with external electromagnetic fields, etc., make them an attractive platform for systems of quantum information, quantum communication and quantum metrology and sensing.

The name "Rydberg atom" is given to these extraordinary states of atoms in honor of the physicist Johannes Rydberg. He introduced the empirical formula to describe the energy intervals of the hydrogen. This Rydberg formula, together with the Rydberg constant, predicts that the energy levels of a bound electron are discrete and follow

$$E_n = -\frac{R_y}{n^2} \tag{2.1}$$

Table 2.1: Principal quantum number (n) scaling laws of the Alkali atom Rydberg states.

Property	Quantity	Scaling
Energy levels	E_n	n^{-2}
Level spacing	ΔE_n	n^{-3}
Radius	$\langle r \rangle$	n^2
Transition dipole moment ground to Rydberg states	$\lvert\langle n\ell \rvert er \rvert g\rangle\rvert$	$n^{-3/2}$
Decay lifetime	τ	n^3
Polarizability	α	n^7
Van der Waals interaction	C_6	n^{11}
Resonant dipole interaction	C_3	n^4

where n is a discrete integer, also known as the principal quantum number and R_y is the Rydberg unit of energy which is defined by the Rydberg Constant R_∞ through

$$\begin{aligned} 1Ry \equiv hcR_\infty &= \frac{m_e e^4}{8\epsilon_0^2 h^2} \\ &= \frac{1}{2} \quad \text{(a.u.)} \\ &\approx 2.18 \times 10^{-18} \quad \text{(J)} \\ &\approx 13.6 \quad \text{(eV)} \end{aligned} \tag{2.2}$$

where h is the Planck constant, c is the speed of light, m_e is the rest electron mass, e is elementary charge and ϵ_0 is the vacuum permittivity. Its numerical value is also shown in three common unit system (the a.u. stands for atomic units).

For a highly excited Rydberg state, the electron is far away from the nucleus and thus is weakly bounded. This configuration makes the electron very sensitive to external electric fields. In addition, the relatively long lifetime (on the order of hundreds of microseconds) of these highly excited states gives Rydberg atoms the promising potential to become atom sensors. Many other useful properties of the Rydberg atoms, such as polarizability and transition dipole moments, scale strongly with principal number n. These n-dependencies result from the characteristics of the Rydberg atom wavefunctions which are discussed in Ch. 3. Some of these properties are summarized in Tab. 2.1.

2.2 Radiative & Blackbody Decay Lifetime

One particular property that is most relevant to the topic of this thesis is the decay life time of the Rydberg states. The decay rate $1/\tau$ can be decomposed as:

Table 2.2: Lifetime parameters in Eq. 2.5 for Rb Rydberg states with different angular momentum quantum number l up to 3

test	s	p	d	f
τ_0 (ns)	1.43	2.76	2.09	0.76
α	2.94	3.02	2.85	2.95

$$\frac{1}{\tau} = \frac{1}{\tau_r} + \frac{1}{\tau_{bb}} \tag{2.3}$$

where τ_r and τ_{bb} are the inverse of the spontaneous decay rate and blackbody decay rate, respectively. The spontaneous decay of a Rydberg state usually involves many possible decay channels. The decay rate is, however, typically dominated by the channel that has the highest transition frequency due to its cubic dependency on the transition frequency:

$$\frac{1}{\tau_r} = \frac{3}{2}\frac{e^2\mu_{ij}\omega_{ij}^3}{\epsilon_0 c^3} \tag{2.4}$$

where, e is the electron charge, μ_{ij} denotes the dipole moment between two states i and j, and ω_{ij} represents the transition angular frequency in units of rads.

The total lifetime of the Rydberg state can be calculated accurately and has been compared with experiments extensively (see Theodosiou et.al. [56]). They can also be conveniently parameterized by using the following equation

$$\tau = \tau_0 (n^*)^\alpha \tag{2.5}$$

where n^* is the effective principal quantum number, which differs from the normal integer-numbered principal quantum number by real-number values called quantum defects (See Ch. 2.3 for details). For Rubidium Rydberg states, τ_0 and α are given in Table. 2.2

For high angular momentum Rydberg states, the lifetime is dominated by the blackbody radiation induced decay. The spontaneous emission rate decreases rapidly as l increases. For sufficiently high l states, the black body decay rate only depends on the principal quantum number n but not l and can be estimated by

$$\frac{1}{\tau_{bb}} = \frac{4\alpha^3 k_B T}{3n^2} \tag{2.6}$$

where α is the fine structure constant, k_B is the Boltzmann constant, and T is the temperature in Kelvin. Note that, for high l states, quantum defects are usually small, such that $n^* \approx n$. It is also important to notice that the blackbody decay rate scales as $1/n^2$

Table 2.3: Parameters in Eq. 2.7

$S_{1/2}$				$P_{1/2}$ / $P_{3/2}$				$D_{3/2}$ / $D_{5/2}$			
A	B	C	D	A	B	C	D	A	B	C	D
0.134	0.251	2.567	4.426	0.053	0.128	2.183	3.989	0.033	0.084	1.912	3.176
				0.046	0.109	2.085	3.901	0.032	0.082	1.898	3.703

as opposed to $1(/n^*)^3$. Therefore, even for low l states, as long as it has a high enough principal quantum number, the blackbody decay rates can contribute large amounts to the total lifetime which cannot be totally ignored. It also plays an important role in population redistribution among the Rydberg states manifold.

For low ℓ states, the blackbody decay life can also be parameterized for quick estimation using the following formula as shown in the work of I. I. Beterov et.al. [57]:

$$\frac{1}{\tau_{bb}} = \frac{A}{(n^*)^D} \frac{2.14 \times 10^{10}}{exp[315780 \times B/(n^*)^C \times T] - 1} \quad (\mathrm{s}^{-1}) \tag{2.7}$$

where parameters A, B, C and D are summarized in Table. 2.3 for the Rb atoms.

2.3 Energies of Rydberg States and Quantum Defects

Alkali atoms such as Rubidium have one valence electron orbiting an ion core. The energy level structure of this electron naturally resembles that of a hydrogen atom. However, due to the finite size of this ion core, the electron can both polarize and penetrate it. These two effects lead to very different energy structures than those of the hydrogen atom.

Due to the rapid increase of the centrifugal potential $\ell(\ell+1)/2r^2$ as a function of ℓ, the core polarization effect is small for the Rydberg electron with high angular momentum. Therefore, for the high-ℓ state, the major deviation from the Rydberg formula (see Eq. 2.2) comes from the polarization energy W_{pol}, which can be written in atomic units as:

$$W_{pol} = -\frac{\alpha_d}{2}\langle r^{-4}\rangle - \frac{\alpha_q}{2}\langle r^{-6}\rangle \tag{2.8}$$

where α_d and α_q are the dipole and quadrupole polarizabilities of the ionic core. For the high-ℓ state, both $\langle r^{-4}\rangle$ and $\langle r^{-6}\rangle$ exhibit n^{-3} scaling of the principal quantum number n. Therefore, we can write the energy $W_{n\ell}$ of the state $|n, \ell\rangle$ as:

$$W_{n\ell} = -\frac{Ry}{n^2} - \frac{\delta_\ell}{n^3} \tag{2.9}$$

where δ_ℓ is a ℓ dependent, real valued quantity called quantum defect.

Table 2.4: Fine structure parameters in Eq. 2.11

ℓ	A	B	C
p	85.865THz		
d	10.800(15) THz	-84.87(10) THz	
f	-152 GHz	1.82 THz	

When the spin-orbit interaction is included, Eq. 2.9 is then corrected by the fine structure splitting between the $j = \ell + 1/2$ state and the $j = \ell - 1/2$ state. For the hydrogen atom, the fine structure splitting W_{FS} is given by

$$W_{FS} = \frac{\alpha^2}{2n^3}\frac{1}{\ell(\ell+1)} \tag{2.10}$$

where α is the fine structure constant. For Alkali atoms, the fine structure splitting does not scale completely as n^{-3}. A better parameterized formula can be used

$$W_{FS} = \frac{A}{(n-\delta)^3} + \frac{B}{(n-\delta)^5} + \frac{C}{(n-\delta)^7} \tag{2.11}$$

where A, B and C are fitting parameters. The value for Rubidium are listed in Table. 2.4

For the low-ℓ state, the core penetration effect plays an important role. The energy of these states can be parameterized by the quantum defects as follows:

$$W_{n,\ell,j} = -\frac{R_y}{(n^*)^2} = -\frac{R_y}{(n-\delta_{n,\ell,j})^2} \tag{2.12}$$

where is n^* is the effective quantum principal number, and quantum defects $\delta_{n,\ell,j}$ are parameterized by the Rydberg-Ritz formula as:

$$\delta_{n,\ell,j} = \delta_0 + \frac{\delta_2}{(n-\delta_0)^2} + \frac{\delta_4}{(n-\delta_0)^4} + ... \tag{2.13}$$

In a power series expansion of Eq.2.12 with respect to $\delta_{n,\ell,j}/n$ (note that $\delta_{n,\ell,j} \ll n$ for Rydberg states), the first order term goes as follows $\delta_{n,\ell,j}/n^3$. This n^{-3} scaling is the same as the corrections produced by the core polarization effects and fine structure splitting. Therefore, the Rydberg-Ritz formula can be used to parameterize the Rydberg state energies regardless of the angular momentum quantum number. These quantum defects for Rb atoms can be found in Refs. [58, 59, 60].

The Rydberg-Ritz formula Eq. 2.13 is widely used as a fitting function for experimentally measured data. It is different from the analytic result obtained by the quantum defect theory [61]. Some limitations of the Rydberg-Ritz formula Eq. 2.13 are discussed in

Ref. [62].

2.4 Static Electric Fields and Stark Effects

As shown in Tab. 2.1, the extremely high polarizability makes Rydberg atoms sensitive to small external electric field perturbations. These perturbations manifest themselves through the energy Stark shifts of the Rydberg states. Accurate measurements of these shifts allow us to use Rydberg atoms as atomic sensors to detect minute electric fields.

2.4.1 Macroscopic Homogeneous Fields and Ensemble Average

Detailed Stark maps in which precise energy shifting behavior of the relevant Rydberg states are required in order to extract information about the actual field strength and direction from the experimental results. Rydberg states are hydrogen-like in many aspects. However, the successful perturbation treatment of the Stark effect in hydrogen atoms fails to provide accurate Stark maps for alkali-metal atoms with ion cores of a finite size. A complete matrix diagonalization using a few hundreds of unperturbed Rydberg basis states is desirable[63, 64].

With the help of modern computers, these computations can be processed in the blink of an eye. Details about the basis state preparation and related computational aspects are discussed in Chap. 3. Fig. 2.1 shows a Stark map example of the Rb 60D Rydberg state. Near zero electric fields, it demonstrates the familiar quadratic Stark effects predicted by the second-order perturbation theory. The dramatic down shifts above 0.5 V/cm are caused by nonzero matrix elements between the 60D states and the down-shifting high-angular-momentum states (not shown in the figure) above the 60D states.

Rydberg EIT spectroscopy turns out to be a versatile experimental tool to measure these Stark shifts hence the electric fields. Fig. 2.2 adapted from Ref. [65] demonstrates, in astonishing detail, the capability of this technique for mapping Stark shifts . In this demonstration, the electric fields are generated by electrodes inside a room temperature glass cell. The cell is connected to the vacuum system, in which the Rb vapor pressure is maintained at 1×10^{-7} mbar.

Stark shifts shown in Fig. 2.1 and Fig. 2.2, assume a spatially uniform external electric fields inside the measurement region. This is usually an over simplified situation for real world electric fields sensing applications. The Rydberg EIT measurement with hot atom vapor is averaged over an ensemble of atoms which may experience different fields strengths. This average can be performed on a macroscopic level using the single atom

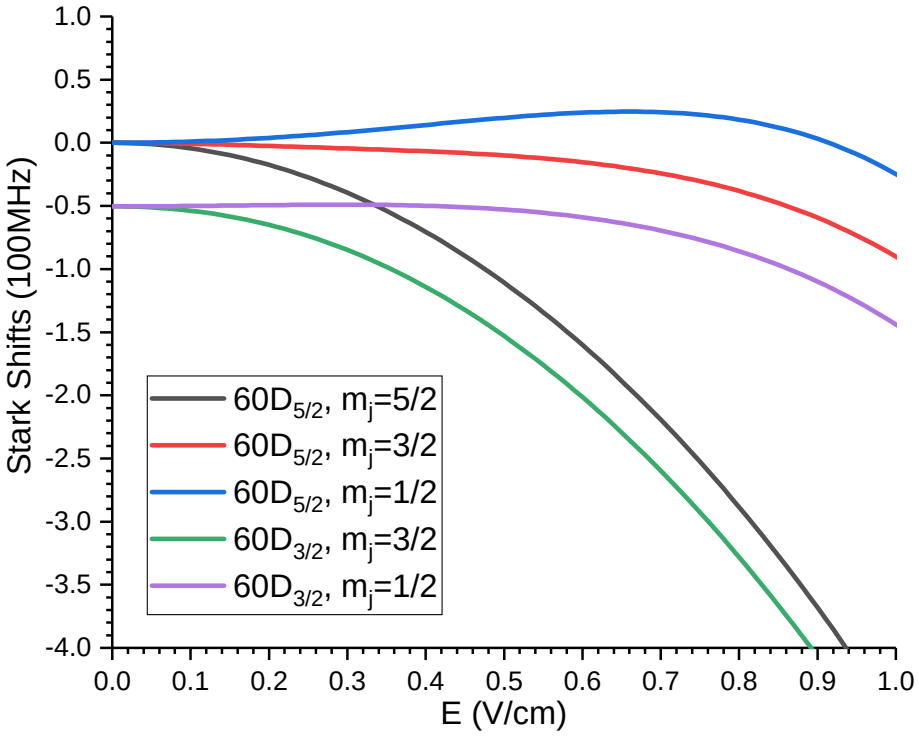

Figure 2.1: Detailed Stark shifts of the Rb 60D states in a uniform external electric fields. This shifts are demonstrated in units of wavenumber, and zero energy is referenced to the ionization threshold of the Rydberg electron.

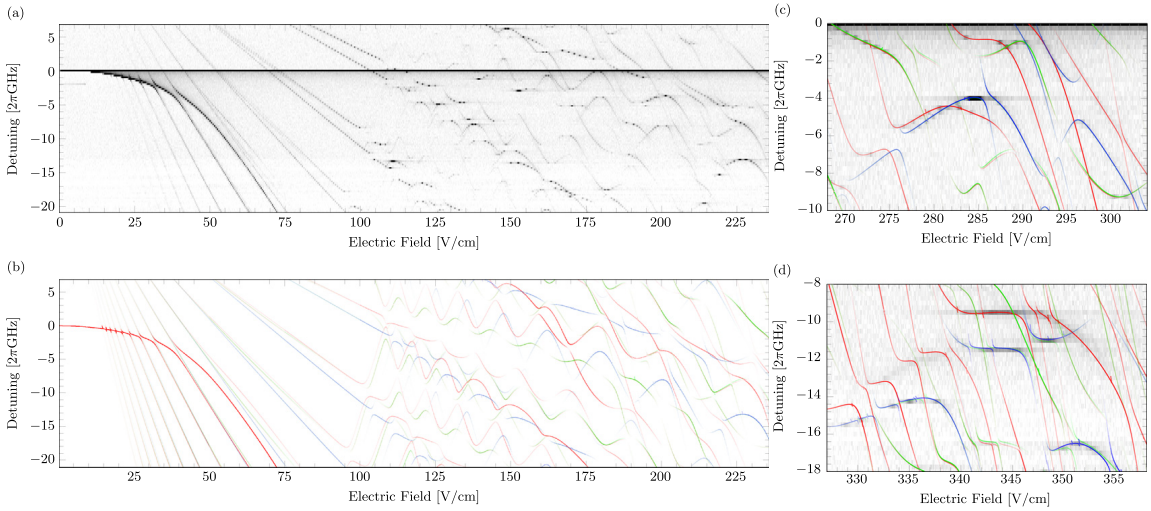

Figure 2.2: Rydberg Stark map measured by the EIT spectroscopy in a vapor cell adapted from Ref. [65].(a) Stark map for $35S_{1/2}$ for an electric field range of 0–235 V/cm. (b) The red, green and blue lines show the numerically calculated Stark map for $|m_j| = 1/2$, $|m_j| = 3/2$ and $|m_j| = 5/2$, respectively. The opacity gradients represent the transition strength. (c) and (d) show details of the measurement with the numerically calculated Stark map on top for $35S_{1/2}$.

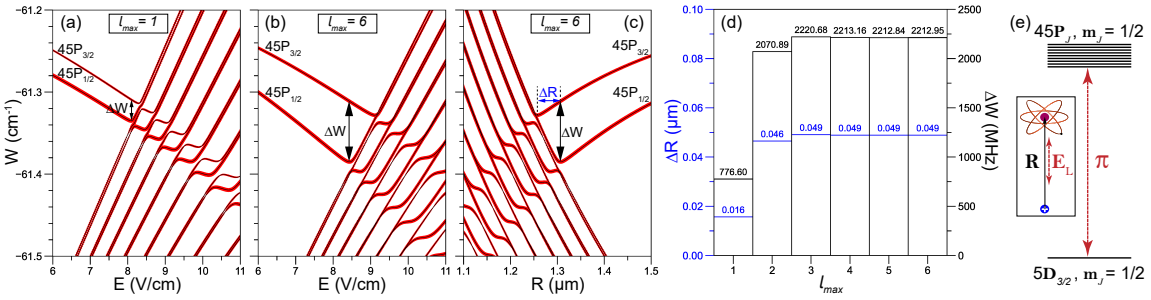

Figure 2.3: (Color online) Energy shifts of the Rb 45P states in a multipolar static electric field (a) Energy shifts a function of electric field $E = Q/(4\pi\epsilon_0 R^2)$ with $l_{max} = 1$ in Eq. 2.15.(b) Similar to (a), but with $l_{max} = 6$. (c) Similar as (b), but plotted as a function of R with Q set to one elementary charge. Thickness of lines are proportional to the square root of the oscillator strengths of different transitions. (d) Effect of l_{max} in Eq. 2.15 on the fine-structure splitting, ΔW, indicated in (c), and on the differential internuclear separation, ΔR, between the two most prominent minima in the relevant potential energy curves. (e)Possible single color excitation schemes where the neutral atom is initially prepared in $|5D_{3/2}, m_J = 3/2\rangle$ state and is excited to Rydberg state with π-polarized light. The angle θ between excitation laser electric field, $\mathbf{E}_L$, and the quantization axis is 0 as depicted in the inset.

Stark shifts. The ensemble average is discussed in greater detail in Sec. 3.2.

2.4.2 Microscopic Inhomogeneous Fields and Multipolar Interaction

The macroscopic average approach fails when the inhomogeneity of the electric fields is significant at a microscopic level (at a scale comparable to the size of the Rydberg atom). In contrast to the case of uniform electric fields, a quantized multipolar field interaction Hamiltonian is necessary. Although this situation is hard to encounter in vapor cell experiments, I give a brief summary of this microscopic field effects here for the completeness of the discussion.

We start with a classical picture in which the source charges of the multipolar electric field are separated from the Rydberg atom by a distance $|\boldsymbol{R}|$ that is larger, but comparable to orbital radius $|\boldsymbol{r}|$, i.e. $|\boldsymbol{R}| \gtrsim |\boldsymbol{r}|$.

Using the spherical expansion shown in Eq. 2.14 we can write down the interaction Hamiltonian V_{int} by promoting the classical Rydberg electron coordinate $\boldsymbol{r}$ to an operator as shown in Eq. 2.15

$$\frac{1}{|\boldsymbol{r}-\boldsymbol{R}|} = \sum_{l=1} \sqrt{\frac{4\pi}{2l+1}} \frac{|\boldsymbol{r}|^l}{|\boldsymbol{R}|^{l+1}} Y_l^0(\boldsymbol{r}) \quad (|\boldsymbol{r}| < |\boldsymbol{R}|) \tag{2.14}$$

$$V_{int}(\hat{\mathbf{r}}_e; R) = -\frac{Qe}{4\pi\epsilon_0}\sum_{l=1}^{l_{max}}\sqrt{\frac{4\pi}{2l+1}}\frac{\hat{r}_e^l}{R^{l+1}}Y_l^0(\hat{\theta}_e, \hat{\phi}_e) \tag{2.15}$$

In Eq. 2.15, we cut off the multipolar interaction order to l_{max}. Total source charge Q and distance R set the overall electric field strength. A direct matrix diagonalization using the interaction Eq. 2.15 is necessary in order to get the detailed Stark shifts. As an example, the Stark effect of this multipolar electric field on the Rb 45P state is plotted in Fig. 2.3. The effects of the max interaction order l_{max} are also illustrated. Note that, for $l_{max} = 1$, the energy shifts caused by the total electric field strength $|\boldsymbol{E}| = |Q|/4\pi\epsilon_0 R$ are the same as those in a uniform electric field of the same strength.

For strong electric fields or shorter distances, keeping higher orders of l is necessary because the energy scale of the matrix elements resulting from $\hat{V}_{int}$ can be on the same order as the fine structure splitting between near-by Rydberg states (for example between the $nP_{1/2}$ and the $nP_{3/2}$ states).

2.5 Static Magnetic Fields and Diamagnetism

The study of the magnetic fields effects on the Rydberg atoms dates back to the1930s in the experiments done by Jenkins and Segre [66]. In their experiment, the large diamagnetism of the Rydberg atoms was investigated. To get an intuitive picture of the large diamagnetism of Rydberg atoms, writing down the Hamiltonian in cylindrical coordinates (ρ, z) may actually be helpful in this case. For the magnetic field (in units of $\hbar/ea_0^2 \approx 2.35 \times 10^5$ T) orienting in the positive z direction, the Hamiltonian for the Rydberg electron reads

$$H = A(r)\boldsymbol{L}\cdot\boldsymbol{S} + \frac{1}{2}\boldsymbol{L}\cdot\boldsymbol{B} + \boldsymbol{S}\cdot\boldsymbol{B} + \frac{1}{8}\rho^2 B^2 \tag{2.16}$$

where $r = \sqrt{\rho^2 + z^2}$ is the electron-nucleus distance and A is the fine structure coupling function. The first term in Eq. 2.16 describes the spin-orbital interaction. The second and third terms give rise to the Zeeman effect. The last term which is proportional to the square of the magnetic field leads to the diamagnetism of Rydberg atoms.

Special attentions needs to be paid to the ratio between the quadratic and linear terms of the magnetic fields. Since Rydberg atoms have a large size and $\langle\rho^2\rangle \propto 1.5n^2$, where n is the principal quantum number, this ratio can be much larger than 1, even for a relatively small B field when the atoms are excited to a high Rydberg state. For B=1 T, $0.5n^2B = 1$ at $n = 32$. The competition between the linear term and the quadratic term manifest

itself more clearly for the spin down Rydberg state. In a sufficiently strong magnetic field, the energy down-shift due to the linear Zeeman effect will be over turned by the strong quadratic up-shift caused by the diamagnetism.

Just like the electric field case, by accurately measuring the Zeeman shifts of the Rydberg electron energy, we can use Rydberg atoms as a magnetic field sensors. The strong diamagnetism provides us with one additional advantage such that sensors made out of Rydberg atoms are sensitive to small perturbations on a large background field. Sensors with high sensitivity to minute fields (such as vapor cell magnetometers) usually have limited dynamic ranges and vice versa. Applications such as quench detection of super conducting magnets require a wide detection range together with high sensitivity for small perturbations. The large diamagnetism of the Rydberg atoms holds promising potential to bridge the gap.

It is also interesting to note that the quadratic energy shifts can be strong enough such that when it starts to approach the energy splittings between adjacent principal quantum levels ($\Delta E_n \simeq 1/n^3$), principal quantum number n will no longer be a good quantum number. For an S state with angular momentum quantum number $\ell = 0$, $\langle\rho^2\rangle$ scales as $\propto 2n^4$. Thus the magnetic field (in atomic units) only needs to reach $2n^{-3.5}$ for a principal quantum number n-mixing.

For further stronger $B \gg \sqrt{2}n^{-3}$ (in atomic units), the diamagnetic energy starts to become stronger than than Coulomb energy, i.e. $\langle\rho^2\rangle B^2/8 \gg \langle 1/r\rangle = 1/2n^2$, and the spherical symmetry of the Coulomb interaction starts to break down due the strong cylindrical symmetry imposed by the magnetic fields. Classical electron motions start to become sensitive to the initial conditions and demonstrate long term chaotic behaviors. The quantum behavior of the bounded wavefunctions, on the one hand, still demonstrates discrete energy levels [67]. On the other hand, the phase space is dominated by irregular trajectories [68]. This is the so called quantum chaos regime. There is no experimental proof that the nonlinear EIT spectroscopy is still going to work in such a strong fields. Nevertheless, in Ch. 4, I show how Rydberg EIT spectroscopy can be used to detect the diamagnetism of the Rydberg atoms.

CHAPTER 3

Numerical Calculations and Simulations

Due to years of extensive experimental and metrological efforts on measurements of Rydberg atoms' properties, Rydberg atoms are almost computable quantum systems in addition to hydrogen and helium atoms. These Rydberg physics data of high precision and accuracy enable us to make not only quantitative calculations about the quantum properties of Rydberg atoms but also establish realistic semi-classical simulations for various sensing applications in which the quantum properties of Rydberg atoms play key roles. The ability to numerically calculate Rydberg electron wavefunctions is the bedrocks for using them as atomic sensors.

In this chapter, I summarize and document the general procedures for evaluating Rydberg wavefunctions in the space domain and along with some computational techniques that are necessary to ensure efficiency and accuracy. In the context of the optical spectroscopy of gaseous samples, I outline the usage of density matrices and master equations with their applications in semi-classical simulations for experimentally measured signals.

3.1 Rydberg Wavefunction Calculations in the Space Domain

3.1.1 Backgrounds and General Procedures

Many quantum mechanical predictions related to Rydberg atoms require accurate calculations of the matrix elements for evaluating the interaction operators between the relevant Rydberg states. In many applications, the Rydberg electron is represented in the spatial coordinate basis where a radial part and an angular part of the wavefunction can be separated. The spin degree of freedom of the Rydberg electron can also be integrated with the angular part of the wavefunction using *generalized spherical harmonics*. These are two-component spinors composing regular spherical harmonics and Clebsch-Gordan coefficients.

The general procedures for calculating Rydberg wavefunctions in the spatial coordinates basis resemble the analytic evaluations of the hydrogen atom. However, due to the multi-body nature of the ionic core, analytic expressions for Rydberg wavefunctions are barely obtainable. (Whittaker functions and Coulomb functions [68] given by the non-relativist quantum defect theory [69, 70] are good analytic approximations [71].) Thanks to many precision measurements, the Coulomb potential generated by the ionic core can be numerically parameterized and modeled very accurately. Using these numerically modeled core potentials and experimentally measured energies of the Rydberg states, we can calculate the Rydberg electron wavefunctions with excellent precision. These wavefunctions are implemented as basis functions for evaluating quantum mechanical interactions involving Rydberg atoms.

The Hamiltonian for the Rydberg electron can be written, in atomic units, as

$$\hat{H}_{Ryd} = \frac{\hat{\boldsymbol{p}}^2}{2\mu} + \varphi_*(\hat{r}) + \alpha_*(r)\hat{\boldsymbol{\ell}} \cdot \hat{\boldsymbol{s}} \tag{3.1}$$

where μ is the reduced mass of the electron, $\hat{p}$ is the momentum operator, $\varphi_*(r)$ represent the ionic core potentials and $\alpha_*(r)$ is the spin orbit coupling strength. The subscript $*$ indicates that these quantities are numerically modeled and the parameters are Rydberg state dependent.

We use the traditional Pauli matrices to represent the spin operator $\hat{\boldsymbol{s}}$ as:

$$\hat{\boldsymbol{s}} = \frac{1}{2}\sigma_x \boldsymbol{e}_x + \frac{1}{2}\sigma_y \boldsymbol{e}_y + \frac{1}{2}\sigma_z \boldsymbol{e}_z \tag{3.2}$$

where $\boldsymbol{e}_x$, $\boldsymbol{e}_y$ and $\boldsymbol{e}_z$ are the unit vectors in the Cartesian coordinate system, and σ_x, σ_y, and σ_z are the Pauli matrices. The Pauli matrices are defined as:

$$\sigma_x = \begin{pmatrix} 0 & 1 \\ 1 & 0 \end{pmatrix} \quad \sigma_y = \begin{pmatrix} 0 & -i \\ i & 0 \end{pmatrix} \quad \sigma_z = \begin{pmatrix} 1 & 0 \\ 0 & -1 \end{pmatrix} \tag{3.3}$$

We can then represent the Rydberg state $|E_*, \ell, j, m_j\rangle$ in the spherical coordinate as:

$$\psi(\boldsymbol{r}) = \frac{\rho_*(r)}{r}\mathcal{Y}_{j,m_j,\ell}(\theta, \phi) \tag{3.4}$$

where $\mathcal{Y}_{j,m_j,\ell}$ are the generalized spherical harmonics (two-component vectors). These harmonics are defined as:

$$\mathcal{Y}_{j,m_j,\ell}(\theta,\phi) = \begin{array}{l} \dfrac{1}{\sqrt{2j}} \begin{pmatrix} \sqrt{j+m_j}\, Y_\ell^{m_j-1/2}(\theta,\phi) \\ \sqrt{j-m_j}\, Y_\ell^{m_j+1/2}(\theta,\phi) \end{pmatrix} \quad \text{for } \; j = \ell + \dfrac{1}{2} \\ \dfrac{1}{\sqrt{2j+2}} \begin{pmatrix} -\sqrt{j-m_j+1}\;\; Y_\ell^{m_j-1/2}(\theta,\phi) \\ \sqrt{j+m_j+1}\;\; Y_\ell^{m_j+1/2}(\theta,\phi) \end{pmatrix} \quad \text{for } \; j = \ell - \dfrac{1}{2} \end{array} \tag{3.5}$$

where $Y_\ell^m(\theta,\phi)$ are the regular spherical harmonics following the Condon-Shortley phase convention. Note that due to the spherical symmetry of the modeled ionic potential $\varphi_*(r)$ and $\alpha_*(r)$, Eq. 3.4 are completely separable between the radial and angular coordinates.

It is straight forward to show that the generalized spherical harmonics $\mathcal{Y}_{j,m_j,\ell}$ defined in Eq. 3.5 are common eigenstates of the operator sets $\left\{\hat{\boldsymbol{\ell}}^2, \hat{\boldsymbol{s}}^2, \hat{\boldsymbol{j}}^2\right\}$ with eigenvalues of $\ell(\ell+1)$, $s(s+1)$ and $j(j+1)$ respectively. It can also be shown that $\mathcal{Y}_{j,m_j,\ell}$ are normalized orthogonal sets satisfying

$$\int \mathrm{d}\Omega \;\; \mathcal{Y}^\dagger_{j',m'_j,\ell'} \cdot \mathcal{Y}_{j,m_j,\ell} = \delta_{j'j}\delta_{m'_j m_j}\delta_{\ell'\ell} \tag{3.6}$$

where δ_{ij} are the Kronecker delta functions and $\mathrm{d}\Omega$ is the differential solid angle.

In Eq. 3.1, by writing

$$\hat{\boldsymbol{p}}^2 = -\left(\frac{\partial^2}{\partial r^2} + \frac{2}{r}\frac{\partial}{\partial r} - \frac{\hat{\boldsymbol{\ell}}^2}{r^2}\right) \tag{3.7}$$

and

$$\hat{\boldsymbol{\ell}} \cdot \hat{\boldsymbol{s}} = \frac{1}{2}\left(\hat{\boldsymbol{j}}^2 - \hat{\boldsymbol{\ell}}^2 - \hat{\boldsymbol{s}}^2\right) \tag{3.8}$$

together with Eq. 3.4, we can find that the radial part of the wavefunction, $\rho_*(r)$, satisfies the following radial Schrödinger equation:

$$\left(-\frac{1}{2\mu}\frac{\partial^2}{\partial r^2} + V_{eff}(r)\right)\rho_*(r) = E_*\rho_*(r) \tag{3.9}$$

where E_* is the energy of the Rydberg state, μ is the reduced mass and the effective potential, $V_{eff}(r)$, is defined as

$$V_{eff}(r) = \frac{\ell(\ell+1)}{2\mu r^2} + \varphi_*(r) + \frac{X_*}{2}\alpha_*(r) \tag{3.10}$$

where $X_* = j(j+1) - \ell(\ell+1) - s(s+1)$ is a state-dependent constant, $\alpha_*(r)$ is the state-dependent spin-orbit coupling function and $\varphi_*(r)$ is the ionic core potentials.

According to Eq. 3.9, the reduced radial wavefunction, $\rho_*(r)$, hence the total radial

wavefunciton, $\rho_*(r)/r$, is numerically computable once the E_*, $\alpha_*(r)$ and $\varphi_*(r)$ are numerically specified. They can be accurately modeled with experimental measurements inputs for a particular Rydberg state $|*\rangle$ with angular quantum number ℓ, j, m_j. Details are presented in Sec. 3.1.2.

Before diving into these modeled potentials, let us summarize the numerical integration method that is suitable for solving Eq. 3.9. The reduced radial wavefunction, $\rho_*(r)$ of a Rydberg electron is highly oscillatory due to the high Rydberg energy. In the classically allowed region where $E_* > V_{eff}$, the oscillatory nature of $\rho_*(r)$ can be described by a local de Broglie wave length, $\lambda_{\rm local}(r)$, defined as

$$\lambda_{\rm local}(r) = \frac{2\pi}{\sqrt{2\left[E_* - V_{eff}(r)\right]}} \tag{3.11}$$

For an accurate numerical evaluation of $\rho_*(r)$ over a discretized spatial region, Eq. 3.11 sets the upper limit on the step size needed for numerical discretization of Eq. 3.9. With proper scaling in amplitudes, i.e., $\mathrm{X}(r) = \rho_*(r) r^{-1/4}$, and change of variable, i.e. $x = \sqrt{r}$, Eq. 3.9 can be integrated in a fixed step size. One of the widely adopted, machine-precision numerical methods to discretize Eq. 3.9 is the Numerov method [72, 73]:

$$[1 - \mathrm{U}(x+h)]\,\mathrm{X}(x+h) + [1 - \mathrm{U}(x-h)]\,\mathrm{X}(x-h) = [2 + 10\mathrm{U}(x)]\,\mathrm{X}(r) + O(h^6) \tag{3.12}$$

where the propagation function $\mathrm{U}(x) = h^2 f(x)/12$, h is the step size and function $f(x)$ is defined as follows:

$$f(x) = 8\mu x^2 \left[\varphi_*(x^2) + \frac{X_*}{2}\alpha_*(x^2) - E_*\right] + \frac{(4\ell+1)(4\ell+3)}{4x^2} \tag{3.13}$$

In addition to the fixed-step Numerov method, the step-adjusted method based on the local de Broglie wavelength Eq. 3.11 can also be devised. A detailed derivation is found in Appendix A

3.1.2 Experimental Inputs: Ionic Core Potentials, Spin-orbit Couplings and Measured Quantum Defects

To accurately calculate the reduced radial wavefunction $\rho_*(r)$, we need to specify the ionic core potential $\varphi_*(r)$, the spin-orbit coupling function $\alpha_*(r)$ and the Rydberg state energy E_*.

The ionic core potentials have been modeled accurately by Marinescu et. al. in the

early 90s [74]. For the alkali atoms, it is given by the form

$$\varphi_*(r) = -\frac{Z_\ell(r)}{r} - \frac{\alpha_c}{2r^4}\left[1 - e^{(r/r_c)^6}\right] \tag{3.14}$$

where α_c is the core polarizability, r_c is the inner cutoff parameter introduced to avoid the potential divergence at the origin and the radial charge $Z_\ell(r)$ is given by

$$Z_\ell(r) = 1 + (z-1)e^{-a_1 r} - r(a_3 + a_4 r)e^{-a_2 r} \tag{3.15}$$

The state dependency of φ_* comes from the ℓ dependent parameters a_1 through a_4. The specific values of all the parameters in Eq. 3.14 and 3.15 can be found in the Table. 1 in Ref. [74]. The model potentials that include the spin-orbital interactions for high-ℓ Rydberg states can be found in Ref. [75].

The spin-orbit coupling strength function $\alpha_*(r)$ originates from the non-relativistic limit of the relativistic Dirac equation and takes the form of

$$\alpha_*(r) \sim \frac{1}{r}\frac{\mathrm{d}V}{\mathrm{d}r} \sim \frac{1}{r^3} \tag{3.16}$$

where V is the potential energy of the electron with the leading term of the Coulomb potential. For the Rydberg electron in an alkali atom, the exact form $\alpha_*(r)$ is complicated due to the nature of the multi-body system of the ionic core. However, it is, in general, a fairly localized function centered at the ionic core and diminishes quickly compared to the other terms in Eq. 3.10.

Due to the short-range nature of the $\alpha_*(r)$ and the fact that the amplitude of the reduced radial wave function $\rho_*(r)$ weighs heavily far from the ionic core, it is often a good approximation to set $\alpha_*(r)$ to zero when we numerically integrate Eq. 3.9.

It should be to be noted that, although the spin-orbit interaction is neglected when we numerically integrate Eq. 3.9 to find $\rho_*(r)$, the energy E_* in Eq. 3.9 should include the fine structure shifts and splittings and experimentally measured values with high accuracy are used. The amplitude of the reduced radial wave-function $\rho_*(r)$ depends sensitively on the value of E_* at the vicinity of the outer classical return point r_o where $V_{eff}(r_o) = E_*$.

For the low-ℓ state, the energies E_* have been experimentally measured and parameterized by the Rydberg-Ritz formula (Eq. 2.13) through precisely measured quantum defects data. For high-ℓ Rydberg states, precise experimental data on the fine structure splitting and shifts are not completely available. Results from the hydrogen atoms are used in such cases. Eq. 3.17 summarizes the fine structure splittings, $\Delta E_{n,\ell,*}$, between the two spin up and spin down pairs for different angular momentum ℓ:

$$\Delta E_{n,\ell,*} = \begin{cases} -\frac{1}{(n-\delta_{n,\ell,j_+})^2} + \frac{1}{(n-\delta_{n,\ell,j_-})^2} & \text{for } \ell = 1,2 \\ \frac{A^{(\ell)}}{(n-\delta_{n,\ell})^3} + \frac{B^{(\ell)}}{(n-\delta_{n,\ell})^5} & \text{for } \ell = 3 \\ \frac{\alpha^2}{2n^3}\frac{1}{\ell(\ell+1)} & \text{for } \ell \geqslant 4 \end{cases} \tag{3.17}$$

where information from Eq. 2.10 to Eq. 2.13 has been used.

Precise j-dependent quantum defects data are only available for low-ℓ states. To fix the energy of the high-ℓ states, we need to approximate the spin-orbit coupling matrix $\langle \alpha_* \hat{\boldsymbol{\ell}} \cdot \hat{\boldsymbol{s}} \rangle$ without detailed knowledge of $\alpha_*(r)$.

Let us denote $|W_{n,\ell}, *\rangle$ as the Rydberg wavefunction of energy $W_{n,\ell}$ without the fine structure where $*$ represents other quantum numbers. The matrix element of the spin-orbit coupling operator can be evaluated as

$$\langle W_{n,\ell}, *| \, \alpha_* \hat{\boldsymbol{\ell}} \cdot \hat{\boldsymbol{s}} \, |W_{n',\ell'}, *'\rangle = \delta_{\ell,\ell'} \delta j, j' \delta_{m_j, m_j'} \cdot \begin{cases} \frac{1}{2}\ell \alpha_{nn'}^{(\ell)} & \text{for } j = \ell + \frac{1}{2} \\ -\frac{1}{2}(\ell+1)\alpha_{nn'}^{(\ell)} & \text{for } j = \ell - \frac{1}{2} \end{cases} \tag{3.18}$$

where $\alpha_{n,n'}^{(\ell)}$ is the radial part integral. It is defined as:

$$\alpha_{n,n'}^{(\ell)} = \int_0^\infty r^2 \mathrm{d}r \frac{\phi_{n',\ell'}(r)}{r} \alpha_*(r) \frac{\phi_{n,\ell}(r)}{r} \tag{3.19}$$

where $\phi_{n,l}(r)$ satisfies the radial Schrödinger equation without the spin-orbit coupling

$$\left[-\frac{1}{2\mu}\frac{\partial^2}{\partial r^2} + \frac{\ell(\ell+1)}{2\mu r^2} + \varphi_\ell(r) \right] \phi_{n,\ell}(r) = W_{n,\ell} \, \phi_{n,\ell}(r) \tag{3.20}$$

According to Eq. 3.17, the exact energy difference $\Delta E_{n,\ell,*}$ of the two fine structure levels, $|n, \ell, j_+, m_{j+}\rangle$ and $|n, \ell, j_-, m_{j-}\rangle$ can be measured precisely in experiments. The radial part of the diagonal $\alpha_{n,n}^{(\ell)}$ matrix elements is therefore

$$\alpha_{n,n}^{(\ell)} = \frac{\Delta E_{n,\ell,*}}{(2\ell+1)/2} = \frac{E_{n,\ell,j_+,m_{j+}} - E_{n,\ell,j_-,m_{j-}}}{(2\ell+1)/2} \tag{3.21}$$

Since the fine-structure interaction depends on the behavior of the wavefunctions near the ionic origin, for a given ℓ value, this varies only with the normalization factor of the wave-function. Therefore, the radial part of the off-diagonal matrix elements $\alpha_{n,n'}^{(\ell)}$ can be estimated by using the diagonal part $\alpha_{n,n}^{(\ell)}$[76] as

$$\alpha_{n,n'}^{(\ell)} = \sqrt{\alpha_{n,n}^{(\ell)} \cdot \alpha_{n',n'}^{(\ell)}} \times \mathrm{sgn}\left[\alpha_{n,n}^{(\ell)} \cdot \alpha_{n',n'}^{(\ell)} \right] \tag{3.22}$$

3.1.3 Angular Momentum Algebra and Its Numerical Evaluations

In the last section, we outlined the general procedures to numerically evaluate the reduced radial wavefunctions $\rho_*(r)$. Together with the generalized spherical harmonics $\mathcal{Y}_{\ell,j,m_j}$, they serve as the basis functions for calculating the matrix representations of the quantum operators acting on the Rydberg state manifolds.

In many cases, these quantum interaction operators can also be separated into a radial part and an angular part. Hence, the matrix elements of such operators include an integral in the radial coordinates and an integral in the angular domain. Once we calculate the numerical function of the radial wavefunctions of the relevant Rydberg states, it is quite straightforward to perform the radial integral numerically.

For the evaluation of the angular part of the matrix elements, angular momentum algebra can be applied first. These algebraic transformations usually alleviate the burden of directly integrating the spherical harmonics over the whole solid angle space; in return, however, we need to evaluate some algebraic quantities such as Wigner-3j symbols(or Clebsch-Gordan Coefficients), Wigner-6j symbols etc.

For example, evaluating the matrix elements in Eq. 2.15 involves an integral of the three spherical harmonic functions. By using the identity:

$$\int \mathrm{d}\Omega (Y_{\ell_3}^{m_3})^* Y_{\ell_1}^{m_1} Y_{\ell_2}^{m_2} = \sqrt{\frac{(2\ell_1+1)(2\ell_2+1)}{4\pi(2\ell_3+1)}} \langle \ell_1, m_1, \ell_2, m_2 | \ell_3, m_3 \rangle \langle \ell_1, 0, \ell_2, 0 | \ell_3, 0 \rangle \tag{3.23}$$

we can relate the angular integral to the Clebsch-Gordan coefficients $\langle \ell_1, m_1, \ell_2, m_2 | \ell_3, m_3 \rangle$ which in turn can also be related to the Wigner-3j symbols as

$$\langle \ell_1, m_1, \ell_2, m_2 | \ell_3, m_3 \rangle = (-1)^{\ell_1 - \ell_2 + m_3} \sqrt{2\ell_3 + 1} \begin{pmatrix} \ell_1 & \ell_2 & \ell_3 \\ m_1 & m_2 & -m_3 \end{pmatrix} \tag{3.24}$$

Exact values of the C-G coefficients and Wigner-symbols are well documented for small angular momentum quantum values. An analytic expression given by G. Racah[77] allows us to obtain the exact numerical values of the C-G coefficients by evaluating:

$$
\begin{aligned}
&\langle j_1, m_1, j_2, m_2 | j_3, m_3 \rangle \\
&= \delta_{m_3, m_1+m_2} \left[(2j_3+1) \tfrac{(j_1+j_2-j_3)!(j_2+j_3-j_1)!(j_3+j_1-j_2)!}{(j_1+j_2+j_3+1)!} \right. \\
&\qquad \left. \times \textstyle\prod_{i=1,2,3} (j_i+m_i)!(j_i-m_i)! \right]^{1/2} \\
&\times \textstyle\sum_\nu \big[\, (-1)^\nu \nu! (j_1+j_2-j_3-\nu)! (j_1-m_1-\nu)! \\
&\qquad \times (j_2+m_2-\nu)! (j_3-j_1-m_2+\nu)! (j_3-j_2+m_1+\nu)! \, \big]^{-1}
\end{aligned}
\tag{3.25}
$$

where ν is summed over all integers in condition that all the variables of the factorial function take non-negative integer values.

The Racah formula Eq. 3.25 is useful for studying the symmetry properties of the C-G coefficients and also allows us to evaluate them exactly. However, for the high angular momentum states, due to the rapid growth (and eventual overflow of the computer memory) of the factorial functions in Eq. 3.25, it is not suitable for a fast, machine-number precision evaluation. Other exact evaluations for an arbitrary order of the angular momentum exist (See, for example, the documentation of computing software *Mathematica*). However these algorithms are computationally costly.

For calculations at the machine-number precision level, low-cost, fast algorithms for evaluation of Wigner-3j or even higher order symbols are desired. Utilizing the recursive relations among the Wigner-3j and Wigner-6j symbols, Klaus Schulten and Roy G. Gordon, in the 1970s, pioneered the work of developing the machine precision algorithms for fast evaluations of these coefficients [78]. The recurrence relations of 3j or 6j symbols take a form such as:

$$
\begin{gathered}
X_\psi(n)\psi(n+1) + Y_\psi(n)\psi(n) + Z_\psi(n)\psi(n-1) = 0 \\
n_{min} \leqslant n \leqslant n_{max}
\end{gathered}
\tag{3.26}
$$

where ψ represents the 3j or 6j symbol, the variable n can be a j quantum number or a m quantum number within the range of n_{min} to n_{max}, which is governed by the angular momentum coupling algebra. X_ψ, Y_ψ, and Z_ψ are variable dependent coefficients. The exact forms of these coefficients are documented in Table.1 of Ref. [79].

One limitation of the $ab\ initio$ algorithm that Schulten and Gordon proposed is that overflow/underflow glitches may occur. These lead to step rejection and re-initiation during the implementation of their method. The re-initiation limits the efficiency of such a method. In the late 1990s, J. H. Luscombe and M. Luban modified the widely adopted Schulten-Gordon algorithms[78]. The modified method eliminates the programming overhead for over/underflow checking and rescaling tracking, yet it provides highly accurate results with

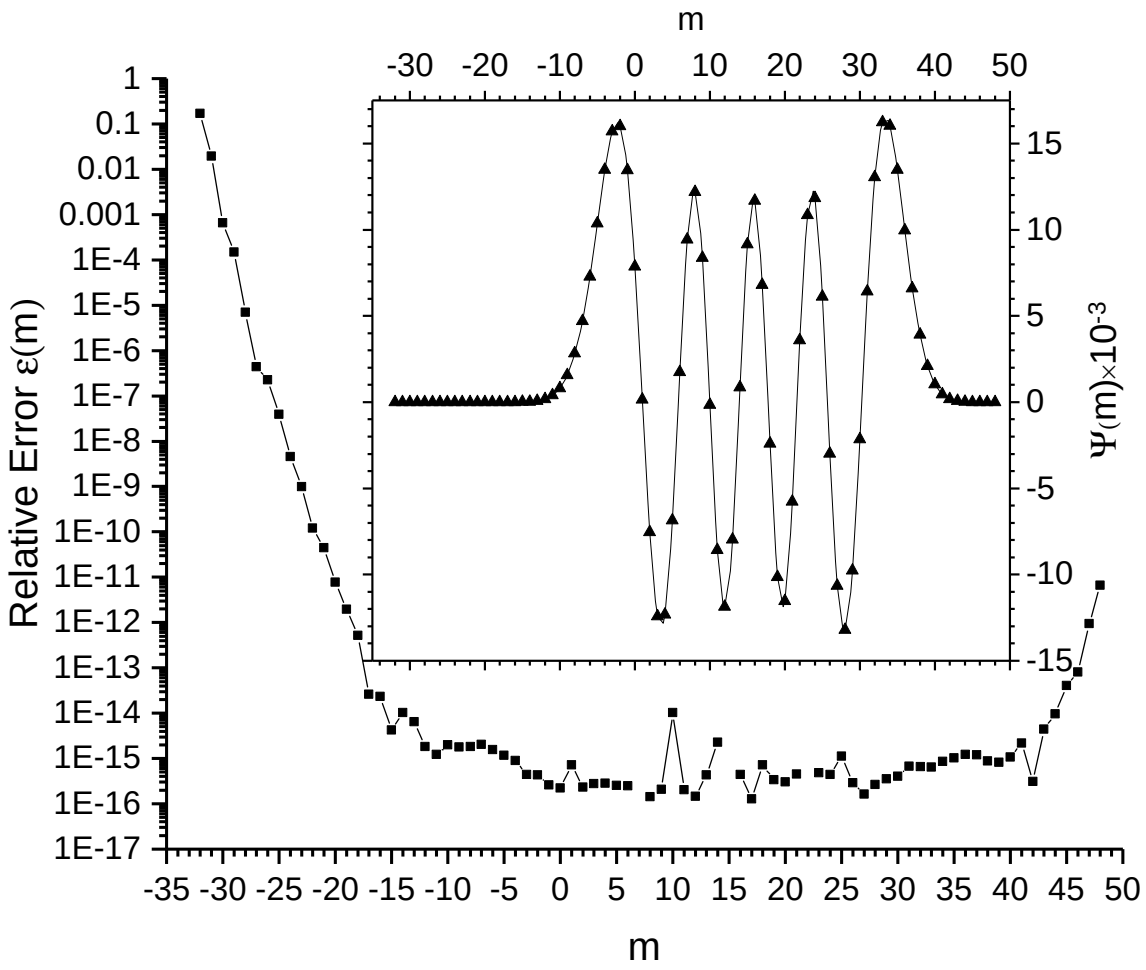

Figure 3.1: Numerical errors defined by Eq. 3.27 for evaluating $\psi(m)$ using the recursive method outlined in Ref. [79]. Excellent accuracy is achieved especially for m values that lie in the classical region [80]. The inset shows the values of $\psi(m)$. The solid lines connecting the data dots are plotted to guide the eyes.

a much simpler framework [79].

As an example, the relative numerical error $\epsilon(m)$ and the numerical realization of the $\psi(m)$ using the method in Ref. [79] are shown in Fig. 3.1. The numerical error $\epsilon(m)$ is defined as

$$\epsilon(m) = \left| \frac{\psi(m) - W_{3j}(m)}{W_{3j}(m)} \right| \tag{3.27}$$

where the W_{3j} is given by the exact value of the Wigner-3j symbol

$$W_{3j}(m) = \left\{ \begin{array}{ccc} 112 & 48 & 72 \\ -40 & m & -m+40 \end{array} \right\} \tag{3.28}$$

and the W_{3j} has none-zero values for $-32 \leqslant m \leqslant 48$.

3.2 Density Matrix and Master equations

3.2.1 A Three-level Example

In this section, I introduce the formalism of the master equations which allow us to connect the experimentally measured variables to the atomic properties. The setups are documented in many quantum mechanics text books with different notations and definitions. For the purpose of the future reference, I lay out the general approach used for the work described in this thesis and clear some confusions about different sign conventions used in the literatures and among different authors. The details are included in the Appendix B.

We describe the process in the "dressed atom" picture [81] (also known as the "field-interaction picture"; see details in the Appendix B), in which the Hamiltonian can be written as:

$$H = \frac{\hbar}{2}\begin{pmatrix} 0 & \Omega_p & 0 \\ \Omega_p & -2\Delta_1 & \Omega_c \\ 0 & \Omega_c & -2\Delta_2 \end{pmatrix} \tag{3.29}$$

and $\Delta_{1,2}$ are the laser detunings which include the first order Doppler shifts:

$$\begin{aligned} \Delta_1 &= \Delta_p + \boldsymbol{k}_p \cdot \boldsymbol{v} \\ \Delta_2 &= \Delta_p + \Delta_c + (\boldsymbol{k}_p + \boldsymbol{k}_c) \cdot \boldsymbol{v} \end{aligned} \tag{3.30}$$

where $\Delta_p = \omega_p - \omega_{21}$ and $\Delta_c = \omega_c - \omega_{32}$ are the probe and coupling laser detunings with respect to the zero velocity atoms.

The master equations are a set of differential equations that describe the time evolution of the density matrix $\rho(t)$ in a system governed by a Hamiltonian H. Unlike the Schrödinger equation, which is powerful enough to describe an isolated system, (i.e., all the quantum mechanical interactions are completely included in the Hamiltonian), the master equations allow the system under description to interact with the outside environment. These interactions are not completely described by the Hamiltonian H, but are given by the Lindblad operators acting on the density matrix ρ through the Lindblad function $L(\rho)$. For a multilevel quantum system, the master equations read:

$$\frac{\mathrm{d}}{\mathrm{d}t}\rho = -\frac{i}{\hbar}\left[H, \rho\right] + L\left(\rho\right) + L_d\left(\rho\right) \tag{3.31}$$

where $[*]$ represents the commutator and the Lindblad terms $L(\rho)$ and $L_d(\rho)$ are defined as

$$L(\rho) = \sum_{(i,j)} \left[-\frac{1}{2} \left(c_{ij}^{\dagger} c_{ij} \rho + \rho c_{ij}^{\dagger} c_{ij} \right) + c_{ij} \rho c_{ij}^{\dagger} \right] \tag{3.32}$$

$$L_d(\rho) = \sum_{(i,i)} -\frac{1}{2} \left(d_{ii}^{\dagger} d_{ii} \rho + \rho d_{ii}^{\dagger} d_{ii} \right) + d_{ii} \rho d_{ii}^{\dagger} \tag{3.33}$$

where $c_{ij} = \sqrt{\Gamma_{ij}} |i\rangle\langle j|$ represent the interactions that affect both the diagonal and off-diagonal density matrix elements. $d_{ii} = \sqrt{\gamma_i} |i\rangle\langle i|$ describe the interactions that affect only the off-diagonal elements, which are also called pure dephasing terms. $\sqrt{\Gamma_{ij}}$ and $\sqrt{\gamma_i}$ represent the interaction strengths respectively. All the definitions related to the Lindblad operators are summarized as follows:

$$\begin{aligned} c_{ij} &= \sqrt{\Gamma_{ij}} |i\rangle\langle j| \\ c_{ij}^{\dagger} c_{ij} &= \Gamma_{ij} |j\rangle\langle j| \\ d_{ii} &= \sqrt{\gamma_i} |i\rangle\langle i| \\ d_{ii}^{\dagger} d_{ii} &= \gamma_i |i\rangle\langle i| \end{aligned} \tag{3.34}$$

In the Rydberg-EIT system, a three-level ladder structure usually captures all the important physics, and the spontaneous decay between the level can be fully captured by the $L(\rho)$ term:

$$L(\rho) = \begin{pmatrix} \Gamma_{12}\rho_{22} & -\frac{\Gamma_{12}}{2}\rho_{12} & 0 \\ -\frac{\Gamma_{12}}{2}\rho_{21} & -\Gamma_{12}\rho_{22} & -\frac{\Gamma_{12}}{2}\rho_{23} \\ 0 & -\frac{\Gamma_{12}}{2}\rho_{32} & 0 \end{pmatrix} + \begin{pmatrix} 0 & 0 & -\frac{\Gamma_{23}}{2}\rho_{13} \\ 0 & \Gamma_{23}\rho_{33} & -\frac{\Gamma_{23}}{2}\rho_{23} \\ -\frac{\Gamma_{23}}{2}\rho_{31} & -\frac{\Gamma_{23}}{2}\rho_{32} & -\Gamma_{23}\rho_{33} \end{pmatrix} \tag{3.35}$$

where $\rho_{ij} = \langle i|\rho|j\rangle$ is the matrix elements of the density matrix, Γ_{12} is the decay rate of the intermediate state $|2\rangle$, and Γ_{23} is the decay rate of the Rydberg state $|3\rangle$.

Additional pure dephasing and line broadening effects can be included in the $L_d(\rho)$ as follows

$$L_d^{total} = L_d^{Laser} + L_d^{Ryd} = \begin{pmatrix} 0 & -\tilde{\gamma}_p\rho_{12} & -(\tilde{\gamma}_{cp} + \frac{\gamma_3}{2})\rho_{13} \\ -\tilde{\gamma}_p\rho_{21} & 0 & -(\tilde{\gamma}_c + \frac{\gamma_3}{2})\rho_{23} \\ -(\tilde{\gamma}_{cp} + \frac{\gamma_3}{2})\rho_{31} & -(\tilde{\gamma}_c + \frac{\gamma_3}{2})\rho_{32} & 0 \end{pmatrix} \tag{3.36}$$

where $\tilde{\gamma}_p$, $\tilde{\gamma}_c$ and $\tilde{\gamma}_{cp}$ are the laser-induced dephasing due to laser field fluctuations. γ_3 rep-

resents the dephasing of the Rydberg states, which can be caused by the collision between the Rydberg atom and an impurity-tracer atom in the cell or by external electromagnetic fields fluctuations. Interaction time broadening can also be included in this term. Typical magnitudes of these parameters are as follows:

$$\tilde{\gamma}_{p,c,cp} \simeq 2\pi \times 1\text{MHz} \tag{3.37}$$

$$\gamma_3 \simeq 2\pi \times 0.1\text{MHz} \tag{3.38}$$

3.2.2 Single Atom Picture and Ensemble Averages

The single-atom picture described in the last section captures the most interesting physics in the system, but its predictions usually cannot be directly compared to experimentally measured results. Measured quantities in experiments are inevitably subject to various inhomogeneities inherent to the macroscopic nature of experimental setups. Additional care must be taken when interpreting measurement data qualitatively. In this section, I heuristically describe how to link the microscopic single-atom picture to macroscopically measured signals.

Let us begin with a discussion of the Rabi frequencies $\Omega_{p,c}$ in the Hamiltonian equation Eq. 3.29. In many cases, the atoms are excited by laser beams with Gaussian amplitude profiles in the transverse direction:

$$\boldsymbol{E} = \boldsymbol{E}_0 \exp\left(-\frac{r^2}{w_0^2}\right) \tag{3.39}$$

In general the electric field amplitude $\boldsymbol{E}_0$ can contain explicit time dependence and phase information $\phi(t)$ with polarization $\hat{\boldsymbol{\epsilon}}$:

$$\boldsymbol{E}_0(t) = \frac{1}{2}\hat{\boldsymbol{\epsilon}} E_0(t)\left[e^{-i\omega t + i\phi(t)} + e^{i\omega t - i\phi(t)}\right] \tag{3.40}$$

where amplitude $E_0(t)$ is a real valued quantity.

Due to the Gaussian spatial dependence, the Rabi frequencies are not spatially uniform:

$$\Omega(r) = \Omega_0 \exp\left(-\frac{r^2}{w_0^2}\right) \tag{3.41}$$

The peak Rabi frequency Ω_0 is defined as

$$\Omega_0 = \frac{e\left\langle i\right| \hat{\boldsymbol{r}} \cdot \boldsymbol{E}_0 \left|j\right\rangle}{\hbar} = \frac{d_{ij} E_0}{\hbar} \tag{3.42}$$

where $\hat{\boldsymbol{r}}$ the electron position operator and $|i\rangle$, $|j\rangle$ are the two atomic states coupled by the laser field. d_{ij} represents a real dipole matrix element which can be evaluated using the Rydberg basis functions in Eq. 3.4. See Appendix. C for further details.

Under normal experimental conditions, the probe laser power is monitored and recorded during laser frequency scans. The initial power of the probe beam $P_{prb,0}$ is

$$\begin{aligned} P_{prb,0} &= \frac{c\epsilon_0}{2} E_{prb,0}^2 \int_0^{+\infty} e^{-2\left(r^2/w_{prb,0}^2\right)} 2\pi r \mathrm{d}r \\ &= \frac{c\epsilon_0}{4} E_{prb,0}^2 w_{prb,0}^2 \pi \\ &= \frac{c\epsilon_0}{4} w_{prb,0}^2 \pi \left(\frac{\Omega_{prb,0}\hbar}{d_{prb}}\right)^2 \end{aligned} \tag{3.43}$$

In the last step, the following relation is used:

$$\Omega_{prb,0} = \frac{2d_{prb}}{\hbar}\sqrt{\frac{1}{c\epsilon_0}}\sqrt{\frac{P_{prb,0}}{w_{prb,0}^2\pi}} \tag{3.44}$$

The probe laser light is strongly scattered during its propagation through atomic vapor. After the propagation length L, the total change in the beam intensity ΔS can be estimated as

$$\Delta S = \int_0^L \left(-\frac{1}{2} N_0 \hbar\omega_{prb}\Gamma_{21}\langle\rho_{22}\rangle\right) \mathrm{d}z \tag{3.45}$$

where N_0 is the atomic vapor number density, Γ_{21} is the intermediate level scattering rate and $\langle * \rangle$ represents an ensemble average of the single-atom density matrix element. The negative sign indicates the intensity loss in this process. Hence, the total change of power is

$$\begin{aligned} \Delta P &= P_{prb,L} - P_{prb,0} \\ &= \int_0^{\infty} \Delta S \; 2\pi r \mathrm{d}r \\ &= -\frac{1}{2} N_0 \hbar\omega_{prb}\Gamma_{21} \int_0^{\infty}\int_0^{L} \langle\rho_{22}\rangle \; 2\pi r \mathrm{d}r\mathrm{d}z \end{aligned} \tag{3.46}$$

Using Eq. 3.46 and Eq. 3.44, we define the transmission signal of the probe laser as

$$\begin{aligned} T_{prb} &= \frac{P_{prb,L}}{P_{prb,0}} = 1 + \frac{\Delta P_{prb}}{P_{prb,0}} \\ &= 1 - \alpha_{prb,0}\frac{1}{2\pi w_{prb,0}^2}\left(\frac{\Gamma_{21}}{\Omega_{prb,0}}\right)^2 \int_0^{\infty}\int_0^{L} \langle\rho_{22}\rangle \; 2\pi r \mathrm{d}r\mathrm{d}z \end{aligned} \tag{3.47}$$

where the absorption coefficient $\alpha_{prb,0}$ is defined as

$$\alpha_{prb,0} = \frac{4N_0\omega_{prb}d_{prb}^2}{c\hbar\epsilon_0\Gamma_{21}} = \frac{4N_0k_{prb}d_{prb}^2}{\hbar\epsilon_0\Gamma_{21}} \tag{3.48}$$

The single-atom matrix density element ρ is determined by the master equation Eq. 3.31. In general, the density matrix $\rho(t, \boldsymbol{r}, v)$ can have explicit dependence on time t (e.g. modulated excitations or limited interaction time), macroscopic position $\boldsymbol{r}$ (e.g. inhomogeneities in Rabi frequency or atomic energy level shifts) and Doppler velocity v through Doppler shifts. These quantities must be averaged according to certain probabilities in order to get the experimentally measurable steady state quantity, in our case, the transmission of the probe laser signal T_{prb}. Therefore, the ensemble average term $\langle\rho\rangle$ can be written as

$$\langle\rho\rangle = \int \mathrm{d}t \int \mathrm{d}\boldsymbol{r} \int \mathrm{d}\boldsymbol{v}\ \rho(t, \boldsymbol{r}, \boldsymbol{v})\mathcal{P}(t)\mathcal{P}(\boldsymbol{r})\mathcal{P}(\boldsymbol{v}) \tag{3.49}$$

where $\mathcal{P}(t)$, $\mathcal{P}(\boldsymbol{r})$and $\mathcal{P}(v)$ are the normalized probability distribution functions. In particular, for a two-dimensional (2D) problem, interaction-time limited $\mathcal{P}(t)$ can be found in Eq. 1.21. For a frequency modulated case where the laser detuning in Eq. 3.30 has a time dependence of $\sim \sin\omega_m$ with a modulation frequency ω_m, in a steady state case, the time should be averaged over one modulation period with a uniform distribution $\mathcal{P}(t) = \omega_m/2\pi$. The spatial probability distribution $\mathcal{P}(\boldsymbol{r})$ is usually considered as a uniform distribution over the whole cell volume. The velocity distribution $\mathcal{P}(\boldsymbol{v})$ follows the Maxwell-Boltzmann distribution as shown in Eq. 1.13.

This concludes the heuristic presentation of how a microscopic single-atom description can be used to describe experimentally measured macroscopic quantities. Formal approaches and potential problems linked to these procedures can be found in quantum optics textbooks, such as Ref.[82].

3.2.3 Maxwell-Bloch equations and Nonlinear Optics

In the last section of this chapter, I briefly summarize some widely used results regarding the Maxwell-Bloch equations, which describe light propagation behavior inside a dielectric medium, much of which is directly applicable to atomic vapor experiments, such as Beer's law of absorption.

Starting with the Maxwell equations and using slowly varying envelope approximation, the second-order Maxwell equations can be approximated by a first-order equation as follows:

$$[\partial_t + c\partial_z]\,\tilde{\boldsymbol{E}}(z,t) = i\frac{\omega}{\epsilon_0}\tilde{\boldsymbol{P}} \tag{3.50}$$

where $\tilde{\boldsymbol{E}}$ is the slowly varying envelope function of the total electric field $\boldsymbol{E}$ with carrying wave frequency ω and wavenumber k defined as

$$\boldsymbol{E}(z,t) = \frac{1}{2}\tilde{\boldsymbol{E}}(z,t)e^{i(kz-\omega t)} + \text{c.c} \tag{3.51}$$

The polarization of the medium is assumed to be driven by the electric field over the same timescale. The envelope polarization function $\tilde{\boldsymbol{P}}$ of the total medium polarization $\boldsymbol{P}$ can be defined in the same fashion as in the case of the electric field:

$$\boldsymbol{P}(z,t) = \tilde{\boldsymbol{P}}(z,t)e^{i(kz-\omega t)} + \text{c.c} \tag{3.52}$$

Please note the $1/2$ difference in Eq. 3.51 and Eq. 3.52

The total medium polarization $\boldsymbol{P}$ can be calculated by an ensemble average of the microscopic dipoles

$$\begin{aligned}\boldsymbol{P} &= N_0\langle\hat{\boldsymbol{d}}\rangle \\ &= N_0\text{Tr}\left[\hat{\rho}\hat{\boldsymbol{d}}\right]\end{aligned} \tag{3.53}$$

If we evaluate Eq. 3.53 in the "dressed atom" picture (also known as a field-interaction picture), we can find that

$$\tilde{\boldsymbol{P}}_{nm} = N_0\boldsymbol{d}_{mn}\rho_{nm} \tag{3.54}$$

where the density matrix ρ_{nm} follows the master equation Eq. 3.31 introduced in Sec. **??**

Using Eq. 3.54 and Eq. 3.50, we find that in the steady-state condition, the propagation of the probe laser $\boldsymbol{E}^{st}_{prb}$ (which is nearly resonant with the transition between the lower two quantum levels $|1\rangle$ and $|2\rangle$) is

$$\partial_z\boldsymbol{E}^{st}_{prb} = i\frac{N_0\boldsymbol{d}_{12}\omega_{21}}{c\epsilon_0}\rho^{st}_{21} \tag{3.55}$$

Recalling the intensity absorption given by Beer-Lambert's law,

$$I(z) = I_0e^{-\alpha z} \tag{3.56}$$

and comparing Eq. 3.56 and Eq. 3.55, the absorption coefficient α can be defined as

$$\alpha = 2\frac{N_0|\boldsymbol{d}_{12}|\omega_{21}}{c\epsilon_0}\Im\left[\rho_{21}^{st}\right] \tag{3.57}$$

CHAPTER 4

Rydberg EIT Measurements in High Magnetic Fields

4.1 Introduction

As mentioned in Sec. 2.5, the Rydberg atoms are very sensitive to external magnetic fields due to its large sizes. These effects are prominent especially in the diamagnetic region. An important feature of Rydberg-EIT in strong B fields is the large diamagnetism of the Rydberg state, which enables the detection of small variations on a large magnetic field background. Since the diamagnetic contribution to the differential dipole moment scales as $n^4 \times B$, the sensitivity of this measurement increases with B and it can be increased by going to higher n.

In magnetic fields $B > 2n^{-4}$ at.un. (0.4 T for principal quantum number $n = 33$), the diamagnetic term dominates and mixes states with different angular momentum [63]. In this work, we employ the $|33S_{1/2}, m_j = 1/2\rangle$ Rydberg state whose interaction with the B field includes a Zeeman (linear) and a diamagnetic (quadratic) term. In a 0.7 Tesla field, the diamagnetic interaction accounts for about 70% of the differential magnetic dipole moment $-dE_r/dB = 3.06\ \mu_B$ (E_r is the Rydberg-state energy). In this field, all involved states are in the hyperfine Paschen-Back regime, and the energy separations between the magnetic states are larger than the spectroscopic Doppler width.

EIT in vapor cells has been employed to investigate Cs Rydberg atoms in magnetic fields up to ~ 0.01 T [83] and Rb $5D_{5/2}$ atoms in fields up to ~ 0.6 T [84, 85]. The method presented in the next sections offers two advantages in high-magnetic-field measurements. First, the diamagnetic interaction gives rise to an enhanced differential dipole moment, enabling measurement of small changes of a large magnetic field. Second, simultaneous measurements of field-induced level shifts for both $^{85}\mathrm{Rb}$ and $^{87}\mathrm{Rb}$ isotopes affords high absolute accuracy in magnetic field measurements based on relative line separations.

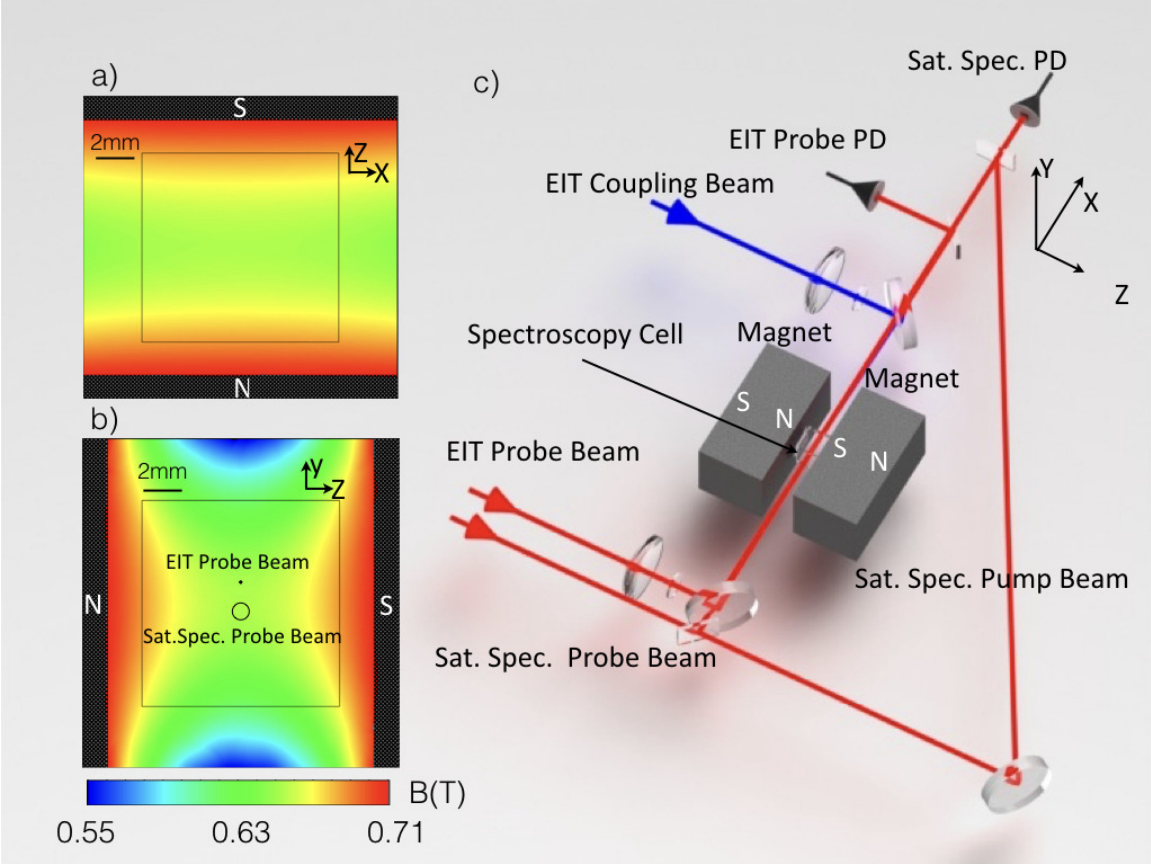

Figure 4.1: (color online) Calculation of the magnetic field B in the x-z plane (a) and y-z plane (b). The filled black regions represent the poles of the bar magnets. The open black square represents the inner boundary of the spectroscopy cell. (c) Illustration of the experimental setup, including an EIT channel and a saturation spectroscopy channel. The two channels are separated in the y direction.

4.2 Experimental Setups and Methods

Two N52 Neodymium permanent magnets are used to produce the magnetic field. For the specific geometry adopted in the experimental setups, the B field strength is also calculated by using a finite-element analysis software (ANSYS Maxwell). Figures 4.1(a) and 4.1(b) show cuts of the magnetic field. A spectroscopic cell filled with a natural Rb isotope mix is placed between the magnets. In order to increase the optical absorption, the cell temperature is maintained at ~ 45 °C by heating both the cell and surrounding magnets.

The optical setup includes two measurement channels: a Rydberg-EIT and a saturation spectroscopy (Sat. Spec.) channel. As shown in Fig. 4.1(b) and (c), the channels are parallel to the x-axis and separated by 1.85 mm in the y-direction. The Rydberg-EIT probe beam is focused to a waist of ~ 40 μm ($1/e^2$ radius) and has a power of ~ 1 μW. The

coupling beam has a waist of $\sim 100\ \mu\mathrm{m}$ and a power of $\sim 35\ \mathrm{mW}$. The polarizations of the coupling and probe beams are both linear and parallel to the magnetic field along z. Both probe beams in the two channels are frequency-modulated by the same acousto-optical modulator. The probe modulation results in a minor broadening of the EIT lines that, in future implementations, can be avoided by only modulating the Sat. Spec. probe beam. The demodulated Sat. Spec. signals are used to lock the probe laser beam to one of the $5S_{1/2}$ to $5P_{3/2}$ transitions shown in Fig. 4.2(a).

The Rydberg-EIT coupling laser is linearly scanned over a range of 4.5 GHz at a repetition rate of ~ 1 Hz. The scans are linearized to within a $1\ \mathrm{MHz}$ residual uncertainty using the transmission peaks of a temperature-stabilized Fabry-Perot cavity. The coupler laser is chopped at $33\ \mathrm{kHz}$. The EIT transmission signals are recovered by a digital lock-in referenced to the chopping frequency.

4.3 Saturation Spectroscopy in High-Magnetic fields

At $B \sim 1\ \mathrm{T}$, the energy levels are shifted by up to several tens of GHz. The relevant ground- ($5S_{1/2}$) and intermediate-state ($5P_{3/2}$) energy levels and calculations of their field-induced shifts are plotted in Figs. 4.2(b) and 4.2(c). In order to frequency-stabilize the EIT probe laser to a $5S_{1/2}$ to $5P_{3/2}$ transition, we implement a Sat. Spec. channel in the high-B region, as illustrated in Fig. 4.1. The right panel of Fig. 4.2(a) shows the measured saturated absorption signals. Over the displayed probe frequency range, the spectrum consists of four $^{87}\mathrm{Rb}$ lines (peaks α, β, δ, and ϵ) and a $^{85}\mathrm{Rb}$ line (peak γ). In the Paschen-Back limit, cross-over dips are not present because 1) the m_i quantum number is conserved in all optical transitions ($\Delta m_i = 0$), and 2) for π-polarized light the selection rule $\Delta m_j = 0$ applies. Also, the separations between the fine structure transitions with different m_j exceed the Doppler width; here, we are selecting the $m_j = 1/2$ levels.

Due to the differences in the hyperfine coupling of $^{87}\mathrm{Rb}$ and $^{85}\mathrm{Rb}$ (magnetic dipole coupling strength, electric quadrupole coupling strength, nuclear spins and isotope shifts), the energy levels of each isotope exhibit differential shifts. In our calculation, we follow references from Professor Daniel A. Steck, "Rubidium 85 D Line Data", (available online at http://steck.us/alkalidata (revision 2.1.6, 20 September 2013)) and references therein. The gap ratio $\Delta_{\gamma\delta}/\Delta_{\beta\gamma}$ is found to be sensitive to the magnetic field at this scale such that we can determine the magnetic field strength in the Sat. Spec. channel to exactly to be $0.71\ \mathrm{T}$. This is indicated by the vertical dashed line in the left panel of Fig. 4.2(a).

At the end of the scan range, the peak positions deviate slightly from their locations expected for $0.71\ \mathrm{T}$. This is caused by a slight nonlinearity of the mechanical-grating

scan of the external-cavity diode laser. This nonlinearity does not affect the Rydberg-EIT experiment, discussed in the next paragraph, because the probe laser is locked to a Sat. Spec. peak (five out of six are shown in Fig. 4.2(a)) and has a fixed frequency.

4.4 Rydberg-EIT Spectra in High Magnetic Fields

To investigate Rydberg-EIT in the high-B regime, we frequency-stabilize the π-polarized EIT probe laser to a $|5S_{1/2}, m_j = 1/2, m_i\rangle \rightarrow |5P_{3/2}, m_j = 1/2, m_i\rangle$ transition and access the $|33S_{1/2}, m_j = 1/2, m_i\rangle$ Rydberg state with a coupling laser of the same polarization. Figures 4.3(a-f) show the Rydberg-EIT spectra measured at $B = 0.70$ T.

For Rydberg-EIT in a vapor cell, the atomic Maxwell velocity distribution needs to be considered, as well as the Doppler effect induced by the wavelength mismatches of the probe and coupler lasers [3]. The details are outlined in the Subsection 1.2.2. Applying these principles to this particular experimental situation where an external field shifts the ground, intermediate and Rydberg levels by ΔE_g, ΔE_e, and ΔE_r, respectively, the coupling laser detunings, $\Delta\omega_c$, at which the EIT resonances occur are:

$$\hbar\Delta\omega_c = \Delta E_r + \left(\frac{\lambda_p}{\lambda_c} - 1\right)\Delta E_e - \frac{\lambda_p}{\lambda_c}(\Delta E_g + \hbar\Delta\omega_p) \tag{4.1}$$

where λ_p and λ_c are the wavelengths of the probe and coupling lasers, and $\Delta\omega_p$ is the probe-laser detuning. As shown in the Section 1.2.2, the wavelength-dependent scaling factors are deduced by requiring resonance on both the lower and the upper transitions in the three-level cascade structure.

The shifts ΔE_g, ΔE_e and ΔE_r in Eq. 4.1 are plotted as a function of B in Figs. 4.3(g-i). For S Rydberg states in Rb, which are non-degenerate and fine-structure-free, the Rydberg level shift (in atomic units) is [63]

$$\Delta E_r = \frac{m_s B}{2} + \frac{B^2}{8}\langle nlm_l|\hat{r}^2 \sin^2\hat{\theta}|nlm_l\rangle \quad , \tag{4.2}$$

where $l, m_l, \text{and } m_s$ are angular momentum, magnetic orbital and spin quantum numbers, respectively. The coordinates r and θ are spherical coordinates of the Rydberg electron (**B** points along z). The first term on the right side of Eq. 4.2 represents the paramagnetic term of the electron spin, and the second term is the diamagnetic shift. For $|33S_{1/2}, m_j = 1/2\rangle$ atoms in a 1 T field, the differential dipole moment is $3.06\mu_B$, implying that the diamagnetic contribution is about twice as large as the spin dipole moment. This fact, as well as the λ_p/λ_c enhancement factor of the ground state shift (ΔE_g) shown in Eq. 4.1, make the Rydberg-EIT resonances highly sensitive to small variations in a high-magnetic-

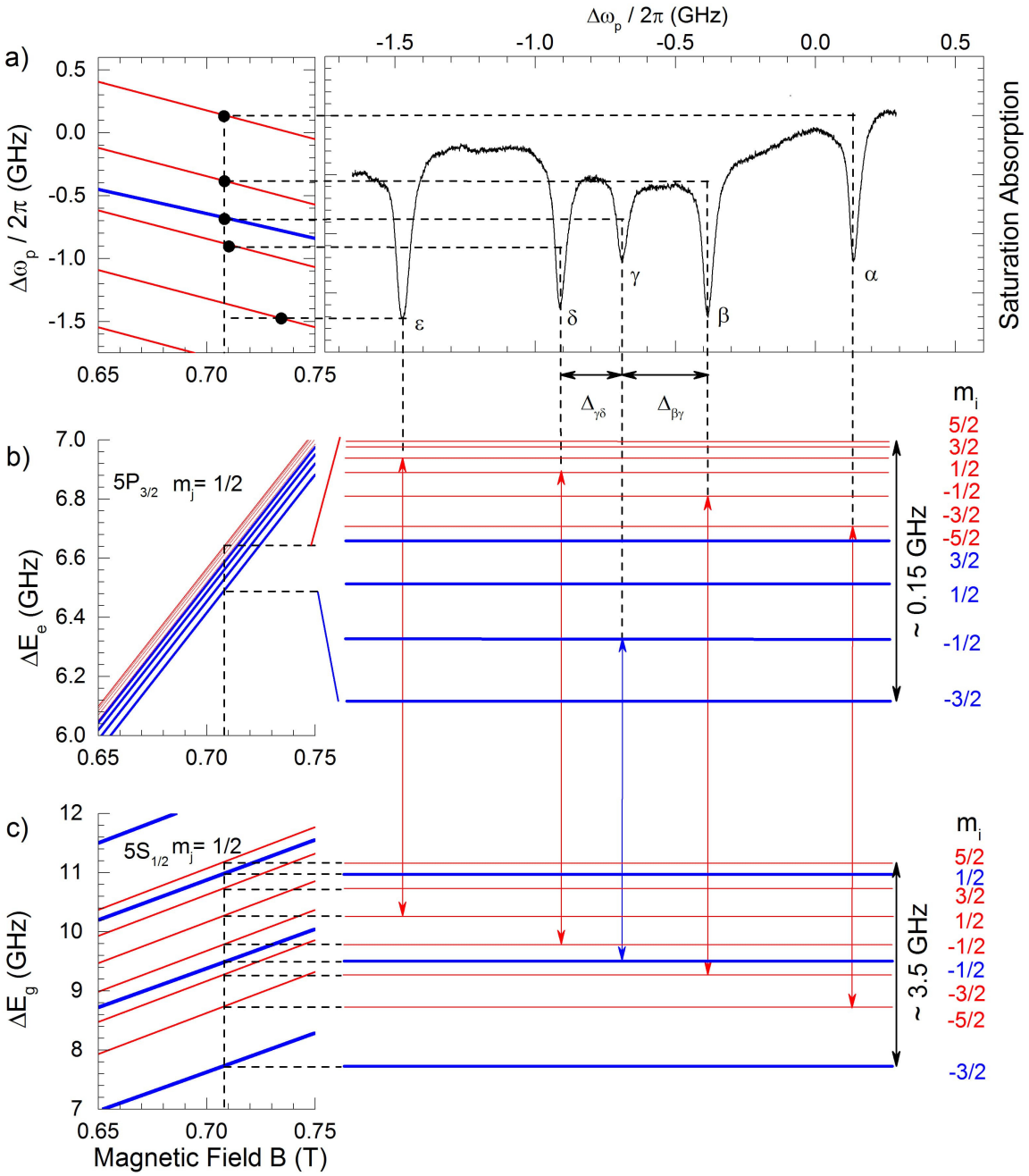

Figure 4.2: (color online) (a) Saturation absorption signal in a 0.71 T magnetic field versus probe frequency detuning $\Delta\omega_p$(right panel) and calculated magnetic-field-induced level shifts (left panel). The frequency is measured relative to the magnetic-field-free ^{87}Rb $5S_{1/2}, F = 2$ to $5P_{3/2}, F = 3$ transition, where $\Delta\omega_p = 0$. The linewidth is dominated by inhomogeneous broadening due to the magnetic-field inhomogeneity. (b) Schematic of atomic energy levels for intermediate state and (c) ground state. The states are labeled by the quantum numbers m_i and m_j (which are good quantum numbers in the Paschen-Back regime). Energy levels of ^{85}Rb and ^{87}Rb are shown in thin red and bold blue, respectively.

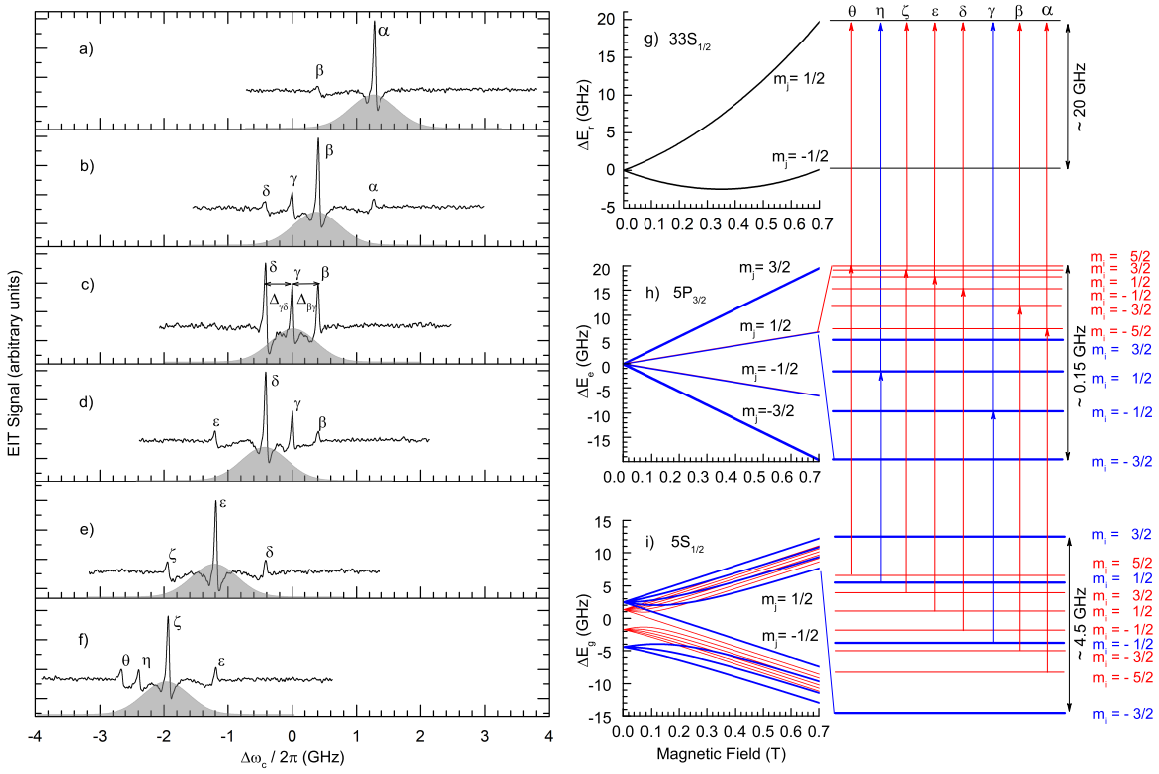

Figure 4.3: (color online) (a) to (f) EIT transmission signals for the EIT probe laser locked to a Sat. Spec. peak. (The Sat. Spec. peaks α to ϵ are shown in Fig. 4.2(a).) The shaded areas indicate the weighting due to the Maxwell velocity distribution (see discussion of Eq. (3)). Signals corresponding to the same EIT transition are labeled with the same Greek letter in the spectra.Same Greek letters are used to label the corresponding lower transition in Fig. 4.2. The coupling laser detuning is given relative to peak γ. The spectra are shifted such that shared EIT peaks are aligned, as determined using cross-correlation functions of neighboring scans. Calculated energy level shifts in the Paschen-Back regime for the (g) Rydberg, (h) intermediate and (g) ground states. The transitions corresponding to the EIT resonances in panels (a-f) are indicated by vertical arrows and labeled with the same Greek letter. Transitions in $^{85}\mathrm{Rb}$ and $^{87}\mathrm{Rb}$ are coded with thin red and bold blue lines, respectively.

field background (see Sec. 4.5).

Eight out of the ten EIT resonances that exist for the given polarization case are present in the frequency range covered by the coupling laser in Figs. 4.3(a-f). Every resonance satisfies Eq. 4.1 and has a well-defined atomic velocity, v, given by

$$v = \frac{\lambda_p}{2\pi}\left(\Delta\omega_p + \frac{\Delta E_g - \Delta E_e}{\hbar}\right) \tag{4.3}$$

For an EIT resonance to be visible in a spectrum with given $\Delta\omega_p$, ΔE_g and ΔE_e, the velocity v that follows from Eq. 4.3 must be within the Maxwell velocity distribution. Since the probe laser is locked to one of the resonances shown in Fig. 4.2 in every EIT spectrum, each spectrum has a strong resonance at its center for which Eq. 4.3 yields $v \approx 0$ (where the Maxwell velocity distribution peaks). For the neighboring EIT resonances, the velocities are several hundreds of meters per second, due to their large $\Delta\omega_p$. (It is seen in Fig. 4.2 that the spacings between neighboring probe-laser resonances are several hundred MHz.) Since the rms velocity of the Maxwell velocity distribution in one dimension is about 170 m/s, the number of atoms contributing to the neighboring EIT resonances is greatly reduced relative to that of the center resonance. The finite width of the velocity distribution therefore limits the number of resonances observed in each scan to 2-4.

According to Eq. 4.1, the paramagnetic shifts (which are all in the Paschen-Back regime) and the diamagnetism of the Rydberg atoms in strong B, lead to highly magnetic-field-sensitive shifts of the Rydberg-EIT resonances. For example, the cascade $|5S_{1/2}, m_j = -1/2\rangle \rightarrow |5P_{3/2}, m_j = -1/2\rangle \rightarrow |33S_{1/2}, m_j = 1/2\rangle$ generates an EIT peak that shifts at 7 MHz/Gauss. The EIT resonances accessed in this work(boxed region in Fig. 4.4(a)) shift at about 2.5 MHz/Gauss.

Fig. 4.4 shows calculated B-field induced Rydberg-EIT resonance shifts of both $^{85}\mathrm{Rb}$ (thin red lines) and $^{87}\mathrm{Rb}$ (bold blue lines). The shifts in Eq. 4.1 are highly dependent on the B field, as shown in Fig. 4.3(g-i). This leads to B-field-dependent differential shifts of the EIT lines of the two isotopes. This feature arises from the Paschen-Back behavior of $|5S_{1/2}\rangle$ and $|5P_{3/2}\rangle$. The arrows in Fig. 4.4(b) indicate the frequency splittings, the ratio of which we use to extract the B field strength. We map the splitting ratio from the experimental data in Fig. 4.3(c) (horizontal arrows $\Delta_{\beta\gamma}/\Delta_{\gamma\delta} = 0.9685 \pm 0.0037$), using the function shown in Fig. 4.4(c), onto a magnetic field of $B = 0.6960 \pm 0.0008$ T (maximum field in the probe region). The quoted field uncertainty follows from the spectroscopic uncertainty of the peak centers of $\lesssim 1$ MHz (the probe laser linewidth) and standard error propagation in the mapping. Note the B fields derived from the Sat. Spec. and the EIT spectrum are slightly different because the respective laser beams pass through different regions of the

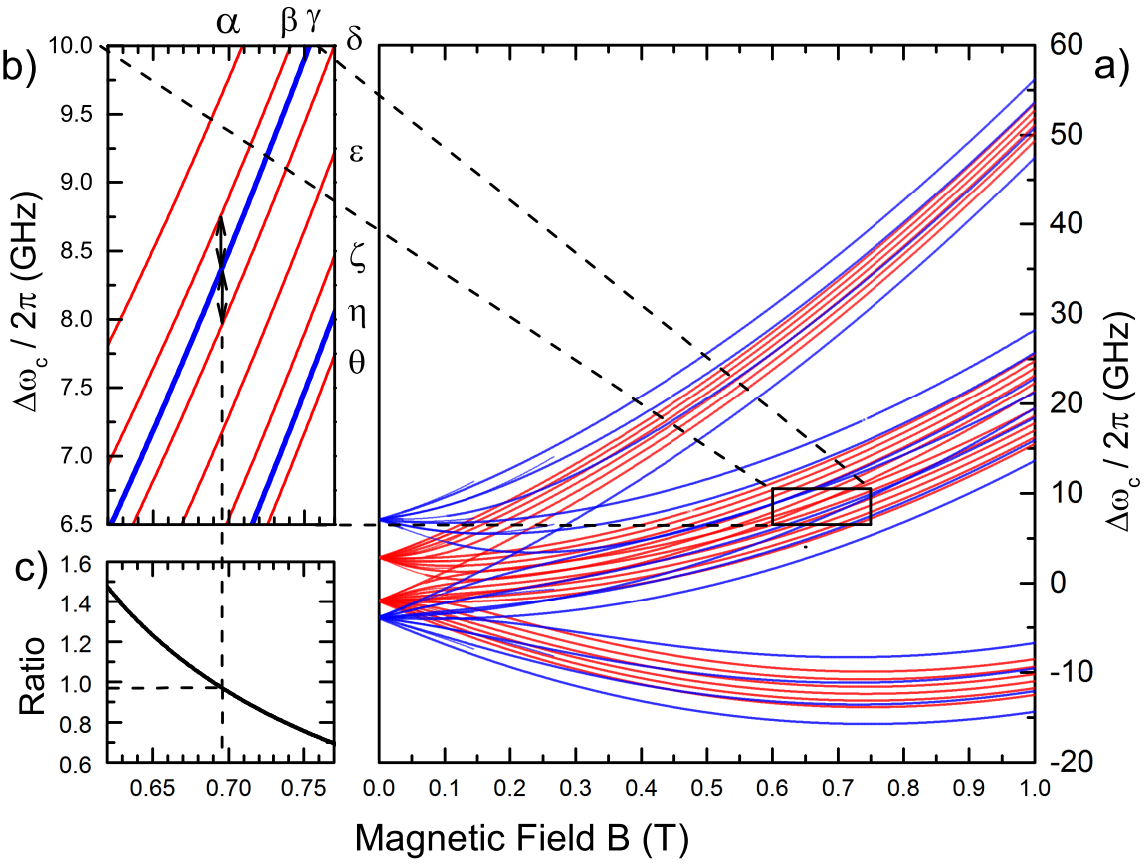

Figure 4.4: (a) EIT line positions according to Eq. 4.1 as a function of B for $\pi - \pi$ or $\pi - \sigma$ transitions from $|5S_{1/2}\rangle$ through $|5P_{3/2}\rangle$ to $|33S_{1/2}\rangle$ for ^{85}Rb (thin red lines) and ^{87}Rb (bold blue lines). (b) Zoom-in of the transitions (α to θ) observed in this work. The arrows indicate the frequency separations $\Delta_{\beta\gamma}$ and $\Delta_{\gamma\delta}$ we use to extract the B field. (c) Splitting ratio $\Delta_{\beta\gamma}/\Delta_{\gamma\delta}$ vs B.

B field (see Fig. 4.1(b)).

4.5 Spectra Simulation and discussions

The spectra in Figs. 4.3 and 4.5 show that the EIT lines are asymmetric. This is in part due to the B-field inhomogeneity, which affect the line width (line-broadening), shift the line centers (line-pulling), and cause the characteristic triangular EIT line shape. The origin of these effects needs to be reasonably well understood to confirm the accuracy of our B-field measurement.

In order to quantitatively model the spectra, we use a Monte Carlo simulation to find the power loss of the probe beam due to the photon scattering by the atoms in the inhomogeneous B field. The atoms are excited by laser beams with Gaussian profiles. The

steady-state of the excited-state population is calculated using the Lindblad equation for the three-level cascade structure [86] with position-dependent Rabi frequencies and magnetic-field-dependent level shifts. The essentials are outlined in the Sec. 3.2. In this particular simulation, we randomly pick the atomic positions $\mathbf{R}_i = (X_i, Y_i, Z_i)$ from a uniform distribution truncated at the cell boundaries, and velocities in x direction from a one-dimensional Maxwell velocity distribution for 300 K (i is the atom counting index). The B-fields at positions $\mathbf{R}_i$ are given by the results of the FEM field calculation shown in Fig. 4.1 and in the inset of Fig. 4.5(c). The field-induced energy-level shifts are taken from data sets used in Figs. 4.3(g-i). The probe and coupler Rabi frequencies, $\Omega_p(\mathbf{R}_i)$ and $\Omega_c(\mathbf{R}_i)$, are determined by the beam parameters given in Sec. 4.2 with center Rabi frequencies, $\Omega_{p0} = 2\pi \times 11$ MHz and $\Omega_{c0} = 2\pi \times 6.8$ MHz. Further, we consider the natural isotopic mix and assume a uniform distribution of the atoms over all m_i states. The probe detuning is set to $\Delta\omega_p = (\Delta E_e - \Delta E_g)/\hbar$ for the peak δ at $B = 0.6960$T, the maximum B field along the beam path, and the coupler detuning is varied. The probe modulation (5 MHz peak to peak) is also taken into account. The spectrum is simulated using a sample of 10^6 randomly selected atoms. The averaged simulated spectrum is shown in Fig. 4.5(b).

The simulation agrees very well with the experimental spectrum, as shown in Figs. 4.5(a) and (b). Here, the B field inhomogeneity (see Fig. 4.1) dominates the line broadening. The B-field variation in the probe volume is about 3.5×10^{-3} T, which corresponds to a line broadening of ~ 100 MHz (vertical dashed lines in Fig. 4.5). The simulation also reveals that the line centers are pulled by the same amount of -10 MHz relative to the theoretical line positions expected for the maximum B field. Therefore, the ratio $\Delta_{\beta\gamma}/\Delta_{\gamma\delta}$ in Fig. 4.5(b), which we have used to determine the magnetic field in Fig. 4.4(c), is unaffected by the line-pulling.

The only free parameter in the simulation is the decoherence rate of the Rydberg state. We have found that this parameter has a profound effect on the depth of the side-dips next to all EIT peaks. In order to explain the experimentally observed spectra, we have to assume a Rydberg dephasing rate of $2\pi \times 50$ MHz, with an uncertainty of ± 10 MHz. This dephasing rate is unexpectedly high, when compared to other Rydberg-EIT and Autler-Townes work [87, 88]. This large dephasing rate might be due to free charges generated by Penning and thermal ionization of Rydberg atoms and magnetic trapping of the charges [89].

In the simulation we ignore optical pumping from the intermediate $|5P_{3/2}, m_j = 1/2\rangle$ into the ground level $|5S_{1/2}, m_j = -1/2\rangle$. We believe this is justified by the short atom-field interaction time (~ 200 ns), which allows only a few scattered photons per atom. We note that any optical pumping effects will only lead to a global attenuation of the EIT line strengths. Further, the EIT leads to a reduction in the probe-photon scattering rate, mod-

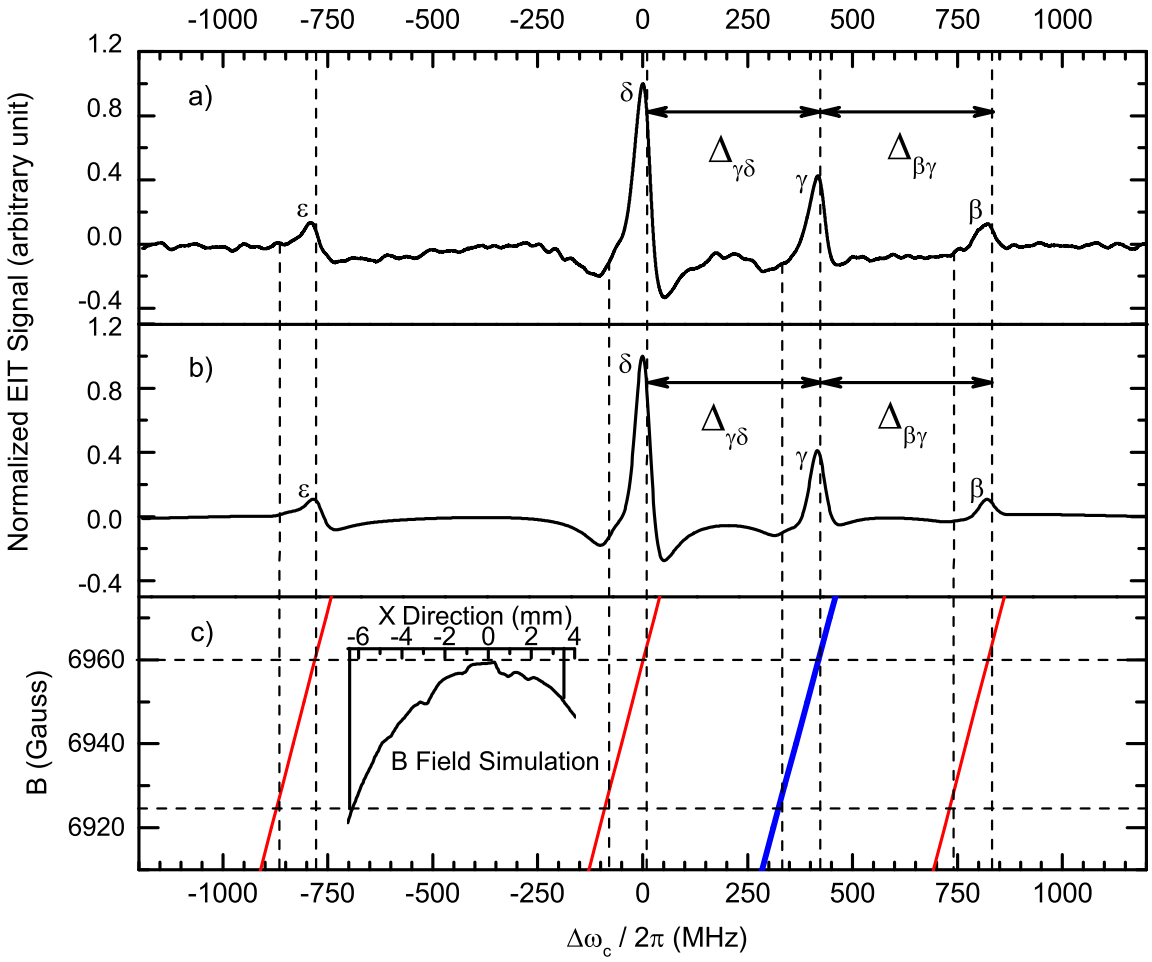

Figure 4.5: (a) Zoom-in look of Fig. 4.3(d). (b) Monte Carlo simulation of the EIT spectrum shown in (a). (c) The magnetic field induced EIT resonance shifts that contribute to the spectroscopic line-broadening and pulling for peaks ϵ, δ, γ, and β. The vertical dashed lines indicate the line shape extension range resulting from the inhomogeneous magnetic field inside the cell. (Power broadening is on the order of 20 MHz). The inset shows FEM simulated magnetic fields distribution along x axis within the cell boundaries indicated by vertical black lines. This distribution is off centered by 1.5 mm to reflect possible asymmetry in the experimental setup.

ifying the optical pumping near the EIT resonances [90]. In our case this is not expected to substantially alter the EIT line shapes. Optical-pumping could be, in principle, entirely avoided by selecting the $|5S_{1/2}, m_j = 1/2, m_i\rangle \rightarrow |5P_{3/2}, m_j = 3/2, m_i\rangle$ transition for the probe laser.

In sufficiently high B fields and large enough n the Rydberg-atom spectrum becomes "chaotic" [68]. The Rydberg spectra in strong B field can be modeled to high precision ($\lesssim 10$ MHz uncertainty) [91]. In the fully chaotic regime, highly accurate calculations, covering energy regimes both below and above the field-free ionization limit, have been performed using large Sturmian basis sets and the complex coordinate method [92]. The resultant added complexity of the spectra, combined with an ability to accurately model these spectra, will make Rydberg-EIT in high B even more sensitive to minute field variations.

4.6 Summary

We have studied vapor-cell Rydberg-EIT in a strong B field, in which ground-, intermediate- and Rydberg-states are all in the Paschen-Back regime. By exploiting the differential magnetic-field-induced shifts of the $^{85}\mathrm{Rb}$ and $^{87}\mathrm{Rb}$ EIT lines, we have measured $B = 0.6960$ T with a $\pm 0.12\%$ uncertainty. Simulated and observed spectra show excellent agreement. The spectra indicate an unusually large Rydberg-state dephasing rate, the origin of which we intend to explore in future work. Further, the large differential magnetic dipole moment of the diamagnetic Rydberg levels, which scales as B, suggests that the method holds promise for high-precision absolute and differential measurements of strong B fields. In Fig. 4.4, the maximum differential dipole moment at 0.7 T is $h \times 7$ MHz/Gauss. Assuming improved experimental conditions (laser line widths < 100 kHz, a homogeneous magnetic field, and an uncertainty of 100 kHz of the EIT line center), for this line we expect a field-measurement uncertainty of 1.5×10^{-6} T. By extending the work to larger B-fields and higher n, one may explore Rydberg-atom physics in the chaotic high-B regime in vapor cell experiments.

CHAPTER 5

Rydberg EIT Measurements in Static Electric Fields using Photoelectric Effects

5.1 Introduction

Among different working platforms of quantum technologies, ranging from ultra cold and ultra high vacuum systems to room-temperature chip scale devices, vapor-cell-based Rydberg atoms enabled technologies [93, 94, 95, 96, 97] have gained significant attention over the past few decades [98]. In these types of devices, Rydberg atoms are directly prepared from an ensemble of ground state atoms at moderate vapor pressures inside dielectric environments (borocilicate glasses or quartz) near room-temperature. These Rydberg atoms can be excited and probed either by cw multi-level electromagnetically-induced-transparency (EIT)[99, 100]or through pulsed nonlinear spectroscopy schemes such as four-wave-mixing [101, 102].

These devices demonstrate amazing isolation to environmental DC electric fields outside the cell[99, 103]. These fields are generally not known but could be very large due to random electrostatic build up. The DC field isolation is an essential prerequisite for radio frequency (RF) and microwave sensing [104, 105]. On the other hand, for applications such as Stark tuning of Rydberg transitions, the manipulation and control of electric fields inside the cell is necessary. By introducing metallic bulk electrodes [106, 107]or thin-film ITO electrodes [108] to apply fields, researchers have shown enhanced capabilities of such devices.

Inside Rydberg-atom-enabled vapor-cell devices, electric charges are ubiquitous [109, 110, 111, 112]. Volume or surface charges can exist inside or on the inner surfaces of the enclosure. These charges may originate directly from Rydberg atoms through blackbody or laser induced photoionization and collision processes (Penning ionization) [113], and can produce volume and surface charge densities through ambipolar diffusion. Due to atomic aggregate layers on the dielectric surface, free charges can also be induced by nonuniform

heating (akin to a Seebeck effect) [114] and laser illumination (photoelectric effect) [115], leading to surface charge layers. Active control of these charging mechanisms can be used to control of the electric fields inside vapor-cell devices, and improve the Rydberg atom response in specified applications.

In the following sections, I outline an experiment in which DC electric fields are produced within the dielectric enclosure without using bulk or ITO electrodes. The method presented here may enhance the functionality of the devices while still utilizing the simple structure of electrode-free dielectric vapor cells. In addition, for applications such as RF and microwave sensing where stray DC electric fields will limit the sensitivity of the device [116, 117], a detailed understanding and characterization of the DC fields inside glass-only vapor cells is necessary, especially when miniaturized devices are required. In such devices, Rydberg atoms start to interact with the device enclosures [118, 119] through surface- or space-charge-induced static electric fields, quasi-static or retarded image charge interactions, or resonant Rydberg-surface plasmon coupling [120].

By conducting this experiment, we show evidence that both Penning ionization and Seebeck-like effects can be suppressed, while at the same time a photoelectric effect can be used to produce a controllable DC electric field. We also find good agreement between the measured electric field distributions and solutions of electrostatic boundary-value problems for the utilized cell geometry.

5.2 Experimental Setups and Methods

In order to investigate the electric field distributions inside an all-glass (borosilicate in our setup) vapor cell, DC-Stark shifts are measured through EIT resonances [35] of a Rydberg state. In the Rydberg-EIT method, a fixed probe laser and a scanned coupler laser are applied to excite the atoms, as seen in Fig. 5.1. When the coupler laser is on-resonance with a Rydberg transition, the atoms in the vapor cell enter a coherent superposition state between ground and Rydberg states, leading to an observable increase in transmission (EIT) [35]. The Stark effect of the Rydberg states causes splittings and shifts of the Rydberg-EIT lines, which reveal the electric field in the cell. The Stark shifts are mapped out as a function of position along the x direction by translating the EIT channel across the vapor cell, as illustrated in Fig. 5.1.

A $9\ \mathrm{mm}$-long and $8\ \mathrm{mm}$-I.D. cylindrical glass vapor cell filled with a natural mixture of Rb vapor (part number VTC-11/9-10/8 from Rydberg Technologies Inc.), is placed inside a magnetic-field-shielding package. There are two 10 mm by 5 mm apertures in both endcaps of the enclosure, which allow us to illuminate the cell walls with a $453\text{-}\mathrm{nm}$ laser beam

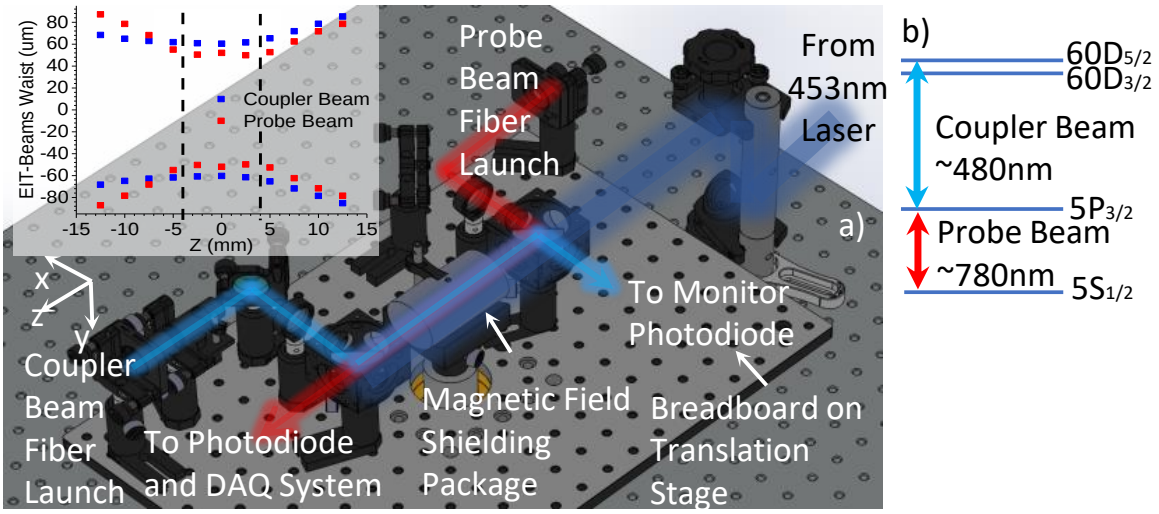

Figure 5.1: (a) Illustration of our experimental setup. A small part of the translation stage between the optical table and breadboard is seen in yellow. The insets shows measured optical beam waists ($1/e$ drop-off radii of the laser electric fields) of both probe and coupler beams. Two dashed lines indicate the positions of the vapor cell windows in the z direction. (b) Level scheme. The frequency of the probe laser (780 nm) is stabilized 27 MHz blue-detuned from the $^{87}\mathrm{Rb}$ $5S_{1/2}, F = 2$ to $5P_{3/2}, F = 3$ transition. (The exact value of the detuning is not important.) The coupler laser (480 nm) is scanned across the$5P_{3/2}, F = 3$ to $60D_J$ resonances.

and to introduce the EIT beams. The vapor cell package is fixed to the optical table with a post that goes through a cutout in an optical breadboard on which the EIT beam optics are mounted. A translation stage connecting the breadboard and optical table is used to translate the EIT probe region within the vapor cell relative to the cell walls. Both the probe and coupler beams of the EIT channel are launched from single mode polarization maintaining fibers on the breadboard. The beam sizes are chosen such that we achieve the best spatial resolution under the condition that the Rayleigh length matches the vapor cell length. Measured beam sizes are plotted in the insert of Fig. 5.1. The 453-nm photoelectric illumination beam is sent into the cell via a periscope mounted on the optical table, which allows us to adjust position of the beam relative the vapor cell. The beam size can also be adjusted via apertures (not shown in Fig. 5.1) placed before the periscope.

This setup provides an adjustable illumination configuration of the vapor cell. Further the EIT channel position can be translated relative to the cell along the x direction, while maintaining a good overlap between the EIT probe and coupler beam. However, due to some warping of the vapor cell windows, slight position mismatch between probe and coupler beams is expected. This mismatch is largest when the EIT channel is brought close

to the vapor cell windows edges, where the warping occurs. This limits the EIT probing range shown in Fig. 5.2 along x direction to about $6\ \mathrm{mm}$, which is about $3/4$ of the inner diameter of the cell.

5.3 DC Electric-field Creation and Mapping in All-glass Vapor Cell

In order to achieve a high EIT signal to noise ratio the magnetic-field-shielding package is uniformly heated to 40 °C. The cell walls are then illuminated by the 453-nm laser beams to create photoelectric charges inside the cell. The EIT resonances of the $60D$ states of $^{87}\mathrm{Rb}$ are then mapped out as function of position of the EIT probe along x direction. The Rydberg EIT resonances clearly demonstrate position-dependent DC Stark shifts. Two such DC Stark maps are shown in Fig. 5.2 (a) and 5.2 (c), corresponding to two different photoelectric illumination conditions. Somewhat surprisingly, the Stark-split lines remain quite narrow up to considerable electric field strength, indicating a simple electric field structure that is approximately homogeneous along the z direction.

In Fig. 5.2 (a), the 453-nm beam is shifted to the side of the entrance aperture, so that it illuminates only one side of the cylindrical cell wall and the illumination of the flat cell windows is negligible. In this configuration, the majority of the beam is blocked by the entrance aperture, and we estimate less that than 10 % of the total power enters through the aperture. In Fig. 5.2 (c), the 453-nm beam is centered on the aperture and the beam size is expanded to 12 mm by 12 mm before being launched from the periscope. In this case, both sides of the cylindrical cell wall are uniformly illuminated, as well as parts of the cell windows which are not blocked by the entrance apertures. In both cases, the top and bottom parts of the cell are not illuminated because of the 5-mm height of the optical-access slit in the cell enclosure.

From Fig. 5.2 and associated Stark-shift calculations which is outlined in Sec. 2.4, we find the DC electric field in the cell can be tuned between 0 and about 0.8 V/cm by varying the distance between atom-field interaction region (EIT probe volume) and the cell wall. The Stark shifts reach values up to about 300 MHz; these shifts are suitable, for instance, to tune Rydberg transitions into resonance with other fields of interest (typically, microwave or THz fields). Comparing line shift and line width of the most Stark-shifted lines, it is further seen that the DC electric field exhibits a large degree of homogeneity within the EIT probe volume; we estimate the field variation to be several percent. The spectra also indicate that the contribution to the signal from atoms close to the flat cell windows, where

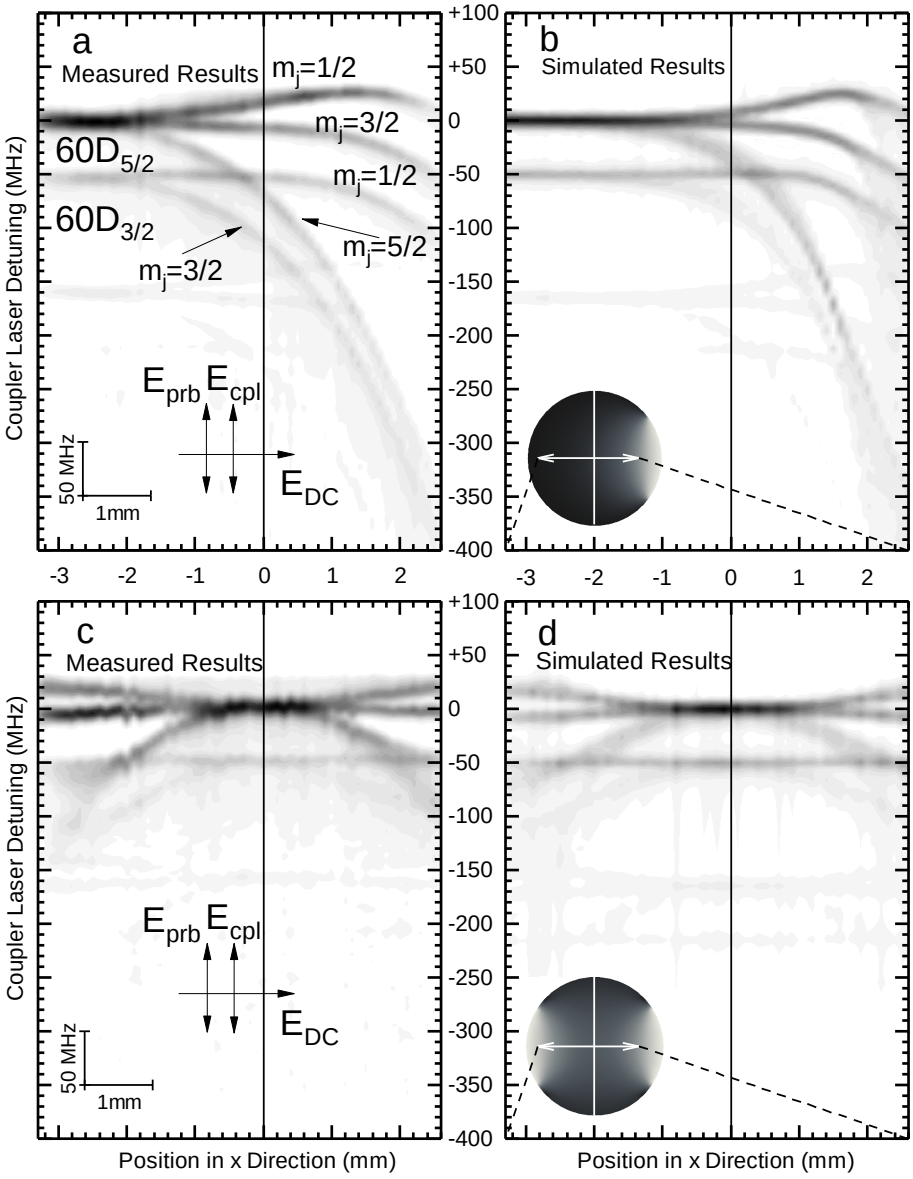

Figure 5.2: DC Stark maps of $\mathrm{Rb}\ 60D$ measured by Rydberg EIT spectroscopy for single-sided (a) and double-sided (c) illumination of the cell walls with 453-nm laser light. The probe transmission is displayed on a linear gray scale, ranging from $\sim\ 67\%$ (white) to $\sim\ 69\%$ (black). In our setup, the strongest EIT lines correspond to a reduction of the absorption coefficient by $\sim 7\%$. DC Stark shifts of $60D_{5/2}$ and $60D_{3/2}$ sub-levels give rise to the strongest signal branches. Weak EIT signals from the intermediate $5P_{3/2}$ hyperfine sub-levels $F = 2$ can also be discerned[99]. The probe- and coupler-laser polarizations and the DC electric-field direction are indicated. Panels (b) and (d) show respective simulations, with the insets showing profiles of the electrostatic potentials on a linear gray scale ranging from 0 (black) to fitted values V_0 (white). The white regions on the perimeter correspond to the illuminated segments of the cylindrical cell wall. Horizontal arrows indicate the relative position between the vapor cell and probe range achieved in this work. Poor flatness on the edges of the vapor cell windows prohibits further extension of the probe range. The vertical lines indicate the geometric center of the vapor cell in x direction.

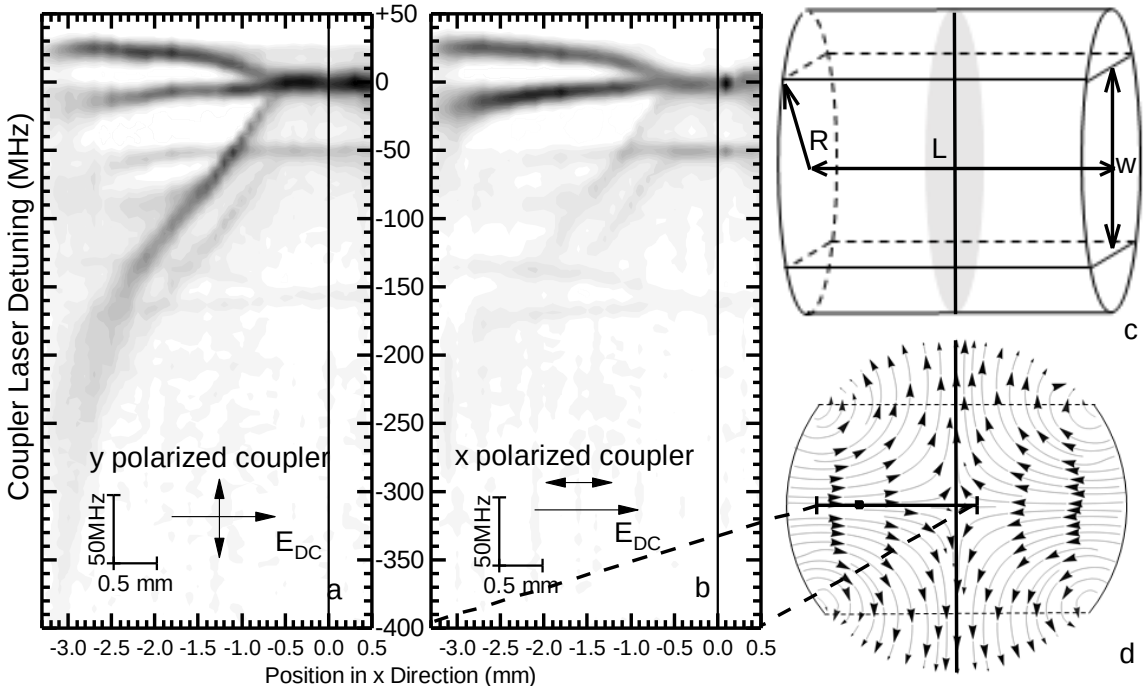

Figure 5.3: Measured DC Stark maps for the double-side illumination scenario when EIT coupler beam polarization is vertically aligned in the y direction (a) and horizontally aligned along the x direction (b). (c) Geometric model for the vapor cell used in the simulations. R is the inner radius of the cell. L is the inner cell length, and w is height of the aperture on the magnetic field shielding end caps. In our electrostatic model, the illuminated portions of the cell walls (which are sandwiched between the two horizontal planes separated by w) are assigned a boundary potential value of V_0, the only fit parameter in our model. The electric field lines on the gray cross section are plotted in (d). Vertical lines in (a), (b) and (c) indicate the symmetry axis. (d) Electric field lines on the gray cross section in (c). The horizontal solid line indicates the probe range shown in (a) and (b).

the electric field is expected to be inhomogeneous and to have a substantial z-component, is small.

5.4 DC Electric-field Model

In order to quantitatively understand the experimental data, we numerically simulate the density matrix by solving the Lindblad equation based on measured optical and geometrical parameters, similar to the procedure described in Ref.[121]. This model, similar to the one discussed in Sec.3.2.2, includes the position-dependent Rabi frequencies in the gaussian EIT beams (see inset of Fig. 5.1) and position-dependent Stark shifts of the atomic energy levels due to the non-uniform volume-distribution of the electric fields inside the cell. The absorption coefficient of the probe laser is calculated by using the position-averaged density

matrix over all three dimensions. The simulated EIT probe beam absorption signals, shown in Figs. 5.2 (b) and 5.2 (d) for both illumination scenarios, are then obtained from Beer's absorption law. The only unknown in this model is the electric-field distribution.

In order to find the electric-field distributions inside the glass cell, the electric potential is calculated by solving the Laplace equation numerically with Dirichlet boundary conditions on the inner surfaces of the cell walls. These boundary conditions simulate the steady state of the photoelectric processes inside the vapor cell. We assign a fixed nonzero potential V_0 to the area that is illuminated by the 453-nm laser, whereas the dark regions of the cell walls are set to zero potential. We also assume that there are no free space charges inside the cell. A sketch of the model for the simulations in Fig. 5.2 (d) is depicted in Fig. 5.2 (c) ($V_0 = 0.15$ V). In our model, V_0 is the only free parameter used fit the experimental data.

A second way of obtaining the potential is to perform a series expansion of the potential in a volume-charge-free cylindrical volume with end-caps [122]. The result for single sided illumination, used in Fig. 5.2 (b), is shown in Eq. 5.1; the best fit value for the surface potential is $V_0 = 0.33$ V in this case. We use numerical solutions of the Laplace equation and series expansions interchangeably; the results of both methods have been cross-checked for consistency.

From the calculated three-dimensional electric-field distributions and the known Stark-shift behavior of the utilized Rydberg levels, we obtain models for the EIT spectra as described near the end of Section 5.3. The spectra are integrated along the z-direction, from the entrance to exit window of the cell. Calculated EIT spectra are shown in Figs. 5.2 (b) and 5.2 (d).

$$\begin{aligned} V(\rho,\phi,z) =& \sum_{m=1}^{\infty}\sum_{n=odd}^{\infty} \frac{8V_0}{mn\pi^2}\frac{I_m(n\pi\rho/L)}{I_m(n\pi R/L)}\sin\left[m\tan^{-1}\left(\frac{w}{2R}\right)\right]\sin\left(n\pi\frac{z}{L}\right)\cos(m\phi) \\ &+ \sum_{n=odd}^{\infty}\frac{4V_0\tan^{-1}[w/(2R)]}{n\pi^2}\frac{I_0(n\pi\rho/L)}{I_0(n\pi R/L)}\sin\left(n\pi\frac{z}{L}\right) \end{aligned} \tag{5.1}$$

We find that the electric fields are relatively uniform in magnitude and direction within the EIT probe region, for both scenarios shown in Figs. 5.2 (a) and 5.2 (c). The electric-field lines on the shaded cross section in Fig. 5.3 (c) are plotted in Fig. 5.3 (d) for the case of double-sided illumination. In this case, the electric field exhibits quadrupolar characteristics.

The direction of the DC electric field is verified by changing the polarization direction

of the coupler beam from perpendicular (as shown in Fig. 5.3 (a)) to parallel (Fig. 5.3 (b)) relative to the DC electric field. In the perpendicular case, the coupler laser effects a mix of left- and right-circularly-polarized Rydberg-atom excitation with respect to the x quantization axis (direction of DC electric fields). This leads to a much stronger $m_j = 5/2$ component in the EIT spectrum in Fig. 5.3 (a) than in Fig. 5.3 (b).

5.5 Discussion

Using only one unknown parameter V_0, our model describes the electric-field distributions inside the cell relatively well. The electric potential generated by the photoelectric processes on the surfaces of a material is generally related to the energy difference between the photon energy (here, 2.74 eV corresponding to 453 nm) and the work function of the surface. In this work, surface potentials in the range of a few hundred mV fit the experimental results best. Due to the complex composition of the glass materials and thin Rb atomic layers (aggregates) deposited on the inner surface of the glass cell, precise determination of the work function and charge affinity of such surfaces is nontrivial (see reference [123] and citations therein). Further, several other (surface / free-space) charge generation mechanisms can also play a role in vapor cell Rydberg-EIT experiments, such as Penning ionization of Rydberg states, Seebeck effects , etc.

In Fig. 5.4, the rms electric field within the EIT probing region is measured as a function of intensity of the 453-nm beam. Fig. 5.4 shows that over the investigated intensity range, the rms electric field varies only moderately. This behavior is seen for all displacements of the EIT probing region along x.

The other well known charge generation mechanism are Penning ionization and blackbody ionization of Rydberg atoms. These processes can be adjusted by varying the power of the EIT beams. We do not observe significant changes in the DC electric field strength in the cell. (The power of both probe and coupler beams are nevertheless kept as low as possible in this work in order to achieve low power broadening and hence better spectral resolution.) These observations motivate us not to include spatial charges in our model. The results also suggest that the photoelectric effect on the cell walls is the only major source of the charges in the present work.

We have observed a decrease in electric field strength when a second 780-nm beam is introduced into the system and overlapped with the 453-nm beam as shown in Fig. 5.5. The second 780-nm beam is tuned close to resonance with the $^{85}\mathrm{Rb}$ D2-line, so that it does not interfere with our $^{87}\mathrm{Rb}$ EIT probe setup. We believe that the additional charges generated by photoionization of $^{85}\mathrm{Rb}$ diffuse to the call walls and (partially) neutralize the electric

field caused by the photoelectric effect on the cell wall. The details of this mechanism need further investigation.

In Fig. 5.2, it is seen that the calculated electric fields decay somewhat faster as a function of distance from the cell walls than the measured ones. This behavior has been observed for all photoelectric illumination conditions tested, and for several different cell temperatures. This faster decay is not a result of underestimating the parameter V_0, and it cannot be explained by taking an average of the field over the EIT probing region. We relate this deviation between calculation and measurement to three possible causes. First, the geometric accuracy of our model is limited. For example, the small filling stem on the cylindrical vapor cell is not included. Second, the illuminated surface area on the cell wall may be underestimated. In the model, this area is set to the aperture size of the magnetic-field shielding package. However, diffraction and scattering of 453-nm-light may lead to an increase of the actually illuminated area on the cell wall. Third, non-negligible free spatial charges generated by the EIT probing beams may (partially) neutralize the field near the center of the cell.

5.6 Summary

We have investigated DC electric fields generated by the photoelectric process on the inner surfaces of a glass vapor cell by introducing a 453-nm beam. The field distributions are mapped out using Rydberg-EIT spectroscopy. Although detailed characterization of the photoelectric effects on the cell inner surface is non-trivial, we have developed a simple phenomenological model that has reproduced the measured electric fields quite well.

The ability to understand and manipulate local electromagnetic fields is critical for developing miniaturized vapor cell based devices. The characterization of spurious photoelectric effects on the cell walls is important to avoid stray electric fields inside the cell. On the other hand, the effect described in this paper can also be used to Stark-tune Rydberg transitions in vapor cells without the use of electrodes inside the cell. This functionality would allow to frequency-tune Rydberg-atom-based detectors and receivers using a laser for electric-field and Stark shift control. In future work, one may also study the electric-field response time to changes in illumination conditions.

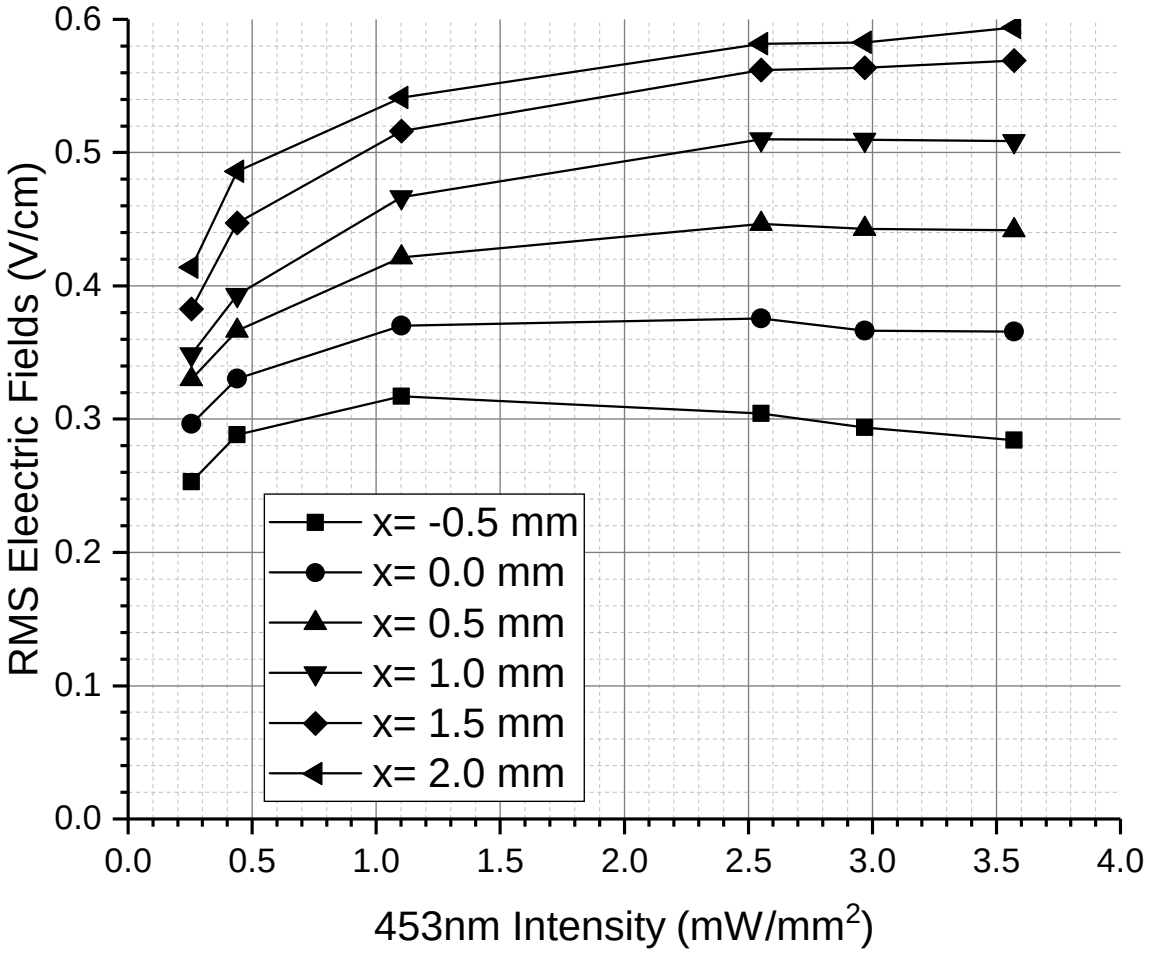

Figure 5.4: Measured rms values of the electric field averaged over the EIT field-probing region as a function of estimated intensity of the 453 nm photoelectric excitation beam, for single-sided illumination as in Fig 2 (a). In this configuration, we estimate that less than 10% of the total power of the 453-nm light entered into the magnetic-shielding package. The majority of the beam is blocked at the entrance aperture of the magnetic-shielding package. Different symbols represent different EIT probe positions along x direction. The electric fields is obtained by matching measured and calculated Stark shifts of the peaks in the EIT spectra. We attribute the slight decrease at high powers, seen for $x \sim 0$, to comparable line-width of EIT transmission peak and DC Stark shifts. To guide the eyes, the data points are connected by lines.

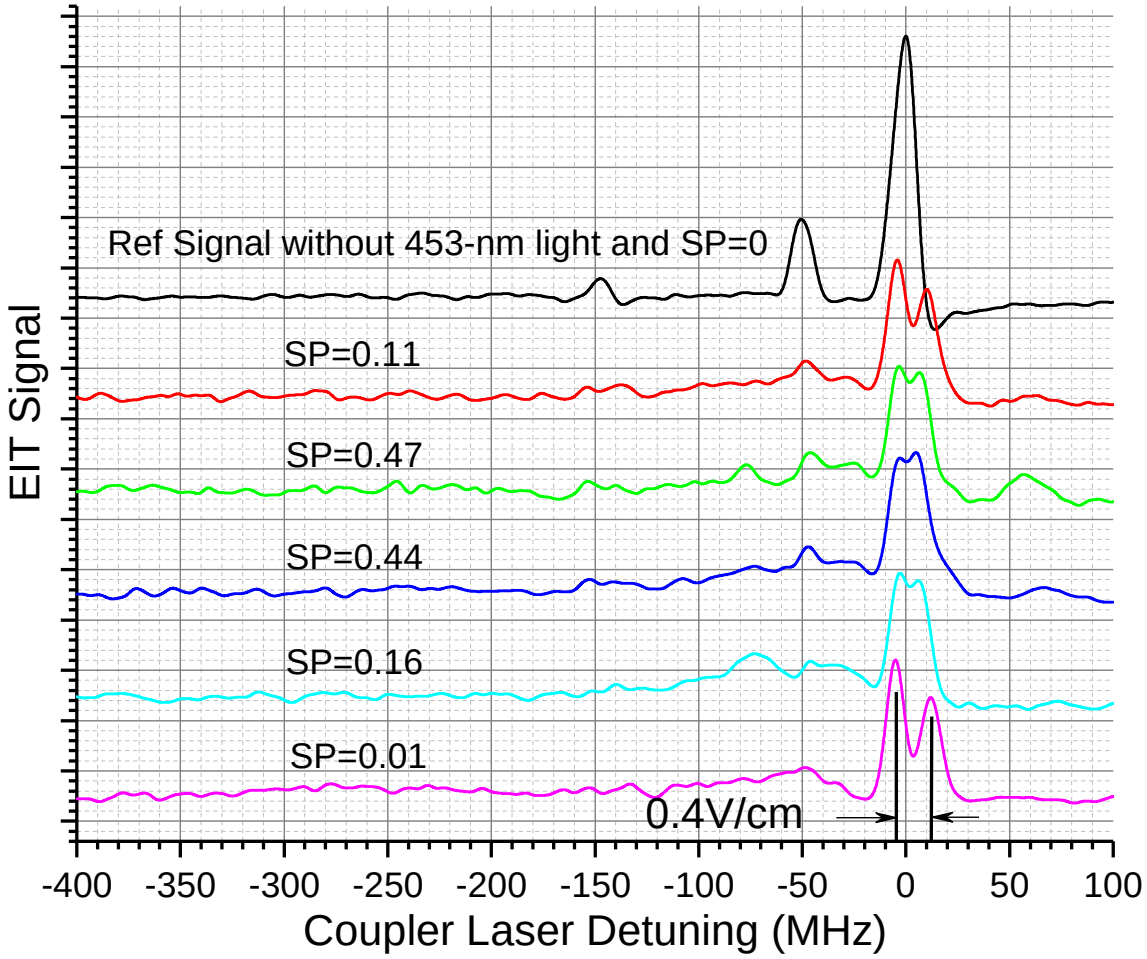

Figure 5.5: EIT probe traces for different saturation parameters (SP) of a second 780-nm laser introduced into the system. The saturation parameters (SP) are indicated in the legend. An EIT trace for zero electric field is shown for reference (black line). The second 780-nm laser has a fixed power of 5.6 mW, a diameter of about 1 mm, and it is overlapped with the 453-nm beam, which also illuminates the cell walls. The saturation parameter is varied via the detuning of the second 780-nm laser, by changing the frequency of this laser from the red side to the blue side of the $^{85}\mathrm{Rb}5S_{1/2}, F = 3 \rightarrow 5P_{3/2}, F = 4$ transition. The power of the EIT beams are fixed. The splitting of the $D = 5/2$ line, indicated by the black vertical lines, is due to the Stark splitting of the $m = 3/2$ and $m = 5/2$ magnetic sub-levels. This Stark splitting corresponds to about 0.4 V/cm.

CHAPTER 6

Interaction Time & Cell-Wall Collision Effects Investigation using Ground State Atoms

6.1 Introduction

The laser induced atomic coherence can be fragile, as it is affected by various decoherence processes, including optical pumping, collision or diffusion, and power broadening. For applications such as atomic frequency standards and precision magnetometers that utilize vapor cells, atomic coherences arising from Coherent Population Trapping (CPT) have been reported in detail in terms of line width and line shape [124, 125, 126]. In these systems, collisions between the probed atoms and buffer gas atoms in the vapor cell contribute significantly to the homogenous line width. Depending on the buffer gas pressure and collision conditions, this broadening can be larger than the Doppler width [127, 128], yet the CPT resonances remain very narrow. Under such circumstances, the CPT line shape and width are determined by atom diffusion and local light intensity [129, 130, 124].

EIT experiments in thermal vapor cells without buffer gas [13, 131, 132, 22, 133, 134, 135, 136, 137] also have received considerable attention, as Ref. [135] points out that the EIT resonance is a unique product of the light-atom coherences that can be experimentally measured and can provide us an opportunity to better understand the influence of different decoherence processes.

In this chapter, instead of performing EIT experiments on a Rydberg state, we chose two ground states of the Rb atoms to form the dark state. We perform the EIT measurements for a Λ-type system on the $^{85}\mathrm{Rb}$ D2 transition in a buffer-gas-free vapor cell without anti-relaxation coating. An illustration of the experimental setup can be found in Figure 6.1(a).

For our study of the EIT line width, we select a resonance with zero first-order Zeeman shift and eliminate inhomogeneous line broadening and pulling effects by lifting the Zeeman degeneracy with an in-situ calibrated spatially homogeneous magnetic field. We demonstrate that the width of the magnetic-field-insensitive EIT line varies linearly as a

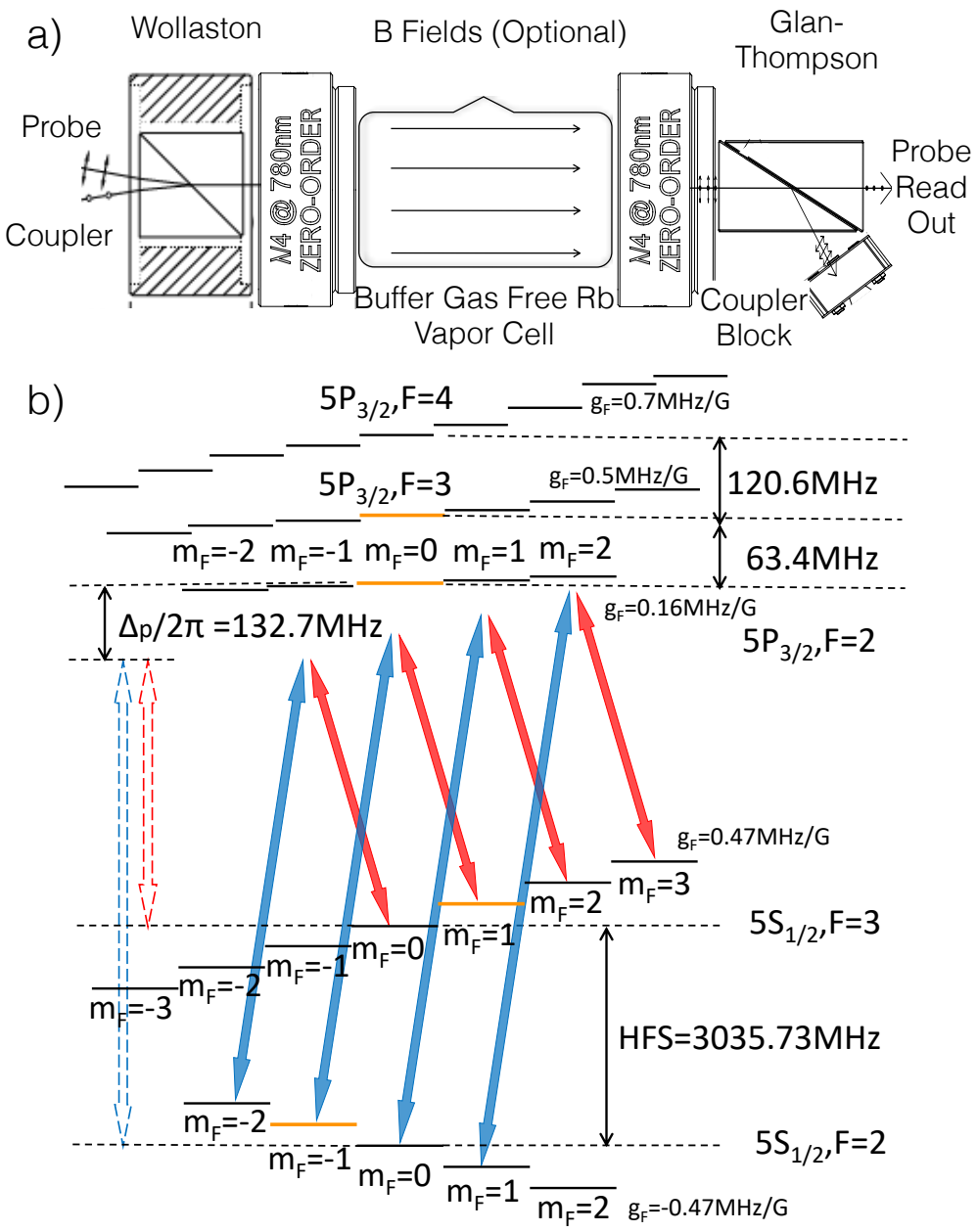

Figure 6.1: (a) Illustration of the experimental setup featuring co-propagating coupling and probe beams in σ^+-σ^- polarization configuration passing through a Rb vapor cell of 25 mm in diameter and 70 mm in length. A variable uniform magnetic field can by applied via a solenoid with inner diameter 33 mm, outer diameter 44 mm, and length 190 mm (not shown). The spectroscopy cell is gently warmed up to 30°C in the experiment. (b) Zeeman level diagram of relevant states and transitions in the given polarization configuration in a magnetic field for the EIT study. The blue and red arrows correspond to transitions driven by the coupling and probe lasers. The scheme breaks up into four Λ systems that correspond to individual, Zeeman-shifted EIT lines. The Λ system with zero first order Zeeman shift has been highlighted with orange energy-level bars.

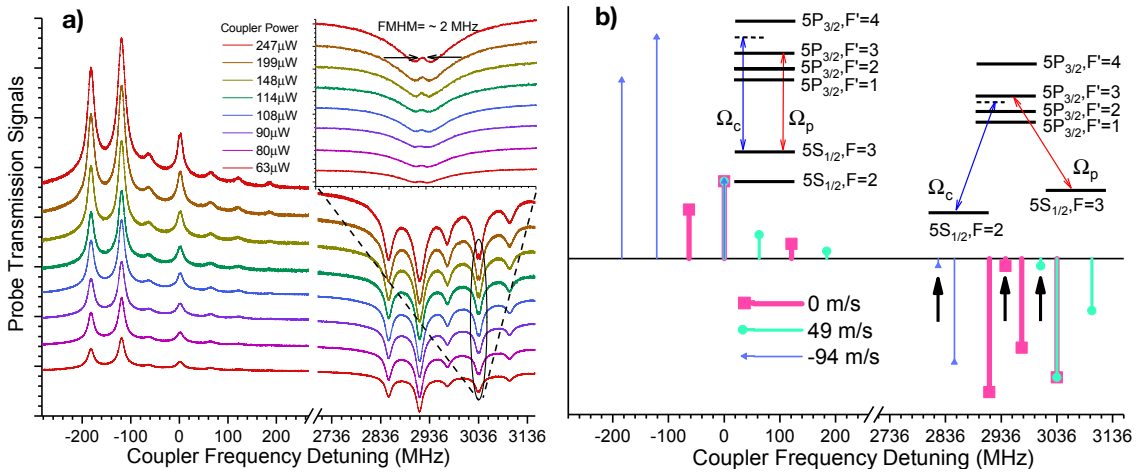

Figure 6.2: (a) Series of probe transmission spectra with different coupling laser power vs coupling laser frequency detuning for fixed probe laser power (70 μW) and fixed probe frequency tuned to the transition $|5S_{1/2}, F = 3\rangle \longrightarrow |5P_{3/2}, F' = 3\rangle$. The insert shows a zoomed-in view on the EIT peak. (b) Analysis of the observed lines by atom velocity groups resonant with probe and coupling lasers. Red lines with square symbols correspond to atoms with zero velocity, green lines with circle symbols correspond to atoms with 49 m/s velocity; and blue lines with triangle symbols represent atoms with -94 m/s velocity.

function of the coupling-laser Rabi frequency. Our results confirm the theoretical prediction outlined in Ref. [138, 139, 140] for a Doppler broadened sample. Further, a numerical simulation in which we include the laser intensity profile shows improved fitting to our data. This aspect is not fully accounted for in previous theoretical [138, 139, 140] and experimental [134, 135, 141] work. In the limit of vanishing laser power, our measurements indicate that the EIT signal decreases exponentially as a function of detuning from the line center. This special behavior was theoretically predicted [142] for room-temperature atoms moving in Gaussian optical beams.

6.2 Velocity-selective Optical Pumping and EIT

We first demonstrate the reduced (saturated) and enhanced absorption lines caused by velocity-selective optical pumping on the ground- and excited-state hyperfine structure, as well as the location of the EIT resonance within the overall spectrum.

Velocity-selective effects occur in vapor cells because of the Doppler shift $\delta\omega = \boldsymbol{k} \cdot \boldsymbol{v}$, where $\boldsymbol{k}$ and $\boldsymbol{v}$ are optical wavenumber and atom velocity [143]. It gives rise to velocity dependent "hole burning" (increased transmission peaks) and "optical pumping" (reduced transmission dips) effects demonstrated in the probe transmission spectra in Figure 6.2(a).

Table 6.1: Assignment table for the spectral features observed in Figure 6.2. The probe laser is fixed at the (zero-velocity) $|5S_{1/2}, F = 3\rangle \longrightarrow |5P_{3/2}, F' = 3\rangle$ transition frequency. Left column: Resonant velocity groups for the indicated probe-laser transitions with lower- and upper-state hyperfine quantum numbers $[F_p, F']$. Center block: Coupling-laser detunings of the enhanced-transmission peaks relative to the probe laser for the indicated coupling-laser transitions, with lower- and upper-state hyperfine quantum numbers $F_c = 3$ and F' and for the velocities shown in the left column. Right block: Coupling-laser detunings of the reduced-transmission peaks relative to the probe laser for the indicated coupling-laser transitions, with lower- and upper-state hyperfine quantum numbers $F_c = 2$ and F' and for the velocities shown in the left column.

Probe Transition	Coupling Transition Detuning (MHz)					
Velocity Group	From $\|F_c = 3\rangle$ to			From $\|F_c = 2\rangle$ to		
(m/s) $[F_p, F']$	$\|F' = 2\rangle$	$\|F' = 3\rangle$	$\|F' = 4\rangle$	$\|F' = 1\rangle$	$\|F' = 2\rangle$	$\|F' = 3\rangle$
49 [3, 2]	0	63	184	3007	3036[a]	3009
0 [3, 3]	-63	0	121	2944	2973	3036[a]
-94 [3, 4]	-184	-121	0	2823	2852	2915

[a] EIT Resonance

Both processes are highly velocity-selective due to the fact that the upper-state ($|5P_{3/2}\rangle$) scattering rate scales as $s/[1 + s + 4(\Delta/\Gamma)^2]$, where s is the saturation parameter defined as the ratio between laser and saturation intensity, Δ is the velocity-dependent optical detuning in rad/s, and Γ is the natural decay rate, which is $2\pi \times 6$ MHz for Rb $5P_{3/2}$. Hence, at low saturation (our case) the velocity bandwidth of the D2 transition in a vapor cell is about 5 m/s. Figure 6.2 (b) and Table 6.2 relate the observed spectral lines to atomic transitions and resonant velocities. The line strengths vary due to the variation of transition dipole matrix elements between the hyperfine states, and because the resonances cover three velocity groups (with different values of the Maxwell probability distribution). Three resonances, indicated by the bold black arrows in Figure 6.2(b), are too weak to become visible in Figure 6.2(a). The line-strength ratios agree with a quantum Monte Carlo simulation [90, 144, 145], in which we have included all magnetic sub-levels of the system. The ratios are not a main topic in the present paper but may be discussed in future work.

The insert of Figure 6.2(a) shows the emergence of an EIT resonance on the optical-pumping dip centered at the hyperfine splitting 3036 MHz. The EIT results from quantum interference on two Raman-degenerate Λ systems involving the excitation pathways $|5S_{1/2}, F = 3\rangle \leftrightarrow |5P_{3/2}, F'\rangle$, driven by the probe laser, and $|5S_{1/2}, F = 2\rangle \leftrightarrow |5P_{3/2}, F'\rangle$, driven by the coupling laser, where $F' = 2$ or 3. These couplings are velocity-selective in the Doppler-broadened medium; here, the respective resonant velocities are 0 and 49 m/s.

The velocity difference is the smallest among Λ-EIT cases on the ^{85}Rb and ^{87}Rb D1 and D2 lines, and it is smaller than the thermal atom velocity in the cell. We find in Section 4 that EIT on the ^{85}Rb D2 line is affected by both Λ-EIT systems.

6.3 Zeeman Shifts of EIT Lines Excited by Phase Locked Lasers

The line width of the EIT peak in Figure 6.2(a) is about 2 MHz. Power broadening, relative laser frequency jitters and Zeeman shifts of the involved magnetic sub-levels due to stray magnetic fields are the dominant contributors to the line width. In the following experiments we have mitigated the last two broadening mechanisms by implementation of an Optical Phase Lock Loop (OPLL), and by application of a calibrated, longitudinal magnetic field that lifts the Zeeman degeneracies, allowing us to selectively study a magnetic-field-insensitive EIT resonance.

6.3.1 Optical Phase Lock Loop

Atomic decoherence caused by laser frequency jitter [146, 147] is significantly improved by an OPLL [148]. In this section, I will describe and document the OPLL we built in order to reduced the relative frequency and phase jitter between the coupling laser and probe laser. I will refer to the coupler laser as the follower laser, where the frequency follows the frequency of the probe laser (in this case, the master laser) with an offset frequency provided by an RF synthesizer. A schematic diagram of the OPLL system is shown in Fig. 6.3. The key element in this system is the digital phase frequency detector (PFD) which detects and compares the frequency and phase of the inputs. An ultra low noise PFD (HMC3176LP4E from Analog Devices) are needed for this type of application. A114413 evaluation board from Analog Devices is used to carry the supporting digital RF circuitry for this PFD.

The functionality of the PFD HMC3176LP4E can be described as it compares the rising edge of the two input signals (REF and VCO). This information is then used to pulse the outputs signals (ND and NU). Depending on which inputs frequency is larger, one of the outputs remains idle (approximately at 5V constant) and the other output is active (output vary on average between 3 to 5 V). This device demonstrates the best noise performance when Digital inputs (TTL) are used. It still functions if analog inputs signals are presented. The outputs behavior allows us to derive a sign switching signal when the two outputs are

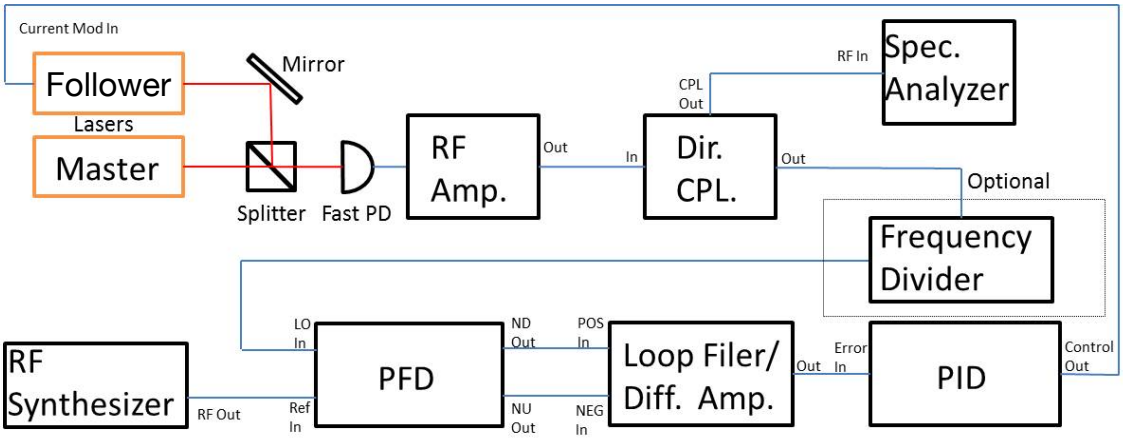

Figure 6.3: OPLL diagram used in this experiment. Two external cavity diode lasers (Follower and Master) light are heterodyne detected using a fast photodetector (Fast PD). The beat note signal is then amplified by a RF amplifier (RF Amp.) and fed into a digital phase frequency detector (PFD). The output of the PDF are further processed by a difference amplifier (Diff. Amp) also known as a loop filter which generate the error signal used in a large bandwidth PID controller. In the lock condition, the frequency difference of the two laser are locked to the RF Synthesizer output frequency and are phase of the beat note signal are held at constant relative to the RF synthesizer output.

processed by a difference amplifier (loop filter). The sign switching signal can be used as an error signal input of a fast PID (Toptica FALC 10MHz bandwidth).

Fig. 6.4 summarize the outputs (ND and NU) behavior of the PFD. In Fig. 6.4(a), the master laser frequency is fixed and follower laser frequency is scanned using the external cavity grating. This results in a frequency sweep of the beat note signal detected by a fast GaAs Metal-Semiconductor-Metal(MSM) fast photodiode (Hamamatsu G4176-03). The RF synthesizer output frequency is held at fixed 330 MHz. When the beat note signal frequency swept through the synthesizer frequency, the difference of the ND and NU demonstrate a sharp sign switch (Lock points). This feature enable us to tightly lock the frequency difference between the two lasers.

Fig. 6.4(b) shows the detailed behaviors of the ND and NU output when the signal frequencies of the two inputs (REF and VCO) are close to each other (They are forced at a difference of 11 Hz). In this case, ND output is idle at about 5 V constant and NU is active and changing linearly and reset at a frequency of exact 11 Hz. This provides some hints about how this device can be used to detect the phase difference between the REF and VCO. In the limit that the periodic oscillations of the two inputs (REF and VCO) have exactly the same frequency but only differ by a small amount in phase, the NU signal will be linearly proportional to the accumulated phase differences. Therefore, in a lock condition, the sign

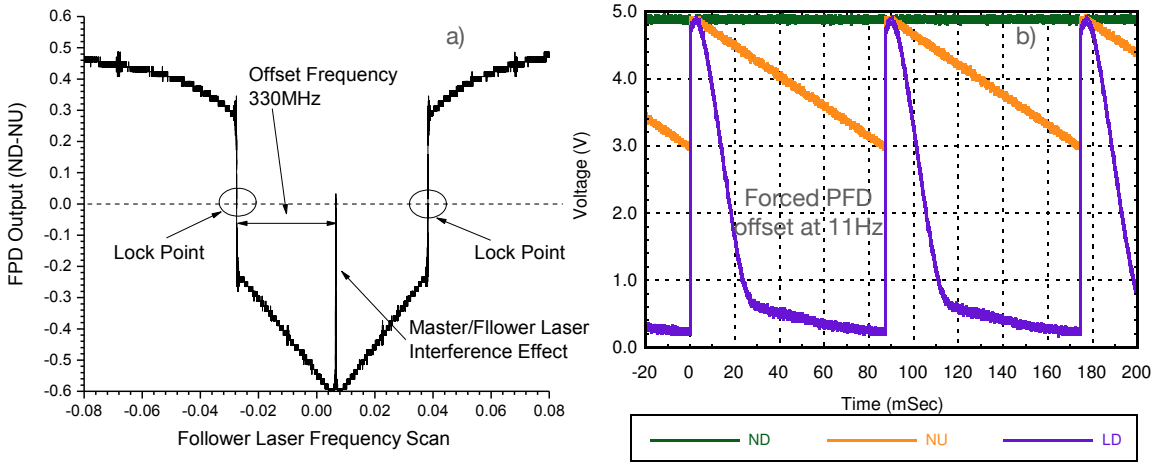

Figure 6.4: The outputs (ND and NU) behavior of the PFD HMC3176LP4E when (a) one of the inputs (REF and VCO) frequency is sweeping and (b) both of the inputs frequencies are held at fix with a small difference. In (a), a sharp sign switching signal is visible when the inputs (ND and NU) frequency differs at a large amount. This feature are used to tightly lock the frequency of the two lasers. The middle peak is an artifact when the follower frequency is swept right across the master laser frequency. This signal can be used as an error signal to lock the two laser frequencies with a preset frequency difference at the lock point. In (b), the blue LD signals can be used to control a LED to indicate the lock status. This function is not implemented in this setup so far.

of the ND$-$NU tells us which input frequency is larger(or smaller) and the magnitude tells us the phase difference.

When the two lasers are phase locked with frequency difference set by the RF synthesizer, the residual phase noise of the two laser beam can be calculated by measuring the frequency spectrum of the beat note signal [149]. This is done by using the directional coupler (Dir. Cpl.) and a spectrum analyzer shown in Fig. 6.3. A typical spectrum is shown in Fig. 6.5 where the offset frequency is adjust close to the ^{85}Rb ground state hyperfine splitting. A FWHM frequency width of less than 3 Hz is achieved. Using the data shown in Fig. 6.5 and Weiner-Khintchine Theorem we conclude that a residual phase uncertainty $\sigma_{\phi_{rms}}$ is less than 0.3 rad. This result is comparable to Ref. [148], where similar locking electronics is used.

6.3.2 First and second order Zeeman shifts

The EIT line broadening caused by stray magnetic fields [150] is alleviated by applying a comparably large, homogeneous magnetic field which removes degeneracies between the magnetic sub-levels. The Zeeman level diagram is shown in Figure 6.1(b). In

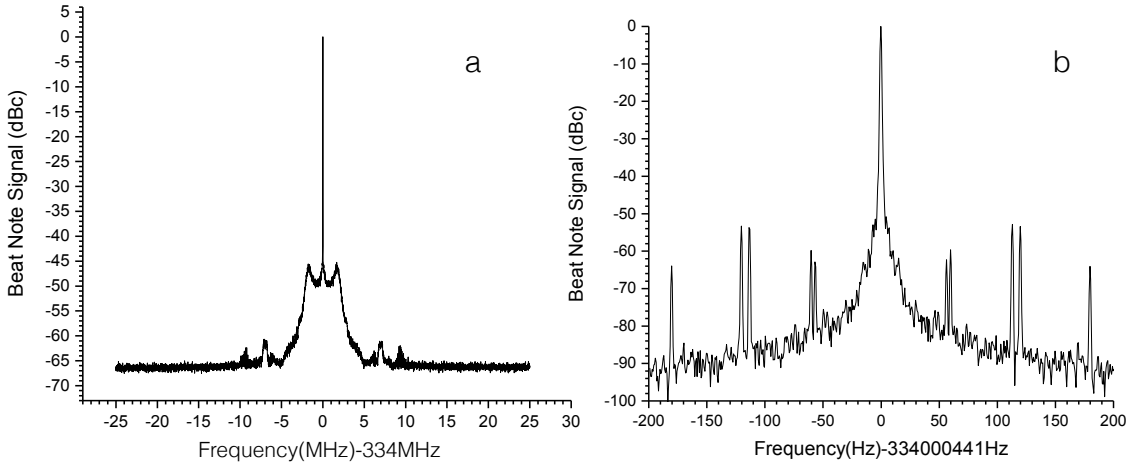

Figure 6.5: Frequency spectrum of the beat note signal of two phase locked lasers at a fixed offset frequency of 334MHz with (a) a large frequency window and (b) a smaller frequency window zoomed on to the center peak in (a). In (b), power line noise at 60Hz and its harmonics are also visible. The source of a mysterious noise signal at 56.5Hz and its harmonics are unknown.

Figure 6.6(a) we present the Zeeman shifts of the EIT signals. For the laser polarizations in our experiment, the first-order Zeeman shifts are $\hbar\delta_{Zeeman} = \mu_B B\left(-\frac{2}{3} + \frac{2}{3}m_F\right)$, where μ_B is the Bohr magneton, B is the magnetic field, and m_F is the magnetic quantum number of the state $|5S_{1/2}, F = 3, m_F\rangle$. The three magnetic-field-sensitive EIT resonances ($m_F = \{0, 2, 3\}$) allow an in-situ calibration of B, against the coil current, I. The calibration factors for the field and the EIT line splittings are 61.7 ± 0.8Gauss/A and 57.6 ± 0.7 MHz/A, respectively. The uncertainty is obtained through a linear fitting procedure, which results in an R^2 value of 0.99993. In currents (fields) below $\sim$ 10 mA (0.6 Gauss), the effects of transverse stray magnetic fields (circled region in Figure 6.6(a)) become obvious.

The first order Zeeman shift vanishes for the EIT resonance involving the states $|5S_{1/2}, F = 2, m_F = -1\rangle$ and $|5S_{1/2}, F = 3, m_F = 1\rangle$. The minuscule shift of this EIT line due the second order Zeeman effect is plotted as red dots in Figure 6.6(b). The black line is the expected second order Zeeman shift obtained through a direct diagonalization of the Hamiltonian including all magnetic sub-levels in both ground and excited states. At fields $B \gtrsim 3$ Gauss the EIT resonances become well-separated, and the magnetic-field-insensitive resonance becomes insensitive to line pulling and broadening effects. For the remainder of the paper, we choose a longitudinal field of $B = 6$ Gauss. At this field strength, field variations due to the finite length of the solenoid and transverse stray fields are less than 1%. The resultant variation of the second-order Zeeman shift causes inhomo-

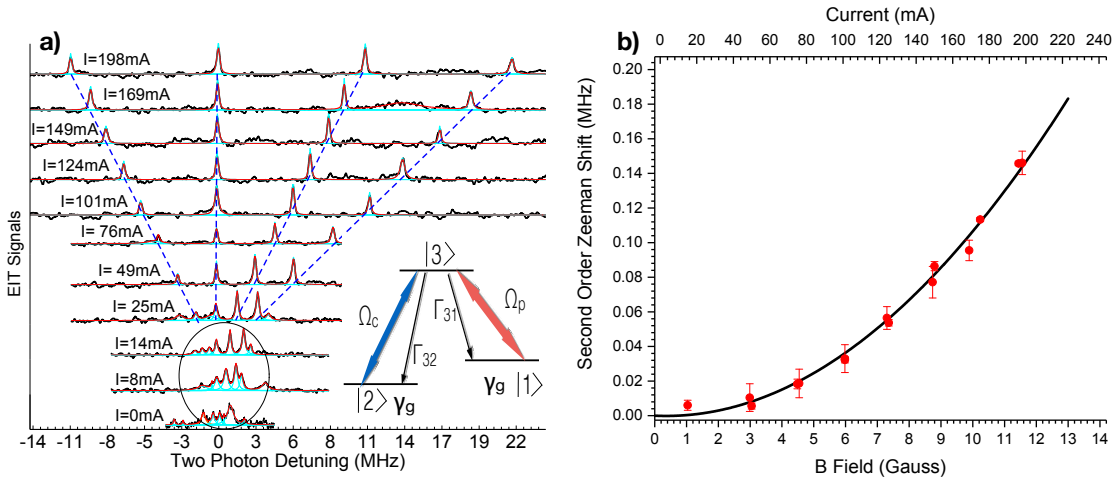

Figure 6.6: (a) Series of Zeeman-split EIT spectra (black lines) for different magnetic-coil currents. Fittings of individual peaks (Cyan lines) and entire traces (red lines) are shown to guide the eye. The spectra are dominated by four Zeeman-split EIT lines, each of which corresponds with an isolated Λ system (see insert). First-order Zeeman shifts (blue dashed lines) can be utilized to perform an in-situ calibration of the magnetic field vs current. In currents less than $\sim$ 25 mA the spectra are affected by stray magnetic fields (circled region); this region is excluded from the field-calibration fit. (b) Measured (red dots) and theoretical (black line) second-order Zeeman shifts of the EIT resonance involving the $|5S_{1/2}, F = 2, m_F = -1\rangle$ and $|5S_{1/2}, F = 3, m_F = 1\rangle$ ground states.

geneous line broadening of $\lesssim 1.5$ kHz for the magnetic-field-insensitive EIT line.

6.4 Doppler Narrowing and Beam Shape effects on EIT linewidth

Taking advantage of the experimental techniques mentioned above, we are able to gain further insight into the ground-state decoherence in a Λ system by studying the line width of the magnetic-field-insensitive EIT resonance. In the limit of zero Rabi frequency, the line width is limited by collision [128, 127, 53] and transit-time effects [142], in addition to technical noise such as residual relative phase fluctuations of the lasers [128] and stray magnetic fields caused by the coil current noises. For experiments using buffer-gas-free room-temperature vapor cells, collisions between Rb atoms and other trace gas atoms are less important. Therefore, power broadening, transverse laser intensity distribution, and transit-time effects of the thermal atoms become the major factors, as we demonstrate in the following. In addition, wall collisions are still present which deplete ground-state coherence [151].

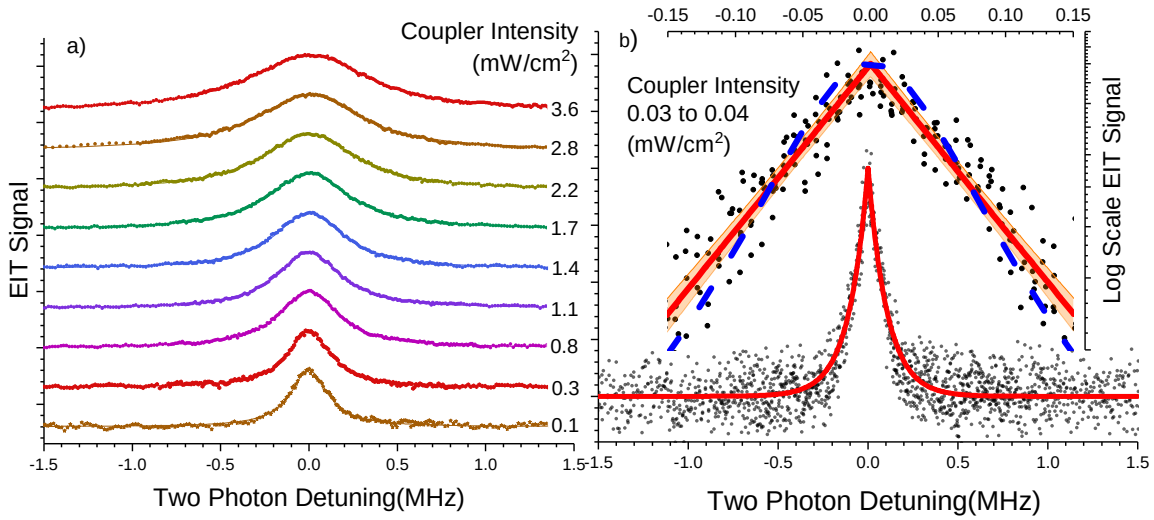

Figure 6.7: (a) EIT resonances for the indicated coupling-laser intensities at the beam center. Experimental data, shown as dots, are fit very well by Lorentzians (solid curves). (b) EIT line shape in the limit of very small coupling laser intensity. Several data sets for intensities ranging from 0.03 to 0.04 mW/cm^2 are overlapped (black dots) in order to improve statistics. The red solid curve represents a symmetric exponential-decay fit on both sides of the resonance. A log-scale representation of data and fits are shown as an insert. The region shaded in orange represents the range of fit results for a 99.5%-confidence range. A Lorentzian fit (blue dashed curve), plotted for comparison, clearly is less good.

Figure 6.7(a) shows a series of spectra of the magnetic-field-insensitive EIT resonance vs coupling-laser intensity at $B = 6$ Gauss. At higher intensities power broadening dominates, and the EIT lines have a Lorentzian shape (as opposed to Gaussian or symmetric exponential). As the intensity drops below ~ 0.1 mW/cm^2, the line width drops dramatically, and the line shape deviates from a Lorentzian profile. Figure 6.7(b) shows spectra with intensities between 0.03 and 0.04 mW/cm^2. These low-intensity signals show an exponential decay on both sides of the resonance. This special behavior has been predicted theoretically in Ref. [142] as a consequence of thermal atoms traveling through Gaussian optical beams. Due to limited signal to noise ratio, we are not able to resolve the exact second derivative at the line center. It needs to be pointed out that this transit-time effect is fundamentally different from CPT line shapes observed in buffer-gas-enriched vapor cells. In the latter case, the diffusion [129, 130] of the alkali atoms among the buffer gas atoms and the local intensity [124] of the driving laser beams play dominant roles.

In Figure 6.8, we plot the measured FWHM (black dots) as a function of the coupling laser power and compare to various analytic and numeric models. We note first that the measured line width is much lower than an opacity/density adjusted result [152, 35] (blue and purple dashed lines) for a homogeneously broadened sample, such as cold atoms or

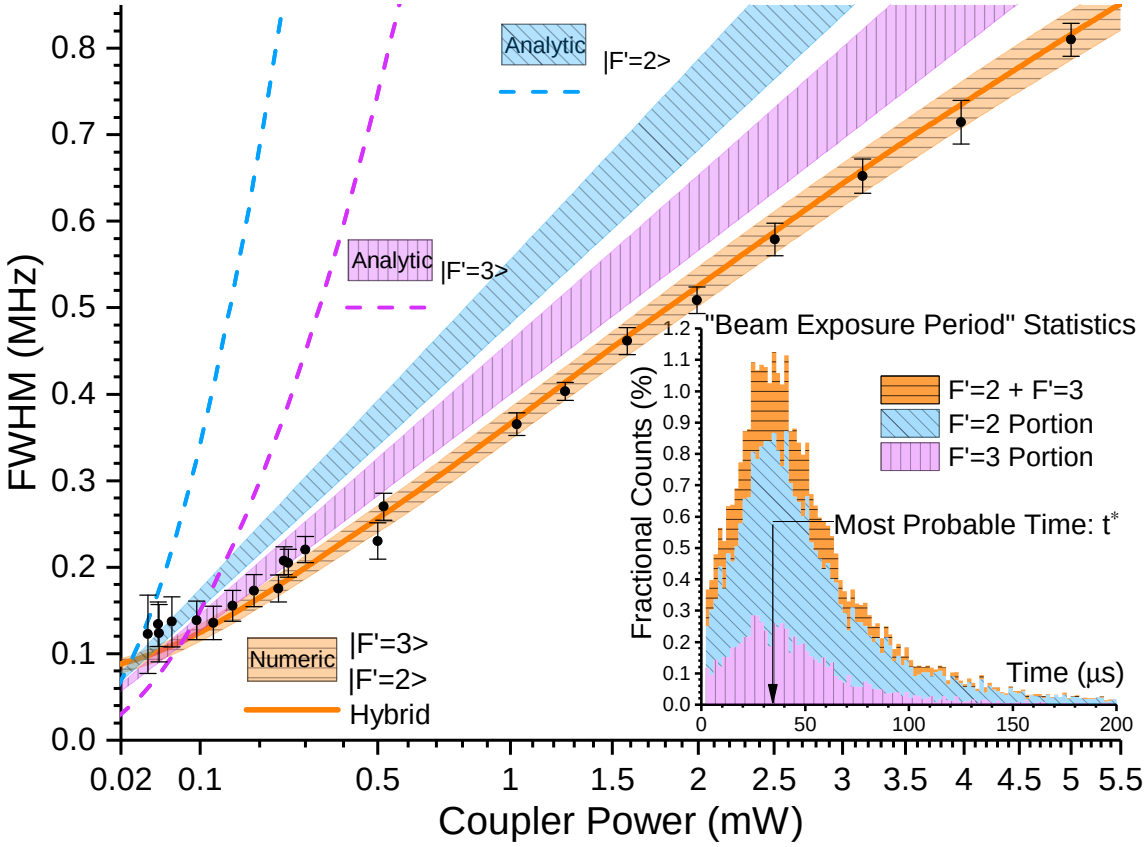

Figure 6.8: Full widths at half maximum (FWHM) of EIT lines (black dots) as a function of coupling laser power. The length along the x-axis is linear in square-root of power. Blue and purple dashed lines represent results for stationary atoms. The blue and purple hatched areas are analytic results following Ref. [138, 139] for 300-K thermal atoms, calculated for single three-level Λ systems involving the excited states $F' = 2$ (blue, diagonally hatched) or 3 (purple, vertically hatched). The ground state decoherence rate $\gamma_g/2\pi$ is varied from 30 kHz to 40 kHz over the shaded hatched regions. The different trends are due to different Rabi frequencies from the beam center for a given laser power and beam size (see text for detail). The orange curve is a simulation result (see Appendix for details) in which both Raman-degenerate Λ systems with $F' = 2$ and 3 are accounted for, as described in the text. The variation of the Rabi frequencies transverse to the beam directions is included, and $\gamma_g/2\pi$ is 35 kHz. The orange-shaded, horizontally hatched region represents a sweep of $\gamma_g/2\pi$, the only fitting parameter in the model, from 30 kHz to 40 kHz. The insert shows a histogram of the "Beam Exposure Period (BEP)" defined in text; the bin size is 2 μs and the most probable BEP is $t^* = 33$ μs.

thermal vapor cells with buffer gases [127, 128], which clearly does not apply to our case. An analytic result for a single Λ system in a Doppler-broadened system, given in Ref. [138, 139, 140, 153], reproduces the general trends in our data (blue and purple hatched areas) in terms of approximate line width values as well as the linear scaling of the width with Rabi frequency (which is linear in distance along the x-axis in Figure 6.8). The remaining mismatch between the analytic result and our measurements, together with the exponential-decay-like line shape (Figure 6.7(b)), motivate us to investigate the effects caused by (1) the presence of two Raman-degenerate Λ systems and (2) by the transverse inhomogeneity of the laser intensities (thus the Rabi frequencies) away from the beam axes.

Before discussing the EIT line width in more detail, we recall that in the $B = 0$ analysis two Raman-degenerate Λ configurations involving two different velocity classes contribute to the EIT signal. This remains true at $B = 6$ Gauss, with the velocity groups resonantly coupled to states $|5P_{3/2}, F', m_F = 0\rangle$ differing by about 50 m/s for $F' = 2$ and 3. Since this velocity difference is much less than the RMS thermal velocity of 170 m/s in one dimension (at our cell temperature of 303 K), both Λ configurations contribute to the EIT line and its width. Further, angular matrix elements and Rabi frequencies depend strongly on magnetic field due to the onset of hyperfine de-coupling in the excited state. At 6 Gauss and for the given circular polarizations, the angular matrix elements, $w_{i,F'}$, are 0.2630 and 0.5825 for probe and coupling laser transitions resonant with $|5P_{3/2}, F' = 2, m_F = 0\rangle$, respectively. For probe and coupling laser resonant with $|5P_{3/2}, F' = 3, m_F = 0\rangle$, they are 0.4140 and 0.3323. It should be noted that these angular matrix elements are significantly different from those at zero magnetic field due to magnetic-field-induced state mixing in the excited-state manifold [154, 155]. The Rabi frequencies are then given by $\Omega_{i,F'} = \Gamma\sqrt{I_i/(2I_{sat})} \times w_{i,F'}$,with $\Gamma = 2\pi \times 6$ MHz and $I_{sat} = 1.67$ mW/cm^2. Subscript i stands for probe or coupling. These Rabi-frequency expressions are used in Figure 6.8, with the given beam powers and widths.

In our numerical model, we integrate three-level Lindblad equations for an ensemble of atom trajectories with random initial velocities, drawn from a 3D Maxwell distribution, and random initial positions on the cell walls or windows. Since the two Raman-degenerate Λ EIT resonances, mentioned above, are only a few m/s wide in velocity space, for any given atom trajectory we select the upper-state F'-level that is closer to resonance with the probe laser, in the frame of reference of the moving atom, and solve the three-level Lindblad equation with that F' level. In addition, the transverse laser intensity distributions are accounted for via spatially dependent Rabi frequencies. Also, the vapor opacity in our experiment is kept at a sufficiently low value that the longitudinal intensity variation of the beams, caused by absorption, can be neglected. A more detailed description can be found in

the Appendix. In this simulation, the ground-state decoherence rate, γ_g, is the only fitting parameter. As shown in Figure 6.8, the numerical simulation (solid orange line) fits our data very well for $\gamma_g/2\pi = 35$ kHz, with a confidence range of about 30 kHz to 40 kHz (orange hatched area).

6.5 Discussions and Conclusions

We note that in Ref [138, 139] the decay of the coherence ρ_{12} is modeled via a bidirectional symmetric population transfer rate between the two ground states, $|1\rangle$ and $|2\rangle$. This mechanism is useful to describe open systems where atoms move in and out of an interaction region [139, 156], and it may also be used to describe the population decay due to atom-wall collisions. In our work we adopt the model from Ref [35], where the decay of the coherence ρ_{21} is modeled through dephasing only, while the ground-state population exchange occurs exclusively via optical pumping through the excited state (for details see Sec. 6.6).

In our next discussion point, we draw a distinction between dephasing of ρ_{21} and interaction-time broadening. Both effects are ubiquitous in thermal-gas experiments. An analytic approach can be found in Ref. [142]. Compared to experiments using atomic beams or cold atoms, interaction time in the vapor cell can be thought of as the beam exposure period ("BEP") i.e. the time of flight of the atoms through the laser-beam core, defined as the region with diameter $2w_p$ and length of L, where $w_p = 6.5$ mm is the usual 1/e-dropoff radius of the electric field in our Gaussian beams, and $L = 70$ mm is the length of the vapor cell. The BEP is broadly distributed due to beam and cell geometry, randomness in atom velocity, and randomness in trajectory orientation relative to cell and beams. Here, the most probable value of the BEP $t^* = 33$ μs (see insert of Figure 6.8). Over a range of numerical tests we have seen that $t^* \approx a \times (2w_p/u)$, with a numerical constant $a = 0.51$ and the most probable speed for a 3D Maxwell velocity distribution $u = \sqrt{2k_BT/m_{Rb}}$. The tests have also shown that a depends somewhat on the geometric ratios w_p/R and R/L; it varies by about 20% from the quoted value for w_p/R varying from 0.2 to 0.8 and R/L from 0.1 to 0.5. An analytic expression for a 2D scenario can be found in Sec. 1.2.3. Our 3D numerical model includes effects caused by the end windows of the cell. Our numerical survey indicates that the end windows modify the 2D analytic result significantly when the R/L ratio becomes large.

According to our numerical model, the zero-power line width is about $2\gamma_g \approx 2\pi \times 70$ kHz. Interaction-time broadening, which is on the order of $1/t^* \approx 30$ kHz, is included in our simulation in Figure 6.8 and has a relatively minor effect on the simulated zero-

power line width. The lowest line width experimentally measured, about 100 kHz, is still slightly affected by power broadening. It is noted that the experimental uncertainty bars in Figure 6.8 increase at low powers due to the decrease in photo-current. Even at the lowest powers, experimental and simulated line widths agree within the experimental uncertainty.

The question arises where the decoherence γ_g comes from. Decoherence due to the spin exchange collisions between Rb atoms is an unlikely cause, as it is only on the order of tens of Hz [157] at our vapor density (about $10^{10}\mathrm{cm}^{-3}$). Also, differential phase noise between coupling and probe lasers is an unlikely cause, because the residual phase noise of the OPLL is only 0.3 rad, and the spectral width of the laser beat signal at 3 GHz has been directly measured to be below about 3 Hz.

Looking at other causes, we note that recent spin noise measurements of Faraday rotation signals [158, 131] carried out in buffer-gas free Rb vapor cells have revealed that the ground state $1/T_2$ rate can vary from kHz to hundreds of kHz, depending on whether the cell walls are coated with anti-relaxation layers or not. Models provided in Ref. [131] also suggest that as low as a few mTorr background gas, which can either come from the outgassing of the coating layer or an impurity introduced during cell manufacturing, can reduce the mean free path of the Rb atoms from meters (much larger than practical cell size) to millimeters (which is on the order of typical optical beam sizes). Since the effects of collisional interactions on quasi-steady-state EIT spectra are not covered in our ballistic model, while wall interactions are effectively included via the BEP time limitation and a random initialization of the ground state population distribution before the atoms desorb from the wall/window, we speculate that the decoherence measured in our work may originate in collisions with an impurity gas.

In conclusion, we have explored Λ EIT in a Rb vapor cell on the D2 line as a means to study EIT line-width suppression in a Doppler-broadened medium. Lifting Zeeman degeneracies by application of a homogeneous magnetic field of 6 Gauss has allowed us to focus the study on a single, magnetic-field-insensitive EIT line, and to push our study of EIT line width vs beam intensity into the 100-kHz regime. We have qualitatively explained the EIT line width behavior using existing analytical models and achieved quantitative agreement using a numerical approach in which we have included experimentally relevant details. We have observed a remaining ground-level dephasing rate $\gamma_g/2\pi \sim 35$ kHz that could not be readily explained. We have discussed possible causes for γ_g. In this context, one may explore the Λ EIT line width as a measure to analyze residual gases in closed cells, where tools such as residual gas analyzers cannot be used. In future, improved models may be developed to account for effects introduced by optical pumping and atomic decay [90, 159] among all magnetic sublevels in both $|5S_{1/2}\rangle$ and $|5P_{3/2}\rangle$ hyperfine manifolds. Effects

induced by state mixing via transverse magnetic fields and impurities in laser polarization states and frequency spectra may also be included.

6.6 Numeric Modeling

A three level Λ-type model is implemented with $|5S_{1/2}, F = 3, m_F = 1\rangle$ as state $|1\rangle$, $|5S_{1/2}, F = 2, m_F = -1\rangle$ as state $|2\rangle$, and $|5P_{3/2}, F', m_F = 0\rangle$ as state $|3\rangle$. Atoms move on trajectories $\boldsymbol{r}(t) = \boldsymbol{r}_0 + \boldsymbol{v}_0 t$ with initial random velocities $\boldsymbol{v}_0$ from a 3D Maxwell distribution, and initial positions $\boldsymbol{r}_0$ randomly chosen on cell walls/windows. States $|1\rangle$ and $|3\rangle$ are coupled by a position-dependent probe Rabi frequency $\Omega_p(\boldsymbol{r}(t))$, and states $|2\rangle$ and $|3\rangle$ by a coupling laser Rabi frequency $\Omega_c(\boldsymbol{r}(t))$. The system has two sets of Λ couplings, one for $F' = 2$ and another for $F' = 3$. For each atom of the ensemble, the F'-value in state $|3\rangle$ is picked such that the Doppler shift of the EIT lasers in the atom's rest frame is minimized for the atom's $\mathbf{v}_0$-value. This is allowed because the internal-state dynamics is usually dominated by the Λ system the atom is closer in resonance with.

The position-dependent Rabi frequencies $\Omega_{c,p}$ are given by $\Omega_{c,p}(\boldsymbol{r}) = \boldsymbol{\mu}_{ij} \cdot \boldsymbol{E}_{c,p}(\boldsymbol{r})/\hbar$ where $\boldsymbol{\mu}_{ij}$ is the transition electric dipole moment between state $|i\rangle$ and $|j\rangle$, and $\boldsymbol{E}_{c,p}(\boldsymbol{r})$ are electric fields with Gaussian transverse profiles. The dipole moments $\boldsymbol{\mu}_{ij}$ are obtained by diagonlization of the atomic Hamiltonian with all Zeeman and hyperfine interactions included. The dipole moments depend significantly on the magnetic field. At $B = 6$ Gauss and for the laser polarizations used, for $F' = 2$ it is $\mu_{31} = 1.46ea_0$ and $\mu_{32} = 3.23ea_0$, and for $F' = 3$ it is $\mu_{31} = 2.30ea_0$, $\mu_{32} = 1.84ea_0$.

In the two-color field picture (which is applicable to systems with fields of sufficiently different frequencies), the atom-laser interaction Hamiltonian in the space $\{|1\rangle, |2\rangle, |3\rangle\}$ is

$$H_{int} = -\frac{\hbar}{2}\begin{bmatrix} 0 & 0 & \Omega_p(\boldsymbol{r}) \\ 0 & -2(\Delta_1 - \Delta_2) & \Omega_c(\boldsymbol{r}) \\ \Omega_p(\boldsymbol{r}) & \Omega_c(\boldsymbol{r}) & -2\Delta_1 \end{bmatrix} \tag{6.1}$$

where $\Delta_1 = \omega_p - \omega_{31} - \boldsymbol{k}_p \cdot \boldsymbol{v}_0$ and $\Delta_2 = \omega_c - \omega_{32} - \boldsymbol{k}_c \cdot \boldsymbol{v}_0$ are the velocity-dependent detunings of the fields relative to the atomic transition frequencies ω_{ij}.

The dynamics of the laser-driven atomic system is described by the Lindblad equation for the density operator ρ,

$$\begin{aligned} \frac{\mathrm{d}\rho}{\mathrm{d}t} = & \quad \tfrac{1}{i\hbar}[H_{int}, \rho] \\ & + \tfrac{\Gamma_{31}}{2}[2\hat{\sigma}_{13}\rho\hat{\sigma}_{31}, -\hat{\sigma}_{33}\rho - \rho\hat{\sigma}_{33}] \end{aligned}$$

$$
\begin{aligned}
&+\tfrac{\Gamma_{32}}{2}[2\hat{\sigma}_{23}\rho\hat{\sigma}_{32}, -\hat{\sigma}_{33}\rho - \rho\hat{\sigma}_{33}] \\
&+\tfrac{\gamma_1}{2}[2\hat{\sigma}_{11}\rho\hat{\sigma}_{11}, -\hat{\sigma}_{11}\rho - \rho\hat{\sigma}_{11}] \\
&+\tfrac{\gamma_2}{2}[2\hat{\sigma}_{22}\rho\hat{\sigma}_{22}, -\hat{\sigma}_{22}\rho - \rho\hat{\sigma}_{22}] \\
&+\tfrac{\gamma_3}{2}[2\hat{\sigma}_{33}\rho\hat{\sigma}_{33}, -\hat{\sigma}_{33}\rho - \rho\hat{\sigma}_{33}]
\end{aligned} \tag{6.2}
$$

with atomic projection operators $\hat{\sigma}_{ij} = |i\rangle\langle j|$, dephasing rates γ_1, γ_2 and γ_3, and partial spontaneous decay rates Γ_{31} and Γ_{32}. The latter, within the Weisskopf-Wigner approximation, are given by [82],

$$
\Gamma_{3i} = \frac{4}{3}\alpha_{\mathrm{FS}}\frac{1}{2F_3+1}\frac{\omega_{3i}^3}{c^2}(2F_3+1)(2F_i+1)\left[\langle 5P_{3/2}\|r\|5S_{1/2}\rangle \begin{Bmatrix} J_3 & 1 & J_i \\ F_i & I & F_3 \end{Bmatrix}\right]^2 \tag{6.3}
$$

where α_{FS} is the fine structure constant, F_i and J_i are the F and J quantum numbers of state $|i\rangle$, $\langle 5P_{3/2}\|r\|5S_{1/2}\rangle = \sqrt{2J_i+1}\times 4.23a_0$ is the reduced dipole matrix element of the D2 transition of ^{85}Rb [160], and $\{*\}$ represents the Wigner-6J symbol. Using this equation, $\Gamma_{31} = 2\pi\times 1.35$ MHz and $\Gamma_{32} = 2\pi\times 4.72$ MHz for state $|3\rangle = |5P_{3/2}, F'=2, m_F=0\rangle$, and $\Gamma_{31} = 2\pi\times 3.37$ MHz and $\Gamma_{32} = 2\pi\times 2.70$ MHz for $|3\rangle = |5P_{3/2}, F'=3, m_F=0\rangle$. The total spontaneous decay rate Γ_3 of state $|3\rangle$ is $\Gamma_3 = \Gamma_{31}+\Gamma_{32} = 2\pi\times 6.07$ MHz, the natural decay rate of Rb $5P_{3/2}$.

The decoherence rate γ_3 is dominated by laser-frequency noise. The lasers are locked via standard saturation-absorption-spectroscopy, with an estimated $\gamma_3 \sim 2\pi\times 200$ kHz. The exact value is not important because γ_3 does not affect the line width of the EIT signal [35].

For simplicity, we set $\gamma_1 = \gamma_2 = \gamma_g$ in our discussion. The decoherence rate γ_g includes noise on the frequency difference of coupling and probe lasers and collisional ground-state level dephasing. The former is very small, due to our use of an OPLL, while the latter could be several tens of kHz due to collisions between Rb atoms and cells walls or trace gases inside the cell. Here we find a fitted $\gamma_g \approx 2\pi\times 35$ kHz.

We numerically integrate the Lindblad equation for a large ensemble of trajectories with randomly chosen velocities $\boldsymbol{v}_0$ and initial positions $\boldsymbol{r}_0$, as explained above. The initial populations are set to be randomly distributed between states $|1\rangle$ and $|2\rangle$, with $\rho_{11}(t=0)+\rho_{22}(t=0)=1$. The position-dependence of the Rabi frequencies, $\Omega_{c,p}(\boldsymbol{r})$, enters in the time integration via the atom trajectories, $\boldsymbol{r}(t) = \boldsymbol{r}_0 + \boldsymbol{v}_0 t$. The integration for a given atom ends when its trajectory exits the cell volume (i.e., hits a wall/window). The absorption signal and the EIT then follow

$$\frac{1}{N}\sum_{j=1}^{N}\int_{0}^{T_j}\mathrm{Im}[\rho_{31}(t;j)]\mathrm{d}t \tag{6.4}$$

where j is a trajectory label, N the number of trajectories, and T_j the time of flight of atom j through the cell.

CHAPTER 7

Engineering Efforts toward Glass-Silicon Spectroscopy Cells

7.1 Integration of Conductive Silicon as Control Electrodes

Due to charge accumulations inside the glass vapor cell, EIT signals are sensitive to local fields generated by stray electric fields inside the cell. Tuning or zeroing these stray electric fields using external electrodes outside the glass cell is difficult [3].

One approach to working around this is to integrate the electrodes into the cell body. In this approach, the electrodes not only serve as the source/drain of the charges but also as parts of the cell walls. Feedthrough structures are not necessary since these electrodes can be directly accessed from outside the cell. Highly doped conductive silicon and anodic bonding are the two technical pillars that make this idea a reality. This technique also has great potential to minimize the overall device size by utilizing mature nanofabrication technology in the silicon industry.

Fig. 7.1 shows a prototype cell with conductive silicon rings as integrated electrodes. In the following sections, I document the design considerations, manufacturing procedures, and preliminary testing data of this prototype cell.

7.1.1 Introduction to Anodic Bonding Process

In the late 1960s, G. Wallis and D. I. Pomerantz at P. R. Mallory & Co. Inc. in Burlington, Massachusetts, demonstrated a new glass-metal sealing method with the assistance of external static electric fields [161]. In their initial demonstration, various insulating glass materials, such as soda lime, borosilicate, fused silica, and quartz, successfully bonded with metals and alloys, such as tantalum, titanium, and Kovar, and semiconductors, such as silicon, germanium, and gallium arsenide. Although the microscopic bonding mechanism was not fully verified until years later, they outlined a few key experimental parameters

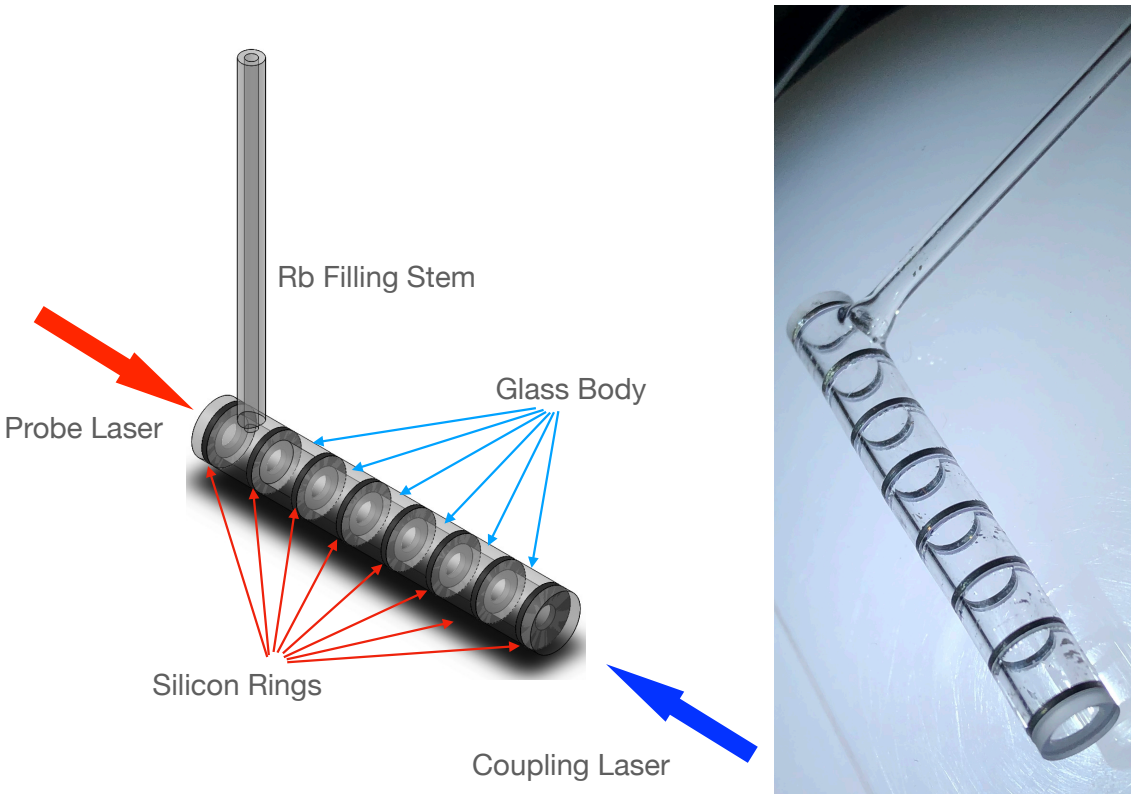

Figure 7.1: Multi-layered anodic bonded spectroscopy cell using conductive silicon rings as electrodes for stray electric field control.

that were essential to the success of the bonding, some of which are summarized in the following.

1) Temperature. Most of the bonding work has been done at temperatures range of 300 to 600 °C. These temperatures are well below the softening temperatures of the glass materials used. Quartz (with a softening temperature of 1200 °C), for instance, successfully bonds to silicon films at 800 °C.

2) Voltage. The voltages used to create the static electric fields are found in the range of 200 to 2000V. A practical upper limit was imposed to avoid sparking among the bonding components. Estimation suggested that the initial local microscopic static electric fields between the bonding surfaces were on the order of 10^6 V/cm.

3) Thermal expansions Close matches of the thermal-expansion coefficients are required between the bonding components. This requirement can be greatly relaxed, however, if one of the bonding parts is in the form of thin film or foil.

Anodic bonding between glass and metal parts is caused by the formation of an ox-

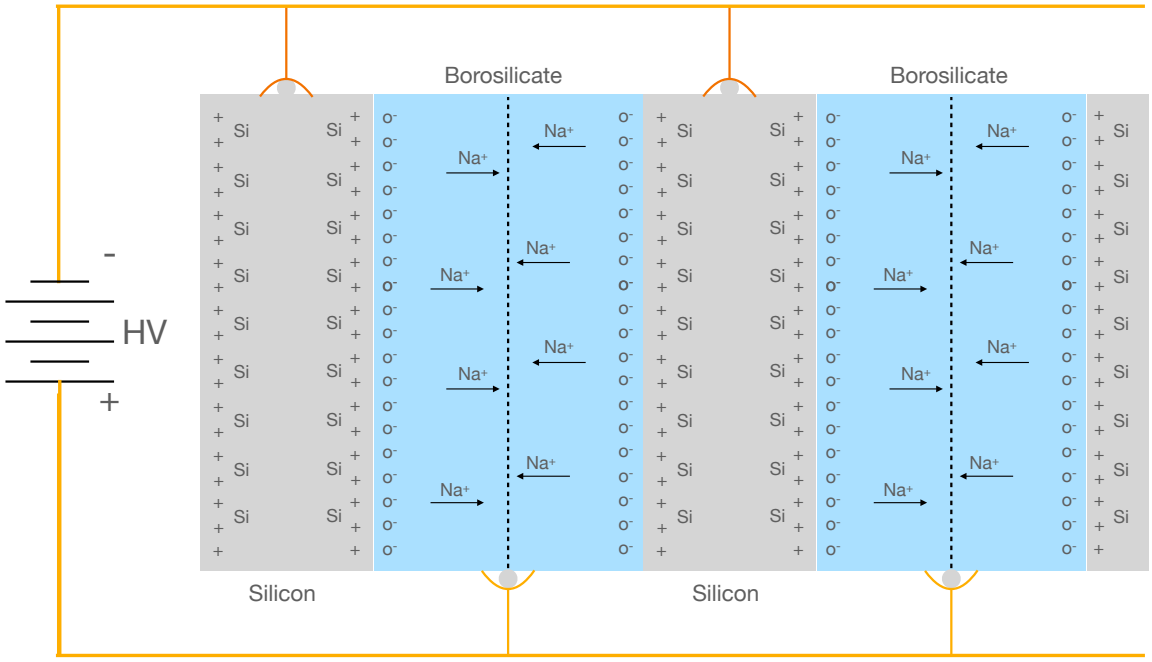

Figure 7.2: Schematic illustration of the anodic bonding between borosilicate glass and silicons. Yellow lines represent copper wires through which the high voltages are applied.

idation layer at the interface of the two materials. Take the anodic bonding between the borosilicate glass and semiconductor silicon, for example. As illustrated in Fig. 7.2, at a temperature of 300 °C, the mobility of the sodium and oxygen ions in the borosilicate glass increases in the presence of an external field. As the oxygen ions drift toward the interface, they combine with the surface Si atoms to form a thin atomic layer of SiO_2. Detailed studies of the bonding mechanism can be found in [162, 163, 164].

7.1.2 Preparation of Glass and Silicon Components

The surfaces roughness requirement for successful anodic bonding is not stringent. For application of making a spectroscopy cell, though, we require not only the glass and silicon pieces to be bonded, but also the formation of an ultra-high vacuums seal such that Rb vapor can be filled and sealed. A hermetic seal suitable for this vacuum requires completely scratch-free bonding surfaces. Therefore, polishing and lapping processes are needed to eliminate any microscopic scratches before the bonding process.

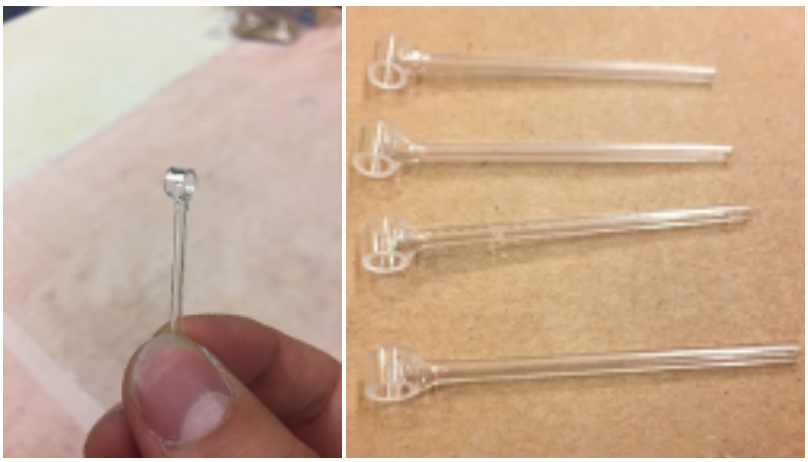

Figure 7.3: T-shaped glasses with filling stems. The longer, thinner stem is used as a Rb filling channel. The shorter, thicker cylindrical part attached on top of the filling stem is used for anodic bonding to silicon parts. These two parts are attached to each other using traditional glass-blowing techniques.

Silicon wafers with high surface quality are commercially available; we only needed to prepare the surfaces of the glass pieces. In this subsection, I document the lapping process developed for this project.

A special glass piece needed for this devices is a T-shaped piece with a filling port. See Fig. 7.3 for details. In order to lap the bonding surface on this piece, a special holding jig is made. beeswax is used to hold the glass pieces to the jig as shown in Fig. 7.4.

Once the lapping glass pieces are securely mounted onto the lapping machine, the lapping procedures can be started. This procedures are developed to suit the special lapper (Fig. D.1) used in Lurie Nanofabrication Facility (LNF) at the University of Michigan. The details are outlined in Appendix. D

7.1.3 Surface Quality Check

The images of the lapped surface are shown in Fig. 7.5 (a) to (e). These images are taken using Olympus BX51 microscope with differential interference contrast (DIC) microscopy capability at LNF. DIC is a technique that enhance the contrast in a semi-transparent sample. By slightly displacing (or shearing) two orthogonally polarized imaging beams, an interference contrast can be detected when the two imaging beams are recombined at the photo detector. This interference contrast is extremely sensitive to the optical path length difference at the local imaging spot on the sample. After properly decoding of the photo detector signals, the contrast of the microscopic images can be rendered to boost the local disturbances of the imaging sample. Due to the details of the beam path arrangement, DIC

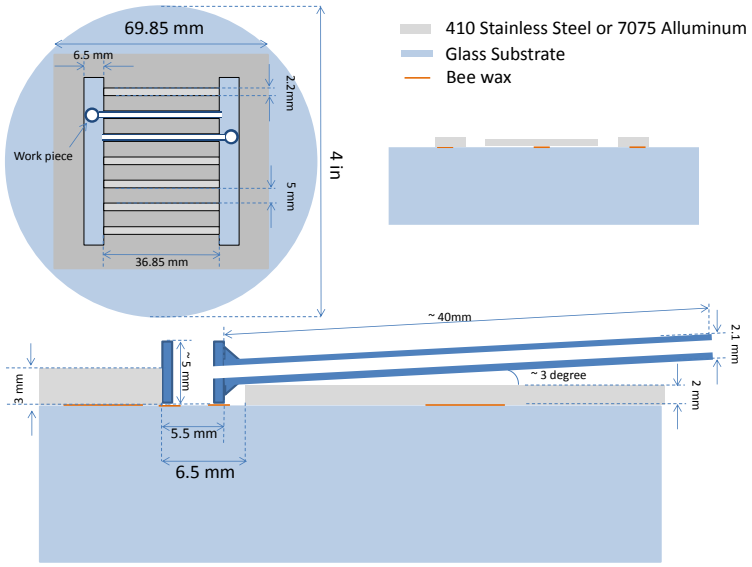

Figure 7.4: The T-shaped stem pieces hold the holding jig (the gray part) using beeswax. They both hold onto a glass substrate that can be mounted onto the lapping machine.

can not measure the exact optical path length difference in the z-direction or the height differences on the sample surface.

During the mechanical lapping stages (see details in Appendix D), the glass material comes off unevenly due to the microscopic stress fluctuation that remain inside the glass. This is responsible for the pit-like structures shown in Fig. 7.5. To remove these irregularities, a chemical-mechanical-polishing (CMP) stage is necessary. In this stage, the polishing slurry contains not only a mechanical polishing compound (colloidal silicon dioxide micro beads) but also an erosive chemical solution (KOH based).

The ultimate roughness of surfaces must be checked by AFM spectroscopy. The AFM imaging is performed using the Bruker ICON AFM at the LNF. This commercial AFM utilizes a cantilever modulated AFM tip to image the surface. The resonance frequency of the cantilever tip depends on the force (or force spatial gradient) applied to the tip, while the force (and thus its gradient) depends on the distance between the sample surface and tip. The interaction can be van der Waals, electrostatic, etc. By monitoring the resonance frequency using lock-in detection and PID controls, we can map the surface height information. Fig. 7.6 shows typical results. The local roughness R_a defined by Eq. 7.1 is on the order of 0.5 nm.

$$R_a = \frac{1}{l}\int_0^l |Z(x)|\mathrm{d}x \approx 0.5\ \mathrm{nm} \tag{7.1}$$

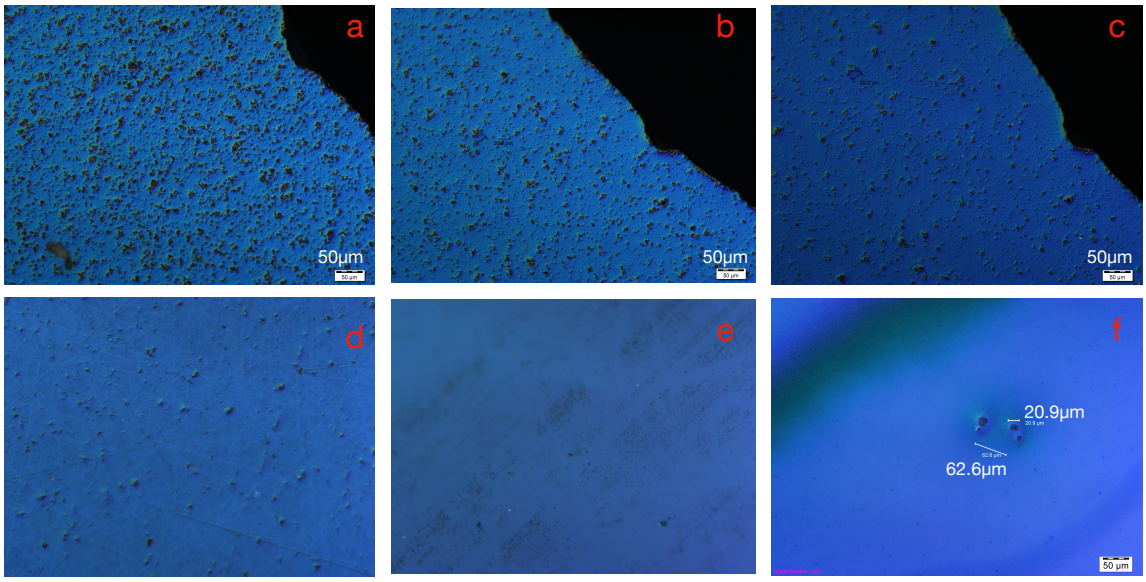

Figure 7.5: Lapping surfaces images after (a) 9μm lapping stage (a), (b) 5μm stage,(c) 3μmstage, (d) 1μm and (e) Chemical-Mechanical-Process(CMP) stage. (f) Typical size of the residual pits.

7.1.4 Setups for simultaneous multi-layer anodic bonding

Special anodic bonding jigs are necessary for making a multi-layer cell shown in Fig. 7.1. In order to test out the anodic bonding process with the silicon rings sandwiched between the glass pieces, a prototype bonding jig shown in Fig. 7.7 is implemented. This bonding jig has a compact design such that the whole piece can be heated up evenly on the surface of a hot plate to a bonding temperature of 300 °C

The bonding pieces lay on the top of two supporting ceramic rods. To ensure the initial contact at the beginning of the bonding process, the bonding pieces are pre-clamped by the setscrews on the side. The high voltage needed for the anodic bonding is fed through conducting metal rails going through the center of the ceramic rods. Thin copper wires are used to connect the silicon rings to the high voltage rail. These detalis are labeled in the Fig. 7.7.

This prototype paved the way for a more general multi-layered design shown in Fig. 7.8. This bonding jig enables us to make a multi-layered spectroscopy cell shown in Fig. 7.1. Such a multi-layered design enables us to demonstrate the 1) local electric field tuning ability and 2) microwave polarization filtering capability. Both of the two functionalities play important roles in developing field-applicable electromagnetic field sensors. We will discuss some preliminary experimental tests on these two topics in the next following sections.

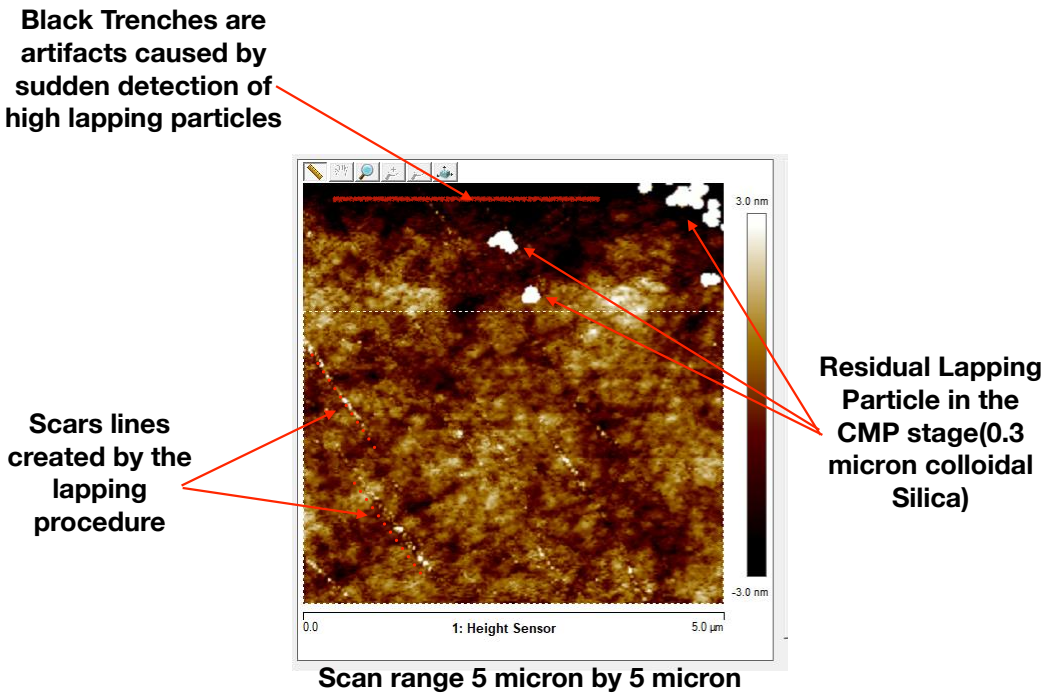

Figure 7.6: Typical AFM Image after CMP lapping

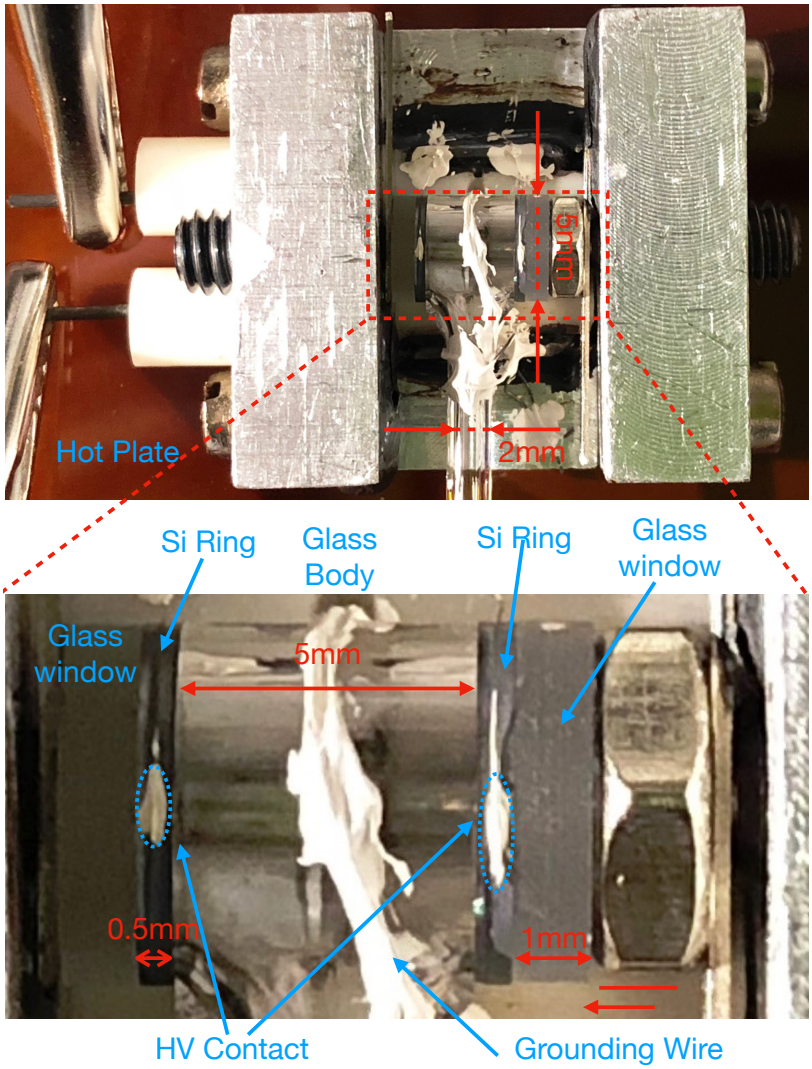

Figure 7.7: Anodic bonding test jig for bonding the T-shaped glass piece to the spectroscopy windows with the conductive silicon rings in between

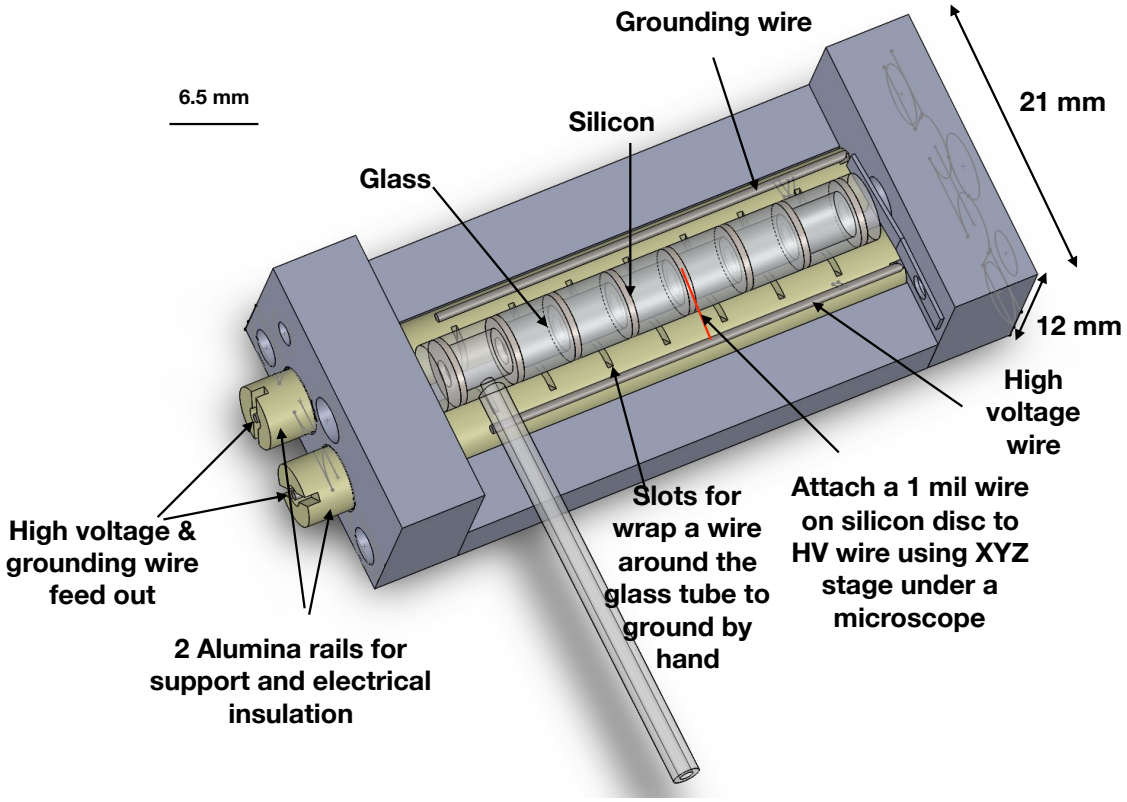

Figure 7.8: Jig design for simultaneous multi-layer anodic bonding

7.2 Prototype Functional Testing

7.2.1 DC Fields Injection and Local Fields Control

First, we tested our device for DC electric field injection capability using the setup shown in Fig. 7.9. The strength of the DC field inside the cell can be monitored through the DC Stark shift of the Rydberg EIT signal. In this test, $32S_{1/2}$ Rydberg state with a DC polarizability α of 2.21353 MHz/(V/cm)^2 is used. As indicated by Fig. 7.10, a relatively uniform DC field of 1V/cm is easily achievable by applying a moderate 10 volts applied to silicon ring electrodes.

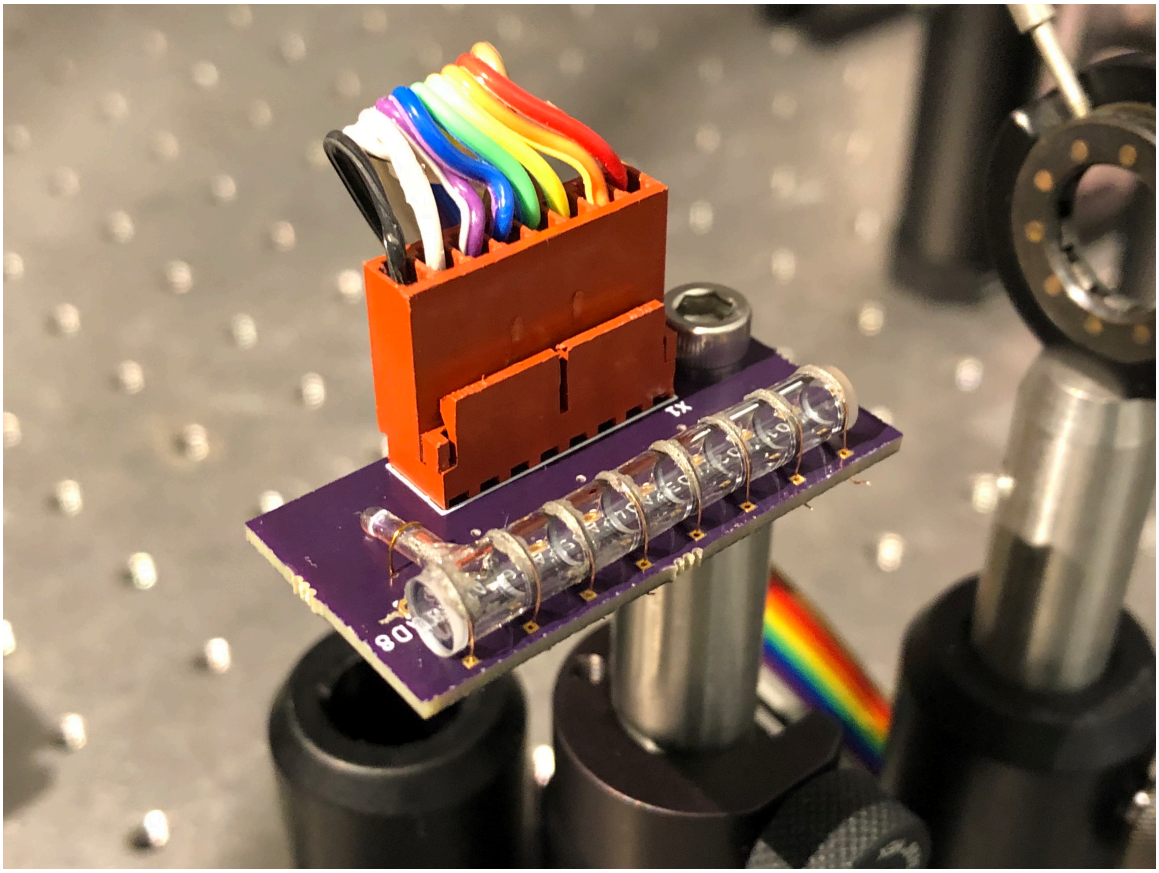

Figure 7.9: Picture of the setup used for the DC field injection test. Individual voltages can be applied to each highly conductive silicon ring electrode through the rainbow colored ribbon cable. Thin copper wires are attached to the silicon ring outside the cell. Sliver paste is used to increase the contact area between the out rim of the silicon ring and the copper wire.

In addition to a uniform DC fields injection, by applying voltage to only one electrode, the EIT spectrum demonstrates a new peak on the red side of the major signal as shown in Fig. 7.11. This is the evidence that a quadratic electric potential fields can be created

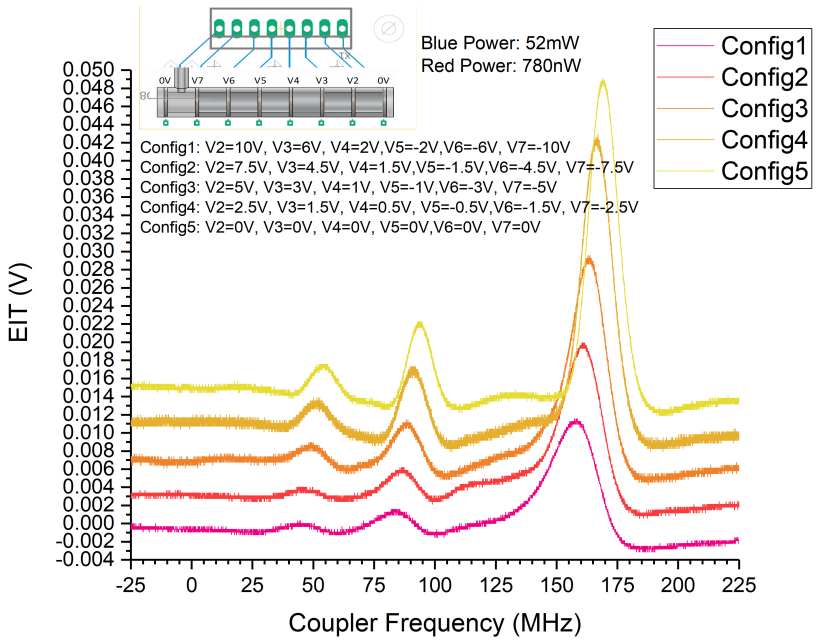

Figure 7.10: EIT signals show distinctive DC stark shifts for various configurations where voltages are applied to the high conductive silicon rings. Note that the voltage difference between the adjacent rings are kept constant in each configuration.

inside the cell, which shows that we can create local electromagnetic trap pockets inside the cell for charged particles with additional external magnetic fields. This is helpful to further investigate the charge particle generations during the EIT measurement.

7.2.2 RF/MW fields polarization filtering

In the past decade, researchers have been developing high-sensitivity RF/MW fields with Rydberg-enabled sensors. Unlike DC electric fields, RF/MW fields travel through the glass cell walls and interact strongly with Rydberg atoms. For sensitive RF/MW polarization measurements, a certain amount of polarization selectivity is desired. Due to the multi-layered structure and high conductivity of the silicon rings, this glass-silicon integrated prototype cell itself can be used as an RF/MW polarization filter without any additional add-on components.

Based on the separation between the two silicon rings, this device is sensitive to RF/MW with frequency around 22 GHz. Driven by the applied fields oscillating along the cell axis, these silicon rings produce additional fields that constructively add to the driving fields inside the cell. When the silicon rings are driven by external fields polarized perpendicular to the cell axis, the secondary fields destructively add to the external ones. Thus, the

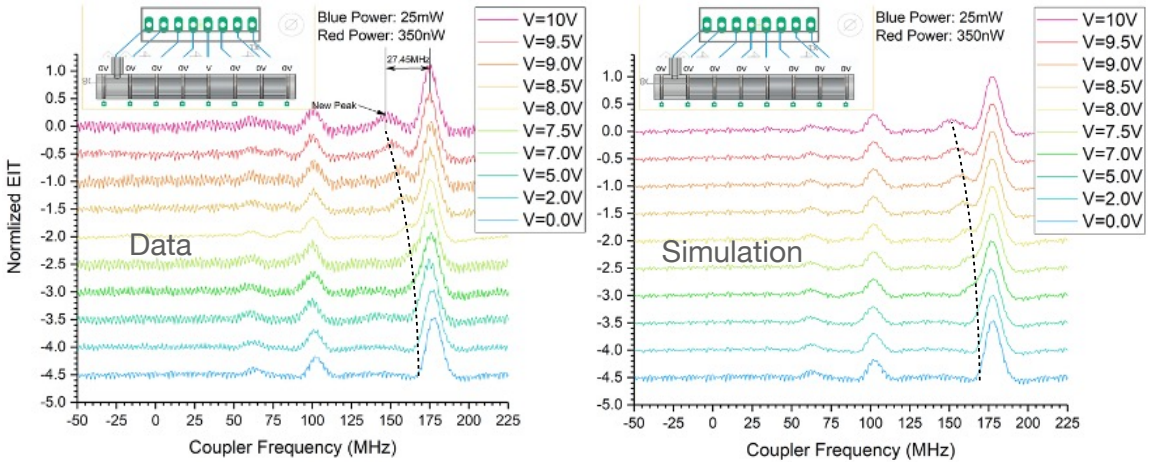

Figure 7.11: EIT signals (left) and simulation data (right) for the configuration where only the center conductive silicon ring is charged. As the voltage increases, a new peak emerges on the red detuned side of the main EIT signal. This new resonance is created by a local maximum of the electric fields. The detailed simulation indicates that a local quadratic potential is responsible for this peak.

cell exhibits polarization-dependent transmission for RF/MW fields traveling from outside to inside.

Fig. 7.12 shows a high-frequency MW simulation at 18.14 GHz that confirms this polarization selectivity. In this simulation, the external MW fields was generated by a microwave horn. The polarization was set to align with the shorter edge of the horn openings (the vertical direction in Fig. 7.12(a)). As shown in Fig. 7.12(c), most of the fields were transmitted into the cell when the polarization of the fields in aligned with the cell longitudinal axis.

We can measured the polarization selectivity of the this prototype cell by performing a MW-Rydberg EIT experiments. MW at 18.14GHz couples the Rydberg state $49D_{5/2}$ to $50P_{3/2}$. This polarization selectivity can be verified by measuring the Autler-Townes splittings of the EIT signal.

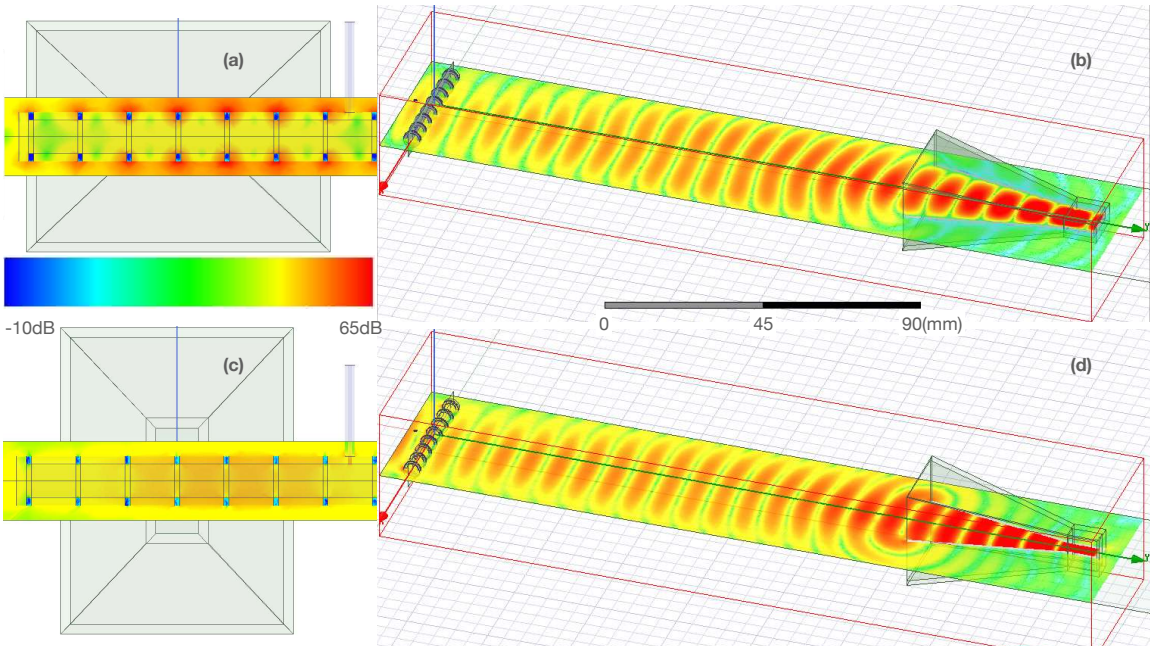

Figure 7.12: High frequency simulation of the MW polarization selectivity of the glass-silicon vapor cell. The colored map corresponds to the magnitude strength $|\boldsymbol{E}_{\mathrm{MW}}|$ of a 18.14GHz MW fields with polarization (a)–(b) perpendicular and (c)–(d) parallel to the cell's longitudinal axis. The microwave horn is also shown together with the cell. The distance between the horn opening and cell is set to about 15cm such that the cell is in far-field region of the microwave horn.

CHAPTER 8

Summary and Outlook

In this thesis, I have summarized and reviewed all the major research activities during my PhD trainings in the Physics Department at the University of Michigan. My research focuses on the topics of electromagnetic field sensing using Rydberg atoms in gaseous phase. Electromagnetically induced transparency (EIT) spectroscopy has been implemented as a major measurement technique; utilizing some of the unique properties of Rydberg atoms, I have explored and demonstrated many novel ideas about the applications of this technology.

In addition to the research activities documented in this dissertation, I also participated in research projects led by my colleagues. One of the most exciting was the demonstration of a new experimental technique to construct a magneto-optical trap (MOT) using millimeter-sized ball lenses [165]. This R&D shows new ways to reduce the physical size of typical cold-atom apparatus significantly, an important first step toward realizing compact, mobile cold-atom quantum machines.

After the discovery of quantum mechanics 100 years ago, we are now in the era of quantum tools and machines. These new technologies will revolutionize industrial productivity, just as steam machines and electricity did a few centuries ago. By the end of my Ph.D. training, I was selected to participate in an internship program at ASML HMI, a semiconductor industry company specializing in manufacturing industry-scale electron microscopic inspection machines. In the business of electron beam spectroscopy, the precise control and monitoring of various electromagnetic fields is a key engineering element that ensures cutting-edge machine capability. From an industrial perspective, the potential applications of Rydberg-enabled electromagnetic field sensing are exciting and promising. I have included some related discussions along this line in Appendix E.

My thesis concludes here, but the dream of utilizing quantum technologies never ends.

APPENDIX A

Step Adjusting Integration Method for Radial Schrodinger Equation

In general, let us consider a differential equation of the form

$$U''(x) = V(x)U(x) \tag{A.1}$$

where x is the independent variable and U is the dependent variable. $V(x)$ is known function for all x in the solution domain.

As shown in Fig. A.1, let us assign x_m, x_0 and x_p ($x_m < x_0 < x_p$) as three adjacent points in the solution domain on which we'd like to seek for numerical approximations, U_m, U_0 and U_p, for dependent function valued at each points i.e. $U(x_m)$, $U(x_0)$ and $U(x_p)$.

Let us examine point x_0, The spatial derivatives of $U(x)$ at $x_0$can be approximated by

$$\begin{aligned} U''(x_0) &\approx \frac{U'(x_{0p}) - U'(x_{m0})}{x_{0p} - x_{m0}} \approx V(x_0)U_0 \\ U'(x_{0p}) &\approx \frac{U(x_p) - U(x_0)}{x_p - x_0} \approx \frac{U_p - U_0}{x_p - x_0} \\ U'(x_{m0}) &\approx \frac{U(x_0) - U(x_m)}{x_0 - x_m} \approx \frac{U_0 - U_m}{x_0 - x_m} \end{aligned} \tag{A.2}$$

By inspecting Eq. A.2, U_m, U_0 and U_p satisfy

$$U_p \approx \frac{U_0\left[V(x_0) + f_m + f_p\right] - U_m f_m}{f_p} \tag{A.3}$$

$$U_m \approx \frac{U_0\left[V(x_0) + f_p + f_m\right] - U_p f_p}{f_m} \tag{A.4}$$

where f_p and f_m are defined as

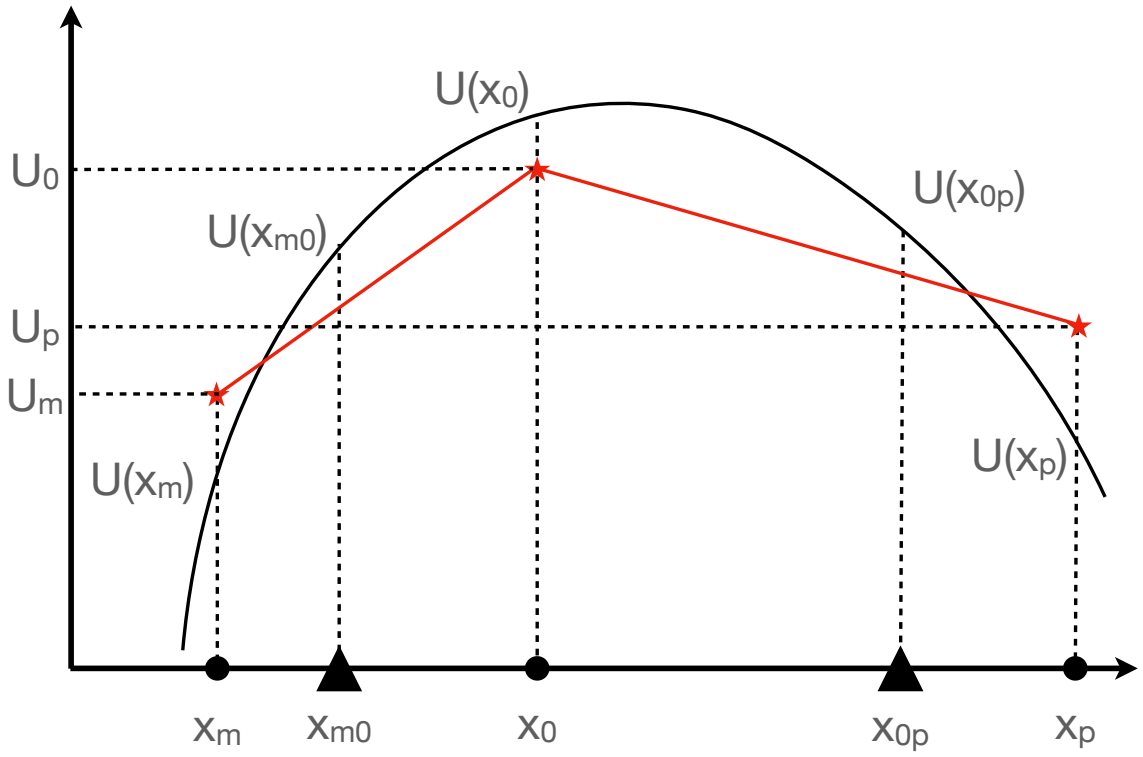

Figure A.1: At three discrete adjacent points x_m, x_0 and x_p, the numerical approximations for $U(x_m)$, $U(x_0)$ and $U(x_p)$ U_m are found to be U_0 and U_p. Points x_{m0} and x_{0p} are arbitrary points located in between x_m, x_o and x_p. The solution of Eq. A.1, $U(x)$ (Solid Black) is then approximated by a piecewise-linear curve (Solid Red).

$$f_p = \frac{2(x_0 - x_m)}{(x_p - x_0)(x_0 - x_m)(x_p - x_m)} = \frac{2}{(x_p - x_0)(x_p - x_m)}$$
$$f_m = \frac{2(x_p - x_0)}{(x_p - x_0)(x_0 - x_m)(x_p - x_m)} = \frac{2}{(x_0 - x_m)(x_p - x_m)} \tag{A.5}$$

For a given x_m, x_0 and U_m, U_0, Eq. A.3 can be used to find U_p. Repeating this procedure, U_x can be integrated outward. Similarly, for a given x_p, x_0 and U_p, U_0, Eq. A.4 can be used to find U_m. Thus the U_x can be integrated inward. Note that the intermediate points x_{m0} and x_{0p} are not used to propagate U and the distances between x_m, x_0 and x_p do not need to be equal. Thus the step size is adjustable.

APPENDIX B

Rotating wave approximation and "dressed atom" picture

We start with the total Hamiltonian $\hat{H}$ which consists of the atomic part $\hat{H}_a$ and the interaction Hamiltonian $\hat{H}_{int}$ for which the electric-dipole approximation is used

$$\begin{aligned} \hat{H} &= \hat{H}_a + \hat{H}_{int} \\ \hat{H}_a &= \sum_j \hbar\omega_j \left|j\right\rangle \left\langle j\right| \\ \hat{H}_{int} &= -\hat{\boldsymbol{d}} \cdot \boldsymbol{E} = -\hat{\boldsymbol{d}} \cdot \boldsymbol{\epsilon}\, E^{real} \end{aligned} \tag{B.1}$$

In the context of the EIT experiment, the electrical field $\boldsymbol{E}$ is usually an optical laser field. In the Microwave-EIT experiment, this field can also be an RF or microwave field in which the oscillation frequency is much slower. In either cases, we assume that this field quasi-monochromatic in the sense that it consists of a dominated oscillation frequency ω_f and a slowly varying envelope $\tilde{E}(t)\boldsymbol{\epsilon}$; as in many cases, it is mathematically convenient to represent a real oscillating electric field $E^{real}(t)$ in a complex form:

$$\boldsymbol{E}(t) = \frac{1}{2}\boldsymbol{\epsilon}\left[\tilde{E}(t)\, e^{-i\omega_f t} + \text{c.c.}\right] \tag{B.2}$$

Note that the field $\boldsymbol{E}$ defined above is a real quantity, while the envelope function $\tilde{E}$ and the polarization unit vector $\boldsymbol{\epsilon}$ can generally be complex valued.

The basis state $\left|j\right\rangle$ satisfies the time-dependent Schrödinger equation with the atom Hamiltonian $\hat{H}_a$:

$$i\hbar\partial_t \left|j\right\rangle = \hat{H}_a \left|j\right\rangle \tag{B.3}$$

It also rotates at an angular frequency ω_j:

$$\left|j(t)\right\rangle = \left|j(t=0)\right\rangle e^{-i\omega_j t} \tag{B.4}$$

In order to make things easier, we also label our the eigenstate with the lowest energy as state $|1\rangle$ and so on

$$\omega_1 < \omega_2 < \cdots < \omega_j < \omega_i < \cdots \tag{B.5}$$

We also define the notation ω_{ij} as the energy difference between $|i\rangle$ and $|j\rangle$

$$\omega_{ij} = \omega_i - \omega_j \tag{B.6}$$

Please note the order of the subscript i and j in the definition.

Using the dipole matrix element $\boldsymbol{d}_{ij} = \langle i|\, \hat{\boldsymbol{d}}\, |j\rangle$, we can express $\hat{\boldsymbol{d}}$ as

$$\hat{\boldsymbol{d}} = \sum_{i>j,\ j} \left(\boldsymbol{d}_{ij}\, |i\rangle\, \langle j| + \boldsymbol{d}_{ji}\, |j\rangle\, \langle i|\right) \tag{B.7}$$

Using Eq. B.2 and Eq. B.7, the interaction Halmitonian $\hat{H}_{int}$ can be shown containing terms like

$$\begin{aligned}\hat{H}_{int} = -\frac{\hbar}{2} \sum_{i>j,\ j} \Bigg(&\frac{\boldsymbol{d}_{ij}\cdot\boldsymbol{\epsilon}\tilde{E}}{\hbar} e^{-i\omega_f t}\, |i\rangle\, \langle j| + \frac{\boldsymbol{d}_{ji}\cdot\boldsymbol{\epsilon}\tilde{E}^*}{\hbar} e^{i\omega_f t}\, |j\rangle\, \langle i| + \\ &\frac{\boldsymbol{d}_{ij}\cdot\boldsymbol{\epsilon}\tilde{E}^*}{\hbar} e^{i\omega_f t}\, |i\rangle\, \langle j| + \frac{\boldsymbol{d}_{ji}\cdot\boldsymbol{\epsilon}\tilde{E}}{\hbar} e^{-i\omega_f t}\, |j\rangle\, \langle i| \Bigg)\end{aligned} \tag{B.8}$$

Up to now, we have been describing our system in the Schrödinger picture. Next we introduce the first unitary transformation $\hat{U}_I$ which brings us from the Schrödinger picture to the interaction picture. We define

$$\hat{U}_I = \sum_{j'=j} e^{i\omega_j t}\, |j'\rangle\, \langle j| \tag{B.9}$$

The new quantum state $|\psi'\rangle$ and Hamiltonian $\hat{H}'$ in the interaction picture transforms as follows

$$\begin{aligned}|\psi'\rangle &= \hat{U}_I\, |\psi\rangle \\ \hat{H}' &= \hat{U}_I \hat{H} \hat{U}_I^\dagger - i\hbar \hat{U}_I \partial_t \hat{U}_I^\dagger \\ &= (\hat{U}_I \hat{H}_a \hat{U}_I^\dagger - i\hbar \hat{U}_I \partial_t \hat{U}_I^\dagger) + \hat{U}_I \hat{H}_I \hat{U}_I^\dagger\end{aligned} \tag{B.10}$$

The $\hat{H}'$ in the interaction picture has 0 diagonal matrix elements and the off-diagonal matrix elements are given by the interaction Hamiltonian $\hat{H}'_{int}$ in the interaction picture

$$
\begin{aligned}
\hat{H}'_{int} &= \hat{U}_I \hat{H}_{int} \hat{U}_I^\dagger \\
&= -\frac{\hbar}{2} \sum_{\substack{i'>j' \\ i=i',j=j'}} \left[\frac{\boldsymbol{d}_{ij} \cdot \boldsymbol{\epsilon} \tilde{E}}{\hbar} e^{-i(\omega_f - \omega_{ij})t} \left|i'\right\rangle \left\langle j'\right| + \frac{\boldsymbol{d}_{ji} \cdot \boldsymbol{\epsilon} \tilde{E}^*}{\hbar} e^{i(\omega_f + \omega_{ji})t} \left|j'\right\rangle \left\langle i'\right| + \right. \\
&\qquad \left. \frac{\boldsymbol{d}_{ij} \cdot \boldsymbol{\epsilon} \tilde{E}^*}{\hbar} e^{i(\omega_f + \omega_{ij})t} \left|i'\right\rangle \left\langle j'\right| + \frac{\boldsymbol{d}_{ji} \cdot \boldsymbol{\epsilon} \tilde{E}}{\hbar} e^{-i(\omega_f - \omega_{ji})t} \left|j'\right\rangle \left\langle i'\right| \right]
\end{aligned}
\tag{B.11}
$$

The last two terms in the bracket of Eq. B.11 are generally ignored due to the fast oscillation $\omega_f + \omega_{ij} = \omega_f - \omega_{ji} \approx 2\omega_f$ when the electric fields couple resonantly with $|i\rangle$ and $|j\rangle$. This approximation is called "rotating wave approximation" (RWA). Using RWA, the interaction Hamiltonian is given by

$$
\begin{aligned}
\hat{H}'^{RWA}_{int} &= -\frac{\hbar}{2} \sum_{\substack{i'>j' \\ i=i',j=j'}} \left[\frac{\boldsymbol{d}_{ij} \cdot \boldsymbol{\epsilon} \tilde{E}}{\hbar} e^{-i(\omega_f - \omega_{ij})t} \left|i'\right\rangle \left\langle j'\right| + \frac{\boldsymbol{d}_{ji} \cdot \boldsymbol{\epsilon} \tilde{E}^*}{\hbar} e^{i(\omega_f - \omega_{ij})t} \left|j'\right\rangle \left\langle i'\right| \right] \\
&= -\frac{\hbar}{2} \sum_{\substack{i'>j' \\ i=i',j=j'}} \left(\Omega_{ij} e^{-i\delta_{ij}t} \left|i'\right\rangle \left\langle j'\right| + \Omega_{ji} e^{i\delta_{ij}t} \left|j'\right\rangle \left\langle i'\right| \right)
\end{aligned}
\tag{B.12}
$$

where the field detuning δ_{ij} is defined as

$$
\delta_{ij} = \omega_f - \omega_{ij} = \omega_f - (\omega_i - \omega_j) \tag{B.13}
$$

The complex Rabi frequency Ω_{ij} is defined as

$$
\begin{aligned}
\Omega_{ij} &= \frac{\boldsymbol{d}_{ij} \cdot \boldsymbol{\epsilon}\, \tilde{E}}{\hbar} \\
\Omega_{ji} &= \Omega_{ij}^* \\
&= \frac{\boldsymbol{d}_{ji} \cdot \boldsymbol{\epsilon}\, \tilde{E}^*}{\hbar}
\end{aligned}
\tag{B.14}
$$

where $\boldsymbol{d}_{ij} = \boldsymbol{d}_{ji}^*$ is used for the Hermitian operator $\hat{\boldsymbol{d}}$. Comparing Eq. B.12 and Eq. B.11, we see that in the interaction picture, the fast oscillations (at the field frequency) of the interaction Hamiltonian matrix elements are reduced to a much slower frequency (at atomic-field detuning frequency). Further, in the RWA the Hermitian property of the Hamiltonian is maintained.

In the next few paragraphs, we will introduce a second unitary transformation $\hat{U}_d$ that

brings us from the interaction picture to a "dressed atom" picture. In this picture, the residual oscillation at the field-detuning frequency δ_{ij} in the off-diagonal matrix element of the Hamiltonian can be eliminated at the cost of introducing additional diagonal terms. It needs to be pointed out that the "dressed atom" picture which we define in the following differs in spirit from that of dressed-atom states which are frequently used together with a fully quantized electromagnetic field. The dressed-atom states, in a quantized electromagnetic field, are eigenstates of the atom plus field (i.e. representation of the linear combinations of the products of atomic and quantized-field eigenstates).

In our "dressed atom" picture, the electromagnetic fields remain classical. Some authors also refer to this picture as field-interaction picture [82]. The exact form of the "dressed-atom" transformation $\hat{U}_d$ depends on the specific structure of the system and, it has a degree of freedom to choose a zero energy state.

In the Rydberg EIT system, the Rydberg atoms are excited in two steps. In the first, the probe laser couples the ground state $|1\rangle$ to the intermediate state $|2\rangle$. In the second, the coupling laser couples the state $|2\rangle$ to the Rydberg level $|3\rangle$. In this case, we have two different laser fields with two distinctive frequencies. The interaction Hamiltonian in the interaction picture is given by the following (using RWA)

$$\hat{H}_{int}^{\prime RWA} = -\frac{\hbar}{2}\left[\Omega_{21}^{prb} e^{-i\delta_{21}^{prb}t}\left|2'\right\rangle\left\langle 1'\right| + \Omega_{32}^{cpl} e^{-i\delta_{32}^{cpl}t}\left|3'\right\rangle\left\langle 2'\right| + \text{c.c.}\right] \tag{B.15}$$

We define the unitary transformation $\hat{U}_d$ which brings us from the interaction picture to the dress-state picture, as follows:

$$\hat{U}_d = \left|\tilde{1}\right\rangle\left\langle 1'\right| + e^{i\delta_{21}^{prb}t}\left|\tilde{2}\right\rangle\left\langle 2'\right| + e^{i(\delta_{32}^{cpl}+\delta_{21}^{prb})t}\left|\tilde{3}\right\rangle\left\langle 3'\right| \tag{B.16}$$

Using the transformation rule (like Eq. B.10) $\tilde{\hat{H}} = \hat{U}_d \hat{H}_{int}^{\prime RWA} \hat{U}_d^\dagger - i\hbar \hat{U}_d \partial_t \hat{U}_d^\dagger$, the total Hamiltonian in the "dressed atom" picture is

$$\tilde{H} = -\frac{\hbar}{2}\begin{bmatrix} 0 & \Omega_{prb}^* & 0 \\ \Omega_{prb} & 2\delta_{prb} & \Omega_{cpl}^* \\ 0 & \Omega_{cpl} & 2(\delta_{prb}+\delta_{cpl}) \end{bmatrix} \tag{B.17}$$

where the Rabi frequencies $\Omega_{prb/cpl}$ are defined as

$$\begin{aligned} \Omega_{prb} &= \frac{\boldsymbol{d}_{21}\cdot(\boldsymbol{\epsilon_1}\,\tilde{E}_{prb,1} + \boldsymbol{\epsilon_2}\,\tilde{E}_{prb,2})}{\hbar} \\ \Omega_{cpl} &= \frac{\boldsymbol{d}_{32}\cdot(\boldsymbol{\epsilon_1}\,\tilde{E}_{cpl,1} + \boldsymbol{\epsilon_2}\,\tilde{E}_{cpl,2})}{\hbar} \end{aligned} \tag{B.18}$$

The $\sim$ symbol reminds us that we assume a slowly varying amplitude of the electric fields

as:

$$\boldsymbol{E}(t)^{real} = \frac{1}{2}\left[(\boldsymbol{\epsilon_1}\,\tilde{E}_1(t) + \boldsymbol{\epsilon_2}\,\tilde{E}_2(t))e^{-i\omega t} + \text{c.c.}\right] \tag{B.19}$$

Also, $\boldsymbol{\epsilon}_1$ and $\boldsymbol{\epsilon}_2$ are unit vectors representing the two orthogonal polarizations perpendicular to the propagation direction $\boldsymbol{k}$. The dipole matrix element $\boldsymbol{d}_{ij}$ is defined as

$$\boldsymbol{d}_{ij} = \langle i| - e\hat{\boldsymbol{r}}\,|j\rangle \tag{B.20}$$

where $e > 0$ is the elementary charge of the electron.

APPENDIX C

Transition Dipole Moments and Rabi Frequencies

C.1 Sign conventions and Definitions

For the convenience of evaluating quantum mechanical operators, spherical tensors are often used in conjunction with traditional vectors and Cartesian tensors. Unfortunately, the sign convention and definitions are a little chaotic in the literatures and among text books. In this section, I document the important sign conventions and definitions used in this work.

Let us start with an arbitrary 3D vector $\boldsymbol{A}$ expressed in the Cartesian coordinate system $\{\boldsymbol{e}_x, \boldsymbol{e}_y, \boldsymbol{e}_z\}$:

$$\boldsymbol{A} = A_x\boldsymbol{e}_x + A_y\boldsymbol{e}_y + A_z\boldsymbol{e}_z \tag{C.1}$$

The Cartesian coordinate basis vectors $\boldsymbol{e}_x$,$\boldsymbol{e}_y$ and $\boldsymbol{e}_z$ are unit vectors and are orthogonal to each other, so the inner product of any two vectors $\boldsymbol{A}$ and $\boldsymbol{B}$ can be directly obtained as

$$\begin{aligned}\boldsymbol{A}\cdot\boldsymbol{B} &= (A_x\boldsymbol{e}_x + A_y\boldsymbol{e}_y + A_z\boldsymbol{e}_z)\cdot(B_x\boldsymbol{e}_x + B_y\boldsymbol{e}_y + B_z\boldsymbol{e}_z)\\ &= A_xB_x + A_yB_y + A_zB_z\end{aligned} \tag{C.2}$$

Next, by using the Cartesian basis vectors $\{\boldsymbol{e}_x, \boldsymbol{e}_y, \boldsymbol{e}_z\}$ let us define the "spherical basis" vectors $\{\boldsymbol{\epsilon}_1, \boldsymbol{\epsilon}_{-1}, \boldsymbol{\epsilon}_0\}$ as following:

$$\begin{aligned}\boldsymbol{\epsilon}_+ &= -(\boldsymbol{e}_x - i\boldsymbol{e}_y)/\sqrt{2}\\ \boldsymbol{\epsilon}_- &= (\boldsymbol{e}_x + i\boldsymbol{e}_y)/\sqrt{2}\\ \boldsymbol{\epsilon}_0 &= \boldsymbol{e}_z\end{aligned} \tag{C.3}$$

Just as in the Cartesian coordinate system, we can express any vector $\boldsymbol{A}$ in the "spherical basis" as $\boldsymbol{A} = A_+\boldsymbol{\epsilon}_+ + A_-\boldsymbol{\epsilon}_- + A_0\boldsymbol{\epsilon}_0$ where $\{A_+, A_-, A_0\}$ are related to $\{A_x, A_y, A_z\}$ through

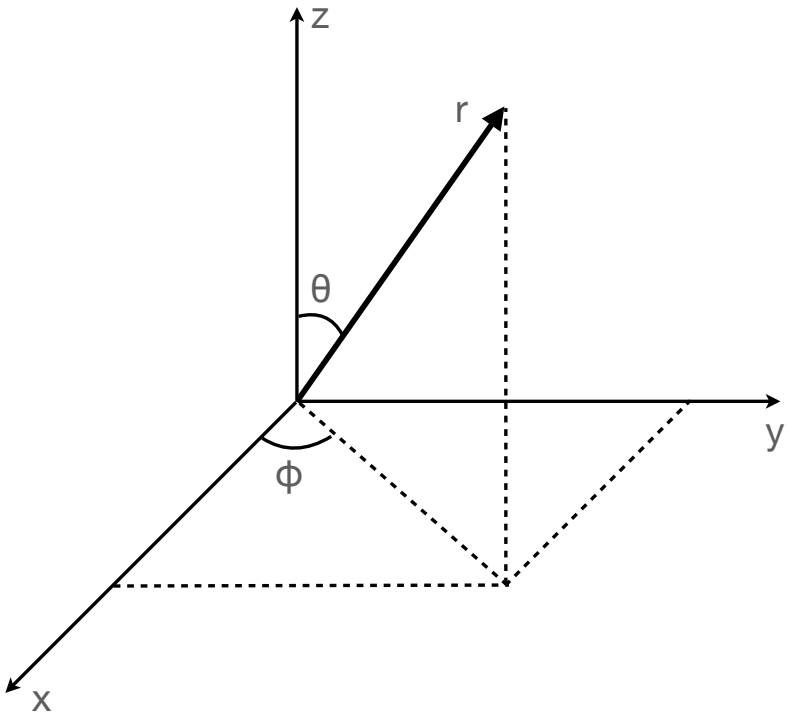

Figure C.1: vector $\boldsymbol{r}$ in Cartesian Coordinate

$$\begin{aligned} A_+ &= -(A_x + iA_y)/\sqrt{2} \\ A_- &= +(A_x - iA_y)/\sqrt{2} \\ A_0 &= A_z \end{aligned} \tag{C.4}$$

Please note the sign differences when comparing Eq. C.3 and Eq. C.4.

On the spherical basis, the inner product of any vector $\boldsymbol{A}$ and $\boldsymbol{B}$ is defined as

$$\boldsymbol{A} \cdot \boldsymbol{B} = \sum_q (-1)^q A_q B_{-q} \tag{C.5}$$

where $q = +, -, 0$. The factor $(-1)^q$ is kept in Eq. C.5 for the convenience of generalization to higher-rank tensors. A 3D vector is a rank-1 tensor. After a few lines of algebra, Eq. C.5 is consistent with Eq. C.2.

As an example, let us consider a vector $\boldsymbol{r} = x\boldsymbol{e}_x + y\boldsymbol{e}_y + z\boldsymbol{e}_z$ with amplitude r, as shown in Fig. C.1. Using Eq. C.4, the spherical components are

$$
\begin{aligned}
r_+ &= -\frac{1}{\sqrt{2}}(x+iy) = -\frac{1}{\sqrt{2}} r\sin\theta e^{i\phi} = \sqrt{\frac{4\pi}{3}} r Y_1^1(\theta,\phi) \\
r_- &= \frac{1}{\sqrt{2}}(x-iy) = \frac{1}{\sqrt{2}} r\sin\theta e^{-i\phi} = \sqrt{\frac{4\pi}{3}} r Y_1^{-1}(\theta,\phi) \\
r_0 &= z = r\cos\theta = \sqrt{\frac{4\pi}{3}} r Y_1^0(\theta,\phi)
\end{aligned}
\tag{C.6}
$$

The Euler identity and spherical harmonics (under Condon-Shortley phase conversion)[166] are used.

C.2 Matrix elements of operator $\hat{r}$

When calculating transition strength or Rabi frequencies, we ofter need to evaluate the matrix elements of the quantum operator $\hat{\boldsymbol{r}}$ using the Rydberg states as basis functions. Since the Rydberg state $|n,\ell,m\rangle$ is prepared in spatial representation as shown in Eq. 3.4, it is convenient to write the $\hat{\boldsymbol{r}}$ in spherical basis using spherical harmonics as shown in Eq. C.6. Thus, the evaluation of the matrix elements of $\hat{\boldsymbol{r}}$ boils down to evaluating the quantity of the form:

$$
\begin{aligned}
\langle n,\ell,m|\, r_q \,|n',\ell',m'\rangle &= \int r^2 \mathrm{d}r \sin\theta \mathrm{d}\theta \mathrm{d}\phi \frac{\rho_{n,\ell}}{r} \left(Y_\ell^m\right)^* \sqrt{\frac{4\pi}{3}} r Y_1^q \frac{\rho_{n',\ell'}}{r} Y_{\ell'}^{m'} \\
&= \sqrt{\frac{4\pi}{3}} \int_0^\infty \mathrm{d}r \rho_{n,\ell}\, r\, \rho_{n',\ell'} \int_\Omega \mathrm{d}\Omega \left(Y_\ell^m\right)^* Y_1^q Y_{\ell'}^{m'}
\end{aligned}
\tag{C.7}
$$

Using identities in Eq. 3.23 and Eq. 3.24, the 3-Y integral can be written in terms of Wigner-3J symbols:

$$
\begin{aligned}
&\int_\Omega \mathrm{d}\Omega \left(Y_\ell^m\right)^* Y_1^q Y_{\ell'}^{m'} \\
&= \sqrt{\frac{3}{4\pi}} (-1)^{-2\ell'+m} \sqrt{(2\ell'+1)(2\ell+1)} \begin{pmatrix} 1 & \ell' & \ell \\ 0 & 0 & 0 \end{pmatrix} \begin{pmatrix} 1 & \ell' & \ell \\ q & m' & -m \end{pmatrix}
\end{aligned}
\tag{C.8}
$$

Recall the Wigner-Ekart Theorem

$$\begin{aligned}\langle n,\ell,m|\, r_q\, |n',\ell',m'\rangle &= (-1)^{\ell-m}\begin{pmatrix} \ell & 1 & \ell' \\ -m & q & m' \end{pmatrix}\langle n,\ell|\,|r|\,|n',\ell'\rangle \\ &= (-1)^{\ell-m}\begin{pmatrix} 1 & \ell' & \ell \\ q & m' & -m \end{pmatrix}\langle n,\ell|\,|r|\,|n',\ell'\rangle\end{aligned} \tag{C.9}$$

We find that

$$\begin{aligned}&\langle n,\ell|\,|r|\,|n',\ell'\rangle \\ &= (-1)^{\ell}\sqrt{(2\ell'+1)(2\ell+1)}\begin{pmatrix} 1 & \ell' & \ell \\ 0 & 0 & 0 \end{pmatrix}\int_0^\infty \mathrm{d}r\rho_{n,\ell}\, r\, \rho_{n',\ell'}\end{aligned} \tag{C.10}$$

APPENDIX D

Glass lapping procedures

D.1 Preparation: Glue to the workpiece to carrier glass wafer

• beeswax is used as Glue

• EcoClear is used as a solvent for the wax to remove excess wax

· EcoClear is product by Logitech Ltd. it is a food grade distilled essential oil. See Fig. D.3

• Acetone and then IPA can be used to remove the EcoClear.

• beeswax is heated above its melting temperature to ensure a low viscosity (80 °C to 100 °C is enough, at 150 °C the beeswax start to evaporate and has low viscosity).

• The workpiece (glass) is heated to about two 80 °C to 100 °C to ensure adequate wetting of the beeswax.

• The substrate (on which the workpiece is glued) is recommended to be heated a little below the melting temperate (65 °C) of the beeswax. 40°C to 50 °C is good enough. A warm substrate ensures a longer period of time for the wax and workpiece to settle. The whole piece should then be cooled for a minute or two, and during this time, a force should be applied to ensure a good contact between the workpiece and substrate; excess wax can be squeezed out during this time. A sudden contact of hot wax and room temperature substrate causes the wax to harden too quickly, making the bond brittle.

• Carefully remove excess beeswax on the surface that needs to be lapped later. A microscope check is recommended. Small residual wax tends to attract lapping particles (calcified aluminum oxide) which stick to the surface. These particles may result in scratches across the surface.

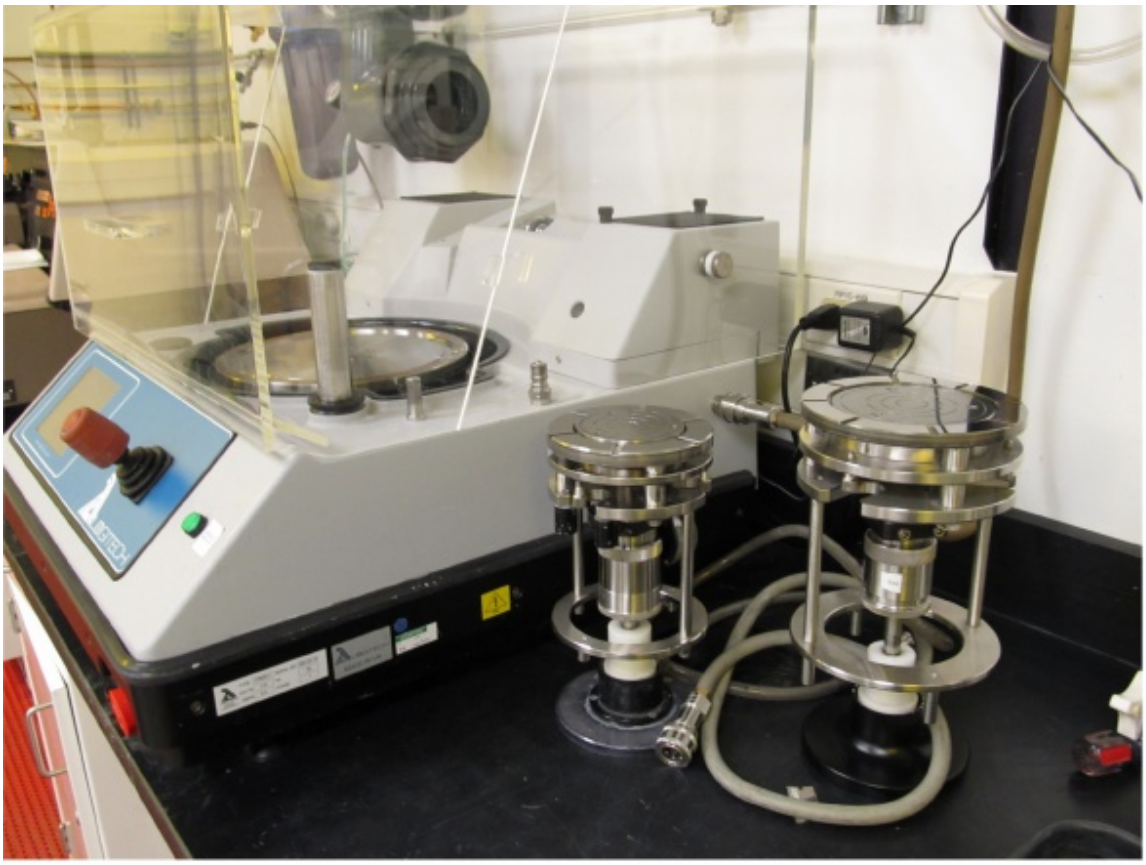

Figure D.1: Lapper at the LNF used for this project

D.2 Lapping procedures

•These lapping procedures were developed with special consideration for the Logitech PM5 Lapper (See Fig. D.1) available at the LNF.

•Chemicals used for lapping and cleaning

· Start with 3 micron, then 1 micron, then CMP(Chemical Mechanical Polishing).

· The 3-micron and 1-micron slurry contains calcified aluminum oxide particles suspended in DI water. (ingredient ratio unknown).

· CMP uses a mixture of potassium hydroxide (KOH), colloidal silicon oxide, and DI water as a slurry (see Fig. D.3).

· 5% of ammonia hydroxide solution is recommended to remove residual lapping particles stuck to the surfaces. Commercial chemicals are available for this purpose (see Fig. D.4).

• Dummy Pieces

·Purpose: distributing weight evenly and ensureing a gentle initial start for the workpiece

·At least three dummy pieces are recommended. They should be a little bit higher than the workpiece (0.1mm or more is enough) and be relatively flat to ensure a good starting conditions for lapping. A height indicator check and visual check are recommended before assembling the whole piece onto the lapper jig. The dummy pieces will start to be polished first and when they reach the same height as the workpiece, all pieces start to be polished. This ensures a gentle start on the workpieces and distributes the total weight which are applied during the lapping process

• Lapping vertical force and lapping plate rotation speed and timing

· The larger vertical force and higher rotation speed of the lapping plate is, the faster the lapping rate is. Higher lapping rate risks breaking the non-flat structure and chipping off on the edges of the glass tubes.

· The lapping plate rotation speed is 5 15 rpm. The more slurry, the higher the speed can be set and the more horizontal drag force is applied

· The lapping jig arm is recommended to be set in sweep mode for stages of 1micron and CMP to remove excess or used slurry from the plate and ensures a flatter less scratched finish.

· Three-micron slurry: start with 0.1kg/pieces. When the working pieces start to get lapped together with the dummy pieces, adjust the vertical force so that the height reduces at about 1micron per 5 10 seconds. The rate of taking material off should be low enough in order to minimize the risk of chipping off on the edges of the tubes. Also, counter-intuitively, the more forces applied, the finish surfaces tend to be more warped. This can be checked after 1-micron stage using microscope with DIC mode (differential interference contrast). See results in Fig. D.5. If the indicator reading does not change at this speed, increase the vertical force or rotation speed of the lapping plate. Monitor the indicator reading at this stage and record the final number. Check with height gauge measurement after this stage. Once all the pieces start to get lapped and get close to the target length, double check the pressure, a 10 gram/mm^2 or less is recommended for finishing off.

· One-micron slurry: approximately 0.1 kg (or less)per lapping pieces for approximately 30 min.

· CMP (oxide slurry): At least 10 gram/mm^2 pressure is required at this stage. 12 to 15 gram/mm^2 is recommended for 10 to 20 min.

• Flipping the pieces over

· When the first surface is done by CMP, clean the surface well to get rid of the residual slurries. The work pieces are then ready to be flipped over.

· Prepare and clean a new carrier glass wafer carefully, this plate will directly contact the polished surface (with less than 10 micron thick of wax in between).

· During the process, pay attention and keep track of what surfaces need to be polished. Sometimes this can be confusing (e.g. when the glass is dipped into a clear solvent, the refraction index blends them together, obscuring where the piece is in the solution).

· Use a plate on the top to distribute the force when the glue is hardening. Since the the bottom surfaces has been lapped flat, as long as the viscosity of the wax is low enough, all pieces can be pressed down and have a flat contact at the bottom even though the top surfaces of the pieces may not be flat (when pressing on the top).

• Intermediate check and clean

· After the initial lapping of three-micron, a height gauge check is recommended to establish the initial workpiece height (they all should be the same height within 10 microns, including the dummy piece). The amount of material needs to be taken off should be estimated at this point.

· After the 3-micron stage, a cleanning process is recommended to remove residual lapping particles stuck on the surface by electrical static force. These residual particles tend to cause scratches in the later lapping stage with finer particles. An approximately 5% of Ammonium Hydroxide solution is used. Ultra sonic bath is recommended or all automatic wafer cleaning machine with a brush and ultrasonic bath (e.g. SSEC wafer and Mask Cleaner) can be used too.

· Do not dry the work piece surface before the wash!

· A microscope check (10X to 50X) is recommended to ensure no residual lapping particle remains. The lapping particles appear shinier than the glass piece under a microscope. Also, move the microscope objective to different spots on the sample surface, and record how much z distance must be adjusted to refocus on the sample surface. This gives a sense of how much tilt or warp exists on the surface macroscopically.

· After the 1-micron stage and before the CMP, a microscope check can be performed. Residual blips appear on the surfaces (see Fig. D.6; the image is taken with an Olympus BX51 microscope using DIC to show blips sticking out of the surface). These are glass materials that have not been removed. Due to micro stress in the glass, the surface glass comes off in chunks (a few microns large), so blips are left on the surface. Chemical lapping is needed to remove them uniformly.

• Final clean and surface smoothness/roughness measure

· At the end of the CMP stage, before stopping the rotation of the lapping plate, stop the slurry first and then pour DI water on the plate to reduce the lapping particle density. This serves as a prewash while the work pieces are still rubbing against the lapping cloth.

· Bring the sample to ammonium hydroxide ultrasonic wash immediately after being taken off the lapper. DONT LET IT DRY !

· If the SSEC wafer and mask cleaner are used, then rinse the whole piece (carrier glass wafer, mounting jigs, workplace, etc) with DI water. Make sure the residuals in the grooves of the mounting jigs are washed.

· Use a nitrogen blowing gun to gently blowing away the DI water on top of the workpiece surfaces. Try not to splash the water droplets from other places on the carrier glass wafer on to the workpiece surfaces.

· TRY NOT to wipe the surface with any materials any more.

· A quick 100X microscope check can be done. It should look smooth under DIC mode (i.e. when the prism is turned, the color of the imaged surface should change uniformly.)

· Now, the sample is ready for an AFM check.

D.3 De-bonding workpieces from the carrier glass disc and cleanning off the wax

• ECO Clear solution is used (see Fig. D.3)

• Heat the glass carrier disc, workpieces, and beeswax to about 120 °C. The wax will start to evaporate a little bit, and fumes will be visible. At this point, the viscosity of the wax is very low, so use a tweezer to hold the workpiece and lift it off the glass plate. as the work piece cools, the wax dips and stay at the hot glass disc. The surface tension of the wax will help at this point.

• Dip the whole workpiece into the Ecoclear solvent, which can also be heated up to about 60 °C. Let it soak for a minute. Then, bring the workpiece with Ecoclear solvent on the surface to an aluminum petri dish and heat them together. The oil-based Ecoclear will start to evaporate, and wax or Ecoclear fluid will stick onto the aluminum petri dish. Use the surface tension of the liquid to extract the wax from inside the tubes as much as possible. Then, soak the workpiece again in the Ecoclear solvent (cold, never heated), reheat the workpiece, and repeat the cleaning.

• When there is no visual residual wax left on the workpiece, it is ready for a rinse of Acetone, IPA, and DI water.

• The work pieces are now ready to be stored in a gel box.

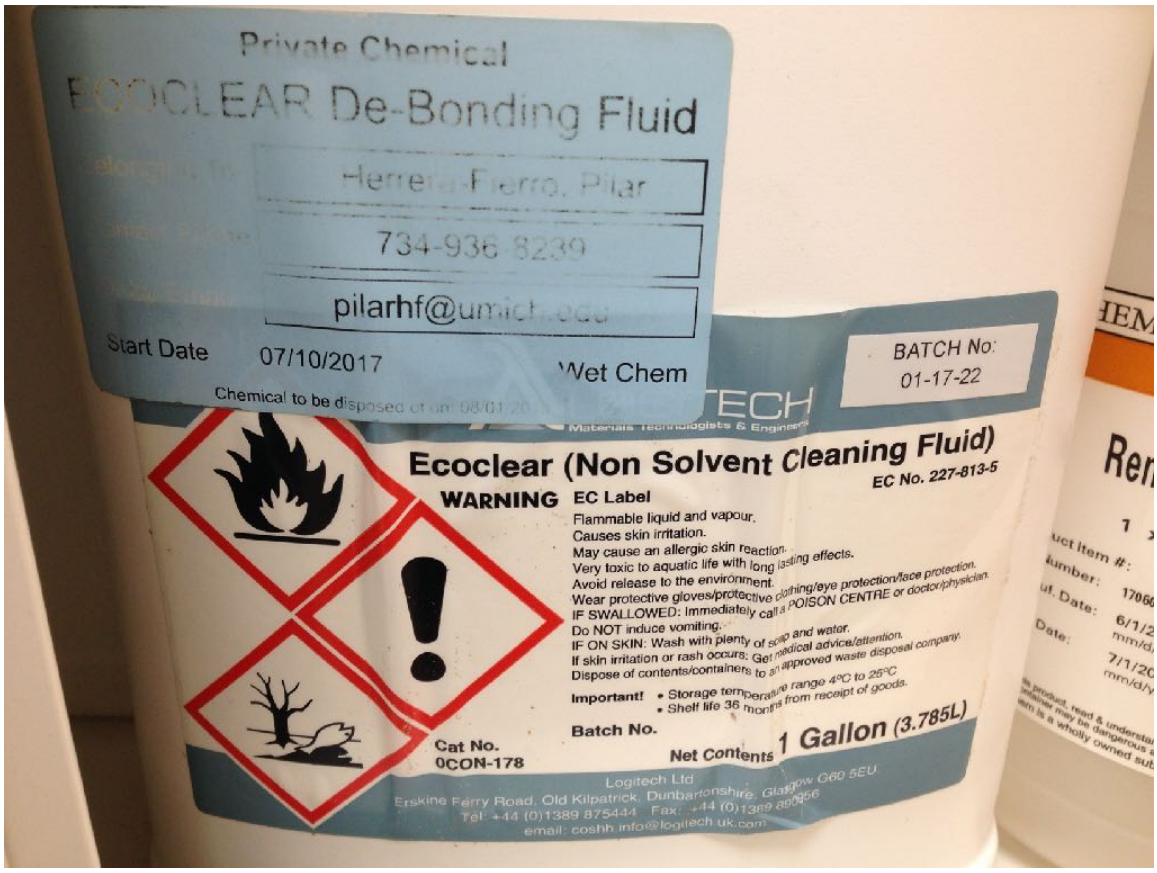

Figure D.2: Ecolear De-Bonding Fluid for removing the beeswax.

Figure D.3: Polishing slurry used in the CMP lapping stage.

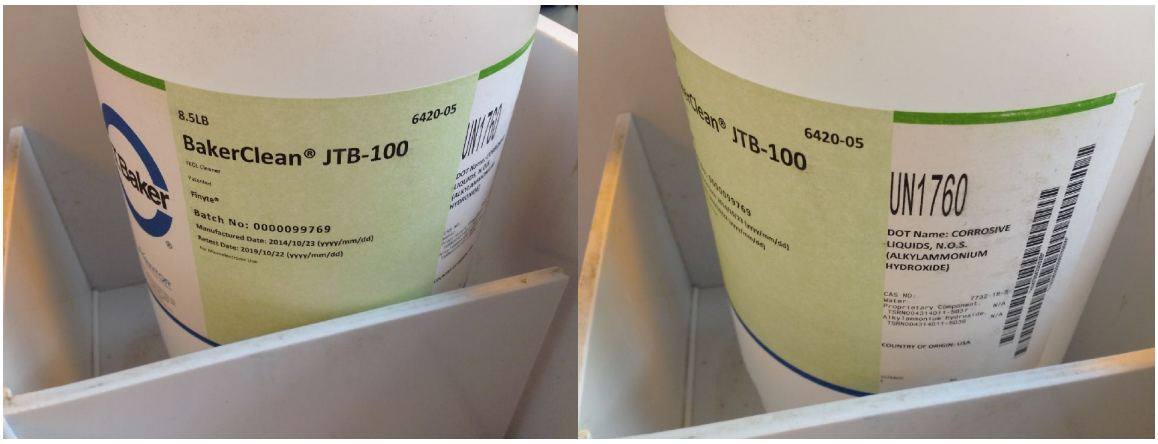

Figure D.4: Cleaning chemicals used to remove the lapping slurry from the working pieces.

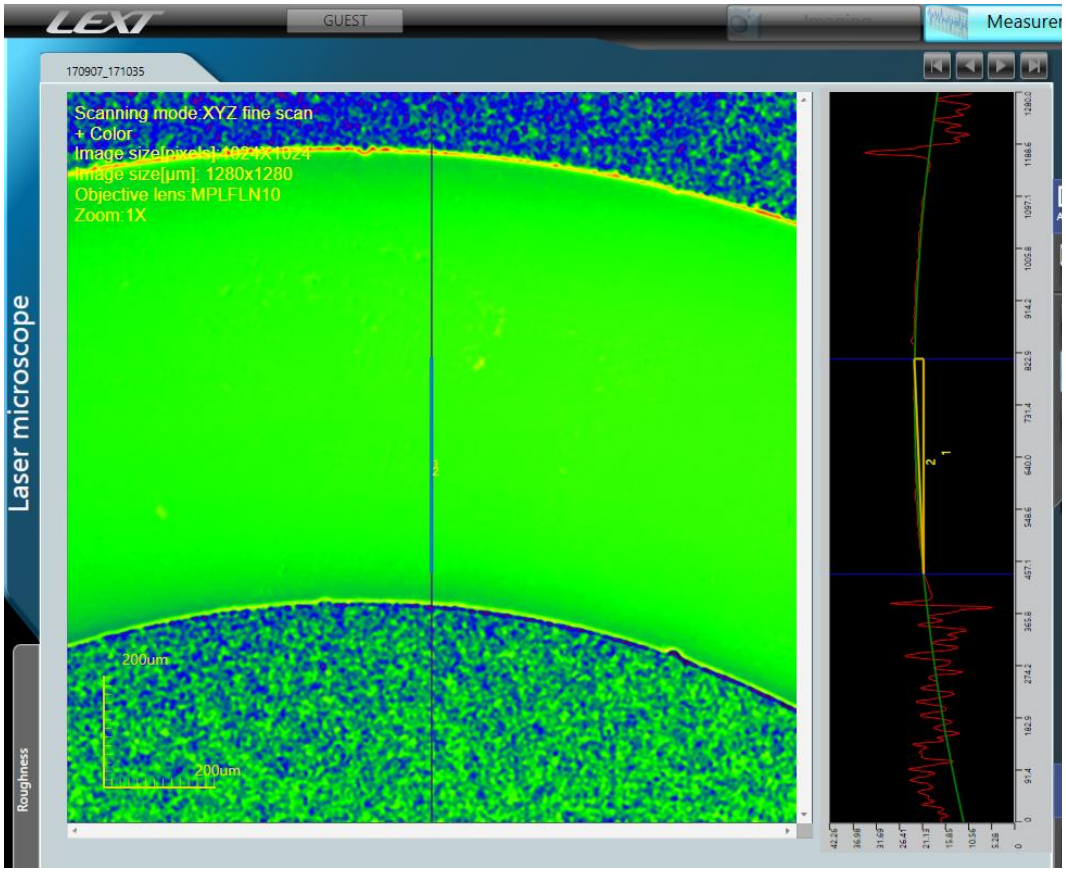

Figure D.5: Microscopes with DIC capability can be used to check the potential warping of the lapping surface after finishing the1micron lapping stage.

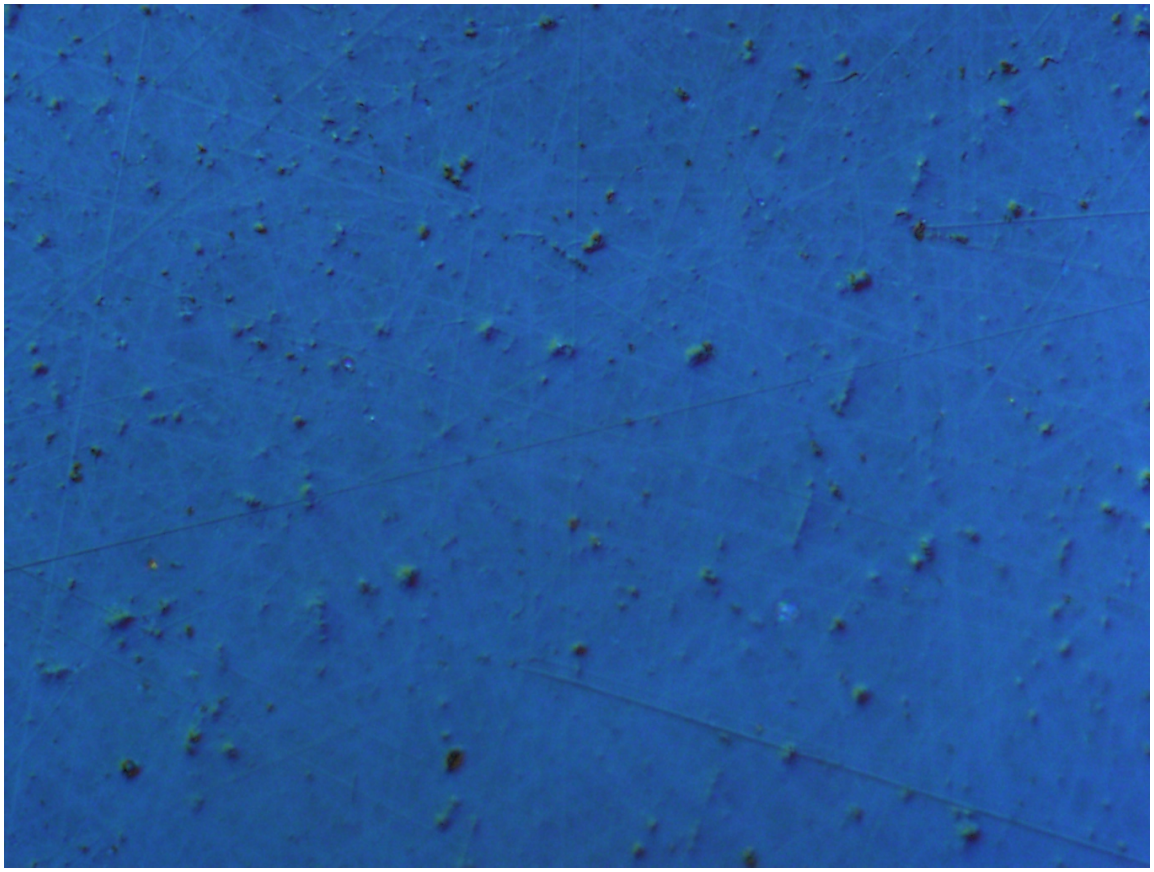

Figure D.6: Residual glass pits are presents due to the uneven stress of the glass after the last mechanical lapping stage. Chemical Mechanical Lapping is needed to uniformly remove them.

APPENDIX E

Application Potentials in the Electron Microscopy Industry

In this chapter, I summarize the application potentials of Rydberg atoms as atomic sensors for electromagnetic-field sensing in the context of manufacturing electron beam microscopes for chip inspections in the semiconductor industry. Based on my internship experiences at ASML HMI, I focus on the challenges and requirements in large-scale industrial production.

As nanofabrication technologies advance, more resources are invested in the chip-making and inspection sector of the semiconductor industry. One verification and inspection method common in this industry is electron beam micro-spectroscopy. Utilizing the short de Broglie wavelength of high-energy electrons in a well-controlled electron beam, engineers can detect defects and irregularities in the nanofabricated transistors on the surfaces of silicon wafers. The fundamentals of this imaging process are governed by the physics of electron scattering. Just like a scanning electron microscope (SEM) in a laboratory environment, a prior for high-resolution spectroscopy images is a high-quality electron beam. This level of beam-shaping and control is achieved using sophisticated electromagnetic fields. A clear, detailed understanding of the electromagnetic environments where the electron beam travels is thus important. The high sensitivity of Rydberg atoms to external RF and static electromagnetic fields makes them good tools for such jobs.

Thanks to advanced computer simulation technologies, complex manipulation and control fields can be designed and studied in detail during the R&D phases of products. The challenges are design verification and real-time monitoring and feedback controls. In many cases, an electron beam must be shaped and focused within a few microns by compactly designed electrodes and coils. It is difficult to verify the field distributions in such a small space using only man-made pickup coils or antennas.

Rydberg atoms come in handy in these scenarios. In addition, the optical-readout method of EIT allows laser beams to be tightly focused, which ensures high spatial reso-

lution. Another advantage people often neglect is that measurements and detections do not need to be performed locally as long as the atoms can fly by. Modern industrial machines are highly complicated equipment with many supporting and servo modules clustered together. A remote sensing capability (hundreds of cm away) using laser beams greatly simplifies the verification procedures. Only peripheral modules (e.g., lasers and photo diodes) are needed, and they do not compromise or alter the core design of the device under testing.

In addition to the verification needs of the R&D phases of new products, there is also great demand for real-time monitoring and feedback control during the running phases of machines. The best approaches are the so-called *in situ* methods, which utilize the electron beams themselves as sensors. However, a certain amount of independent, third-party measurements are also valuable. By considering these types of applications, the shortcomings of using Rydberg atoms as field sensors are clear. The first technical challenge is the lack of fast, real-time methods of analyzing the atomic spectrum. In scientific and research settings, this is done through *ab initio* calculations of underling quantum-mechanical interaction Hamiltonians. Unless more advanced algorithms are developed, these scientific calculations are too costly. In other words, some engineering simplifications (on the levels of both software and hardware) or semi-classical approaches are needed to reduce the complexity of the quantum physics of atoms while preserving accuracy and sensitivity. After all, the point is that engineers do not need to understand the profound importance of the gauge-invariant symmetry of electromagnetism to analyze the circuitry that lights up an LED.

BIBLIOGRAPHY

[1] Sibalic N and Adams C S 2018 Rydberg physics *Rydberg Physics* 2399-2891 (IOP Publishing) pp 1–1 to 1–27 ISBN 978-0-7503-1635-4 URL http://dx.doi.org/10.1088/978-0-7503-1635-4ch1

[2] Xiao M, Li Y q, Jin S z and Gea-Banacloche J 1995 *Phys. Rev. Lett.* **74**(5) 666–669 URL https://link.aps.org/doi/10.1103/PhysRevLett.74.666

[3] Mohapatra A K, Jackson T R and Adams C S 2007 *Phys. Rev. Lett.* **98**(11) 113003 URL https://link.aps.org/doi/10.1103/PhysRevLett.98.113003

[4] Gavryusev V, Signoles A, Ferreira-Cao M, Zürn G, Hofmann C S, Günter G, Schempp H, de Saint-Vincent M R, Whitlock S and Weidemüller M 2016 *Journal of Physics B: Atomic, Molecular and Optical Physics* **49** 164002

[5] Weatherill K J, Pritchard J D, Abel R P, Bason M G, Mohapatra A K and Adams C S 2008 *Journal of Physics B: Atomic, Molecular and Optical Physics* **41** 201002

[6] Tauschinsky A, Newell R, van Linden van den Heuvell H B and Spreeuw R J C 2013 *Phys. Rev. A* **87**(4) 042522 URL https://link.aps.org/doi/10.1103/PhysRevA.87.042522

[7] Chow C M, Ross A M, Kim D, Gammon D, Bracker A S, Sham L J and Steel D G 2016 *Phys. Rev. Lett.* **117**(7) 077403 URL https://link.aps.org/doi/10.1103/PhysRevLett.117.077403

[8] Phillips D F, Fleischhauer A, Mair A, Walsworth R L and Lukin M D 2001 *Phys. Rev. Lett.* **86**(5) 783–786 URL https://link.aps.org/doi/10.1103/PhysRevLett.86.783

[9] Saffman M 2019 *Nature* **567** 468–470

[10] Levine H, Keesling A, Omran A, Bernien H, Schwartz S, Zibrov A S, Endres M, Greiner M, Vuletić V and Lukin M D 2018 *Phys. Rev. Lett.* **121**(12) 123603 URL https://link.aps.org/doi/10.1103/PhysRevLett.121.123603

[11] Urban E, Johnson T A, Henage T, Isenhower L, Yavuz D D, Walker T G and Saffman M 2009 *Nature Physics* **5** 110–114

[12] Wade C G, Marcuzzi M, Levi E, Kondo J M, Lesanovsky I, Adams C S and Weatherill K J 2018 *Nature Communications* **9** 3567 (7 pp.)

[13] Chen Z, Lim H M, Huang C, Dumke R and Lan S Y 2020 *Phys. Rev. Lett.* **124**(9) 093202 URL https://link.aps.org/doi/10.1103/PhysRevLett.124.093202

[14] Holloway C L, Gordon J A, Jefferts S, Schwarzkopf A, Anderson D A, Miller S A, Thaicharoen N and Raithel G 2014 *IEEE Transactions on Antennas and Propagation* **62** 6169–6182

[15] Jing M, Hu Y, Ma J, Zhang H, Zhang L, Xiao L and Jia S 2020 *Nature Physics* **16** 911–915

[16] Zentile M A, Whiting D J, Keaveney J, Adams C S and Hughes I G 2015 *Optics Letters* **40** 2000–2003

[17] Siddons P, Bell N C, Cai Y, Adams C S and Hughes I G 2009 *Nature Photonics* **3** 225–229

[18] Dawes A M C, Illing L, Clark S M and Gauthier D J 2005 *Science* **308** 672–674 ISSN 0036-8075 URL https://science.sciencemag.org/content/308/5722/672

[19] Gard B T, Jacobs K, McDermott R and Saffman M 2017 *Phys. Rev. A* **96**(1) 013833 URL https://link.aps.org/doi/10.1103/PhysRevA.96.013833

[20] Löw R and Pfau T 2009 *Nature Photonics* **3** 197–199

[21] Cirac J I, Zoller P, Kimble H J and Mabuchi H 1997 *Physical Review Letters* **78** 3221–3224

[22] Höckel D and Benson O 2010 *Phys. Rev. Lett.* **105**(15) 153605 URL https://link.aps.org/doi/10.1103/PhysRevLett.105.153605

[23] van der Wal C H, Eisaman M D, André A, Walsworth R L, Phillips D F, Zibrov A S and Lukin M D 2003 *Science* **301** 196–200 ISSN 0036-8075 URL https://science.sciencemag.org/content/301/5630/196

[24] Monroe C, Raymer M G and Taylor J 2019 *Science (New York, N.Y.)* **364** 440–442

[25] Seltzer S J 2008 *Developments in alkali -metal atomic magnetometry* Ph.D. thesis URL https://proxy.lib.umich.edu/login?url=https://www.proquest.com/dissertations-theses/developments-alkali-metal-atomic-magnetometry/docview/275671021/se-2?accountid=14667

[26] Savukov I M, Seltzer S J, Romalis M V and Sauer K L 2005 *Phys. Rev. Lett.* **95**(6) 063004 URL https://link.aps.org/doi/10.1103/PhysRevLett.95.063004

[27] Kominis I K, Kornack T W, Allred J C and Romalis M V 2003 *Nature* **422** 596–599

[28] Fleischhauer M, Matsko A B and Scully M O 2000 *Phys. Rev. A* **62**(1) 013808 URL https://link.aps.org/doi/10.1103/PhysRevA.62.013808

[29] Alexandrov E B, Balabas M V, Vershovski A K and Pazgalev A S 2004 *Technical Physics* **49** 779–783

[30] Sedlacek J A, Schwettmann A, Kübler H, Löw R, Pfau T and Shaffer J P 2012 *Nature Physics* **8** 819–824

[31] Fan H, Kumar S, Sedlacek J, Kubler H, Karimkashi S and Shaffer J 2015/10/28 *Journal of Physics B: Atomic, Molecular and Optical Physics* **48** 202001 (16 pp.) – ISSN 0953-4075 URL http://dx.doi.org/10.1088/0953-4075/48/20/202001

[32] Simons M, Kautz M, Holloway C, Anderson D, Raithel G, Stack D, St John M and Su W 2018/05/28 *Journal of Applied Physics* **123** 203105 (12 pp.) – ISSN 0021-8979 URL http://dx.doi.org/10.1063/1.5020173

[33] Anderson D A, Sapiro R E and Raithel G 2020 *IEEE Aerospace and Electronic Systems Magazine* **35** 48–56

[34] Boller K J, Imamoğlu A and Harris S E 1991 *Phys. Rev. Lett.* **66**(20) 2593–2596 URL https://link.aps.org/doi/10.1103/PhysRevLett.66.2593

[35] Fleischhauer M, Imamoglu A and Marangos J P 2005 *Rev. Mod. Phys.* **77**(2) 633–673 URL https://link.aps.org/doi/10.1103/RevModPhys.77.633

[36] Urvoy A, Carr C, Ritter R, Adams C S, Weatherill K J and L"ow R 2013 *Journal of Physics B: Atomic, Molecular and Optical Physics* **46** 245001

[37] Hohensee M A 2009 Testing fundamental lorentz symmetries of light

[38] Whiting D J, Mathew R S, Keaveney J, Adams C S and Hughes I G 2018 *Journal of Modern Optics* **65** 713–722

[39] Sevincli S, Ates C, Pohl T, Schempp H, Hofmann C S, Gunter G, Amthor T, Weidemuller M, Pritchard J D, Maxwell D, Gauguet A, Weatherill K J, Jones M P A and Adams C S 2011 *Journal of Physics B: Atomic, Molecular and Optical Physics* **44** 184018

[40] Fan H, Kumar S, Sedlacek J, Kübler H, Karimkashi S and Shaffer J P 2015 *Journal of Physics B: Atomic, Molecular and Optical Physics* **48** 202001

[41] Sedlacek J A, Schwettmann A, Kübler H, Löw R, Pfau T and Shaffer J P 2012 *Nature Physics* **8** 819–824

[42] Wade C G, ibali N, De Melo N R, Kondo J M, Adams C S and Weatherill K J 2017 *Nature Photonics* **11** 40–43

[43] Downes L A, MacKellar A R, Whiting D J, Bourgenot C, Adams C S and Weatherill K J 2019 *arXiv:1903.01308 [physics.atom-ph]*

[44] Saffman M and Walker T G 2002 *Physical Review A - Atomic, Molecular, and Optical Physics* **66** 4

[45] Ripka F, Kübler H, Löw R and Pfau T 2018 *Science* **362** 446–449

[46] Busche H, Huillery P, Ball S W, Ilieva T, Jones M P A and Adams C S 2017 *Nature Physics* **13** 655–8

[47] Tiarks D, Schmidt-Eberle S, Stolz T, Rempe G and Dürr S 2019 *Nature Physics* **15** 124–126

[48] Saffman M, Walker T G and Mølmer K 2010 *Reviews of Modern Physics* **82** 2313–2363

[49] Adams C, Pritchard J and Shaffer J 2020 *J. Phys. B, At. Mol. Opt. Phys.* **53** 012002

[50] Pritchard J D, Maxwell D, Gauguet A, Weatherill K J, Jones M P A and Adams C S 2010 *Phys. Rev. Lett.* **105**(19) 193603 URL https://link.aps.org/doi/10.1103/PhysRevLett.105.193603

[51] Robicheaux F, Booth D W and Saffman M 2018 *Phys. Rev. A* **97**(2) 022508 URL https://link.aps.org/doi/10.1103/PhysRevA.97.022508

[52] Peyrot T, Sortais Y R P, Browaeys A, Sargsyan A, Sarkisyan D, Keaveney J, Hughes I G and Adams C S 2018 *Phys. Rev. Lett.* **120**(24) 243401 URL https://link.aps.org/doi/10.1103/PhysRevLett.120.243401

[53] Knappe S, Wynands R, Kitching J, Robinson H G and Hollberg L 2001 *J. Opt. Soc. Am. B* **18** 1545–1553 URL http://josab.osa.org/abstract.cfm?URI=josab-18-11-1545

[54] Cox K, Yudin V I, Taichenachev A V, Novikova I and Mikhailov E E 2011 *Phys. Rev. A* **83**(1) 015801 URL https://link.aps.org/doi/10.1103/PhysRevA.83.015801

[55] Yudin V I, Taichenachev A V, Dudin Y O, Velichansky V L, Zibrov A S and Zibrov S A 2010 *Phys. Rev. A* **82**(3) 033807 URL https://link.aps.org/doi/10.1103/PhysRevA.82.033807

[56] Theodosiou C E 1984 *Phys. Rev. A* **30**(6) 2881–2909 URL https://link.aps.org/doi/10.1103/PhysRevA.30.2881

[57] Beterov I I, Ryabtsev I I, Tretyakov D B and Entin V M 2009 *Phys. Rev. A* **79**(5) 052504 URL https://link.aps.org/doi/10.1103/PhysRevA.79.052504

[58] Li W, Mourachko I, Noel M W and Gallagher T F 2003 *Phys. Rev. A* **67**(5) 052502 URL https://link.aps.org/doi/10.1103/PhysRevA.67.052502

[59] Mack M, Karlewski F, Hattermann H, Höckh S, Jessen F, Cano D and Fortágh J 2011 *Phys. Rev. A* **83**(5) 052515 URL https://link.aps.org/doi/10.1103/PhysRevA.83.052515

[60] Han J, Jamil Y, Norum D V L, Tanner P J and Gallagher T F 2006 *Phys. Rev. A* **74**(5) 054502 URL https://link.aps.org/doi/10.1103/PhysRevA.74.054502

[61] Seaton M J 1958 *Monthly Notices of the Royal Astronomical Society* **118** 504–518 ISSN 0035-8711 (*Preprint* https://academic.oup.com/mnras/article-pdf/118/5/504/9404738/mnras118-0504.pdf) URL https://doi.org/10.1093/mnras/118.5.504

[62] Drake G W F and Swainson R A 1991 *Phys. Rev. A* **44**(9) 5448–5459 URL https://link.aps.org/doi/10.1103/PhysRevA.44.5448

[63] Gallagher T F 2005 *Rydberg Atoms* vol 3 (Cambridge University Press)

[64] Zimmerman M L, Littman M G, Kash M M and Kleppner D 1979 **20** 2251–2275

[65] Grimmel J, Mack M, Karlewski F, Jessen F, Reinschmidt M, Sandor N and Fortagh J 2015 *New Journal of Physics* **17** 053005 (8 pp.) – ISSN 1367-2630 URL http://dx.doi.org/10.1088/1367-2630/17/5/053005

[66] Jenkins F A and Segrè E 1939 *Phys. Rev.* **55**(1) 52–58 URL https://link.aps.org/doi/10.1103/PhysRev.55.52

[67] Jensen R V 1992 *Nature* **355** 311–318

[68] Friedrich H 2006 *Theoretical atomic physics* vol 3 (Springer)

[69] Seaton M J 1983 *Reports on Progress in Physics* **46** 167–257 URL https://doi.org/10.1088%2F0034-4885%2F46%2F2%2F002

[70] Johnson W R and Cheng K T 1979 *Journal of Physics B: Atomic and Molecular Physics* **12** 863–879 URL https://doi.org/10.1088%2F0022-3700%2F12%2F6%2F006

[71] Weber S, Tresp C, Menke H, Urvoy A, Firstenberg O, Büchler H P and Hofferberth S 2017 *Journal of Physics B: Atomic, Molecular and Optical Physics* **50** 133001 URL https://doi.org/10.1088%2F1361-6455%2Faa743a

[72] Numerov B V 1923 *Trudy Glavnoi rossiiskoi astrofizicheskoi observatorii ; t. 2* **2** 188–288

[73] Jackson J 1924 *Monthly Notices of the Royal Astronomical Society* **84** 602–607 ISSN 0035-8711 (*Preprint* https://academic.oup.com/mnras/article-pdf/84/8/602/3661232/mnras84-0602.pdf) URL https://doi.org/10.1093/mnras/84.8.602

[74] Marinescu M, Sadeghpour H R and Dalgarno A 1994 *Phys. Rev. A* **49**(2) 982–988 URL https://link.aps.org/doi/10.1103/PhysRevA.49.982

[75] Sanayei A, Schopohl N, Grimmel J, Mack M, Karlewski F and Fortágh J 2015 *Phys. Rev. A* **91**(3) 032509 URL https://link.aps.org/doi/10.1103/PhysRevA.91.032509

[76] Zimmerman M L, Littman M G, Kash M M and Kleppner D 1979 *Phys. Rev. A* **20**(6) 2251–2275 URL https://link.aps.org/doi/10.1103/PhysRevA.20.2251

[77] Racah G 1942 *Phys. Rev.* **62**(9-10) 438–462 URL https://link.aps.org/doi/10.1103/PhysRev.62.438

[78] Schulten K and Gordon R G 1974 *Journal of Mathematical Physics* **16** 1961–1970 cited By :121 URL www.scopus.com

[79] Luscombe J H and Luban M 1998 *Phys. Rev. E* **57**(6) 7274–7277 URL https://link.aps.org/doi/10.1103/PhysRevE.57.7274

[80] Schultert K and Gordon R G 1974 *Journal of Mathematical Physics* **16** 1971–1988 cited By :117 URL www.scopus.com

[81] Berman P R and Salomaa R 1982 *Phys. Rev. A* **25**(5) 2667–2692 URL https://link.aps.org/doi/10.1103/PhysRevA.25.2667

[82] Berman P R and Malinovsky V S 2011 *Principles of Laser Spectroscopy and Quantum Optics* (Princeton University Press)

[83] Bao S, Zhang H, Zhou J, Zhang L, Zhao J, Xiao L and Jia S 2016 *Phys. Rev. A* **94**(4) 043822 URL https://link.aps.org/doi/10.1103/PhysRevA.94.043822

[84] Whiting D J, Keaveney J, Adams C S and Hughes I G 2016 *Phys. Rev. A* **93**(4) 043854 URL https://link.aps.org/doi/10.1103/PhysRevA.93.043854

[85] Whiting D J, Šibalić N, Keaveney J, Adams C S and Hughes I G 2017 *Phys. Rev. Lett.* **118**(25) 253601 URL https://link.aps.org/doi/10.1103/PhysRevLett.118.253601

[86] Tanasittikosol M, Carr C, Adams C S and Weatherill K J 2012 *Phys. Rev. A* **85**(3) 033830 URL https://link.aps.org/doi/10.1103/PhysRevA.85.033830

[87] DeSalvo B J, Aman J A, Gaul C, Pohl T, Yoshida S, Burgdörfer J, Hazzard K R A, Dunning F B and Killian T C 2016 *Phys. Rev. A* **93**(2) 022709 URL https://link.aps.org/doi/10.1103/PhysRevA.93.022709

[88] Zhang H, Zhang L, Wang L, Bao S, Zhao J, Jia S and Raithel G 2014 *Phys. Rev. A* **90**(4) 043849 URL https://link.aps.org/doi/10.1103/PhysRevA.90.043849

[89] Paradis E, Zigo S, Hu K Z and Raithel G 2012 *Phys. Rev. A* **86**(2) 023416 URL https://link.aps.org/doi/10.1103/PhysRevA.86.023416

[90] Zhang L, Bao S, Zhang H, Raithel G, Zhao J, Xiao L and Jia S 2018 *Opt. Express* **26** 29931–29944 URL http://www.opticsexpress.org/abstract.cfm?URI=oe-26-23-29931

[91] Paradis E, Zigo S and Raithel G 2013 *Phys, Rev. A* **87** URL http://dx.doi.org/10.1103/PhysRevA.87.012505

[92] Iu C h, Welch G R, Kash M M, Kleppner D, Delande D and Gay J C 1991 *Phys. Rev. Lett.* **66**(2) 145–148 URL https://link.aps.org/doi/10.1103/PhysRevLett.66.145

[93] Liew L A, Knappe S, Moreland J, Robinson H, Hollberg L and Kitching J 2004 *Applied Physics Letters* **84** 2694–2696

[94] Daschner R, Ritter R, Kübler H, Frühauf N, Kurz E, Löw R and Pfau T 2012 *Optics Letters* **37** 2271–2273

[95] Simons M T, Gordon J A and Holloway C L 2018 *Applied Optics* **57** 6456–6460

[96] Peyrot T, Beurthe C H, Coumar S, Roulliay M, Perronet K, Bonnay P, Adams C S, Browaeys A and Sortais Y R P 2019 *Optics Letters* **44** 1940–1943

[97] Limes ME Sheng D R M 2019 *Phys. Rev. Lett.* **120** 033401

[98] Phillips D F, Fleischhauer A, Mair A, Walsworth R L and Lukin M D 2001 *Physical Review Letters* **86** 783–786

[99] Mohapatra A K, Jackson T R and Adams C S 2007 *Physical Review Letters* **98** 113003

[100] Kumar S, Fan H, Kübler H, Jahangiri A J and Shaffer J P 2017 *Optics Express* **25** 8625–8637

[101] Whiting D J, Sibalic N, Keaveney J, Adams C S and Hughes I G 2017 *Physical Review Letters* **118** 253601

[102] Ripka F, Chen Y H, Löw R and Pfau T 2016 *Physical Review A* **93** 053429–

[103] Holloway C L, Gordon J A, Jefferts S, Schwarzkopf A, Anderson D A, Miller S A, Thaicharoen N and Raithel G 2014 *IEEE Transactions on Antennas and Propagation* **62** 6169–6182

[104] Holloway C L, Simons M T, Gordon J A, Dienstfrey A, Anderson D A and Raithel G 2017 *Journal of Applied Physics* **121** 233106

[105] Simons M T, Kautz M D, Holloway C L, Anderson D A, Raithel G, Stack D, St John M C and Su W 2018 *Journal of Applied Physics* **123** 203105

[106] Anderson D, Paradis E and Raithel G 2018/08/13 *Appl. Phys. Lett.* **113**

[107] Grimmel J, Mack M, Karlewski F, Jessen F, Reinschmidt M, Sándor N and Fortágh J 2015 *New Journal of Physics* **17** 053005

[108] Barredo D, Kübler H, Daschner R, Löw R and Pfau T 2013 *Phys. Rev. Lett.* **110** 123002

[109] Weller D, Shaffer J P, Pfau T, Löw R and Kübler H 2019 *Physical Review A* **99** 043418

[110] Anderson D A, Raithel G, Simons M and Holloway C L 2017 *arXiv* 1712.08717

[111] Weller D, Urvoy A, Rico A, Löw R and Kübler H 2016 *Physical Review A* **94** 063820

[112] Abel R P, Carr C, Krohn U and Adams C S 2011 *Physical Review A - Atomic, Molecular, and Optical Physics* **84** 023408

[113] Gallagher T F 1994 *Rydberg Atoms* (Cambridge: Cambridge University Press)

[114] Lee E S, Cho S, Lyeo H K and Kim Y H 2014 *Phys. Rev. Lett.* **112** 136601

[115] Muray J 2018 Photoelectric effect induced by high intensity laser light beam in quartz and borosilicate glass URL https://www.osti.gov/biblio/1444126-photoelectric-effect-induced-high-intensity-laser-light-be

[116] Holloway C L, Gordon J A, Simons M T, Fan H, Kumar S, Shaffer J P, Anderson D A, Schwarzkopf A, Miller S A, Thaicharoen N and Raithel G 2015 Atom-based rf electric field measurements: An initial investigation of the measurement uncertainties *2015 IEEE International Symposium on Electromagnetic Compatibility (EMC)* vol 2015-Septmber (National Institute of Standards and Technology (NIST), Electromagnetics Division, 325 Broadway, Boulder, CO 80305, United States: Institute of Electrical and Electronics Engineers Inc.) pp 467–472

[117] Fan H, Kumar S, Sheng J, Shaffer J P, Holloway C L and Gordon J A 2015 *Physical Review Applied* **4**

[118] Ritter R, Gruhler N, Dobbertin H, Kübler H, Scheel S, Pernice W, Pfau T and Löw R 2018 *Physical Review X* **8** 021032–

[119] Whittaker K A, Keaveney J, Hughes I G, Sargsyan A, Sarkisyan D and Adams C S 2015 *Physical Review A* **92** 052706

[120] Kübler H, Shaffer J P, Baluktsian T, Löw R and Pfau T 2010 *Nature Photonics* **4** 112–116

[121] Ma L, Anderson D A and Raithel G 2017 *Physical Review A* **95** 061804–

[122] Jackson J D 1998 *Classical Electrodynamics* 3rd ed (Wiley)

[123] Sedlacek J A, Kim E, Rittenhouse S T, Weck P F, Sadeghpour H R and Shaffer J P 2016 *Physical Review Letters* **116**

[124] Taĭchenachev A V, Tumaikin A M, Yudin V I, Stähler M, Wynands R, Kitching J and Hollberg L 2004 *Phys. Rev. A* **69**(2) 024501 URL https://link.aps.org/doi/10.1103/PhysRevA.69.024501

[125] Levi F, Godone A, Vanier J, Micalizio S and Modugno G 2000 *Eur. Phys. J. D (France)* **12** 53 – 9 ISSN 1434-6060 URL http://dx.doi.org/10.1007/s100530070042

[126] Figueroa E, Vewinger F, Appel J and Lvovsky A I 2006 *Opt. Lett.* **31** 2625–2627 URL http://ol.osa.org/abstract.cfm?URI=ol-31-17-2625

[127] Vanier J, Godone A and Levi F 1998 *Phys. Rev. A* **58**(3) 2345–2358 URL https://link.aps.org/doi/10.1103/PhysRevA.58.2345

[128] Erhard M and Helm H 2001 *Phys. Rev. A* **63**(4) 043813 URL https://link.aps.org/doi/10.1103/PhysRevA.63.043813

[129] Xiao Y, Novikova I, Phillips D F and Walsworth R L 2006 *Phys. Rev. Lett.* **96**(4) 043601 URL https://link.aps.org/doi/10.1103/PhysRevLett.96.043601

[130] Novikova I, Xiao Y, Phillips D and Walsworth R 2005 *J. Mod. Opt. (UK)* **52** 2381 – 90 ISSN 0950-0340 URL http://dx.doi.org/10.1080/09500340500275637

[131] Tang Y, Wen Y, Cai L and Zhao K 2020 *Phys. Rev. A* **101**(1) 013821 URL https://link.aps.org/doi/10.1103/PhysRevA.101.013821

[132] Safari A, De Leon I, Mirhosseini M, Magaña Loaiza O S and Boyd R W 2016 *Phys. Rev. Lett.* **116**(1) 013601 URL https://link.aps.org/doi/10.1103/PhysRevLett.116.013601

[133] Wang G, Wang Y S, Huang E K, Hung W, Chao K L, Wu P Y, Chen Y H and Yu I A 2018 *Scientific Reports* **8**

[134] Akulshin A, Celikov A and Velichansky V 1991 *Optics Communications* **84** 139 – 43 ISSN 0030-4018 URL http://dx.doi.org/10.1016/0030-4018(91)90216-Z

[135] Ye C Y and Zibrov A S 2002 *Phys. Rev. A* **65**(2) 023806 URL https://link.aps.org/doi/10.1103/PhysRevA.65.023806

[136] Iftiquar S M and Natarajan V 2009 *Phys. Rev. A* **79**(1) 013808 URL https://link.aps.org/doi/10.1103/PhysRevA.79.013808

[137] Sargsyan A, Vartanyan T and Sarkisyan D 2020 *Optics and Spectroscopy* **128** 12 ISSN 0030400X URL http://dx.doi.org/10.1134/S0030400X2001021X

[138] Javan A, Kocharovskaya O, Lee H and Scully M O 2002 *Phys. Rev. A* **66**(1) 013805 URL https://link.aps.org/doi/10.1103/PhysRevA.66.013805

[139] Lee H, Rostovtsev Y, Bednar C and Javan A 2003 *Appl. Phys. B, Lasers Opt. (Germany)* **B76** 33 – 9 URL http://dx.doi.org/10.1007/s00340-002-1030-5

[140] Taichenachev A, Tumaikin A and Yudin V 2000 *JETP Letters* **72** 119 URL http://dx.doi.org/10.1134/1.1316812

[141] Khan S, Kumar M, Bharti V and Natarajan V 2017 *Eur. Phys. J. D, At. Mol. Opt. Plasma Phys. (Germany)* **71** 38 (9 pp.) ISSN 1434-6060 URL http://dx.doi.org/10.1140/epjd/e2017-70676-x

[142] Thomas J E and Quivers W W 1980 *Phys. Rev. A* **22**(5) 2115–2121 URL https://link.aps.org/doi/10.1103/PhysRevA.22.2115

[143] Hughes I G 2018 *Journal of Modern Optics* **65** 640–647 (*Preprint* https://doi.org/10.1080/09500340.2017.1328749) URL https://doi.org/10.1080/09500340.2017.1328749

[144] Mølmer K, Castin Y and Dalibard J 1993 *J. Opt. Soc. Am. B* **10** 524–538 URL http://josab.osa.org/abstract.cfm?URI=josab-10-3-524

[145] Dalibard J, Castin Y and Mølmer K 1992 *Phys. Rev. Lett.* **68**(5) 580–583 URL https://link.aps.org/doi/10.1103/PhysRevLett.68.580

[146] Dalton B and Knight P 1982 *Optics Communications* **42** 411 – 416 ISSN 0030-4018 URL http://www.sciencedirect.com/science/article/pii/0030401882902772

[147] Dalton B J and Knight P L 1982 *Journal of Physics B: Atomic and Molecular Physics* **15** 3997–4015 URL https://iopscience.iop.org/article/10.1088/0022-3700/15/21/019

[148] Hockel D, Scholz M and Benson O 2009 *Appl. Phys. B, Lasers Opt. (Germany)* **94** 429 – 35 URL http://dx.doi.org/10.1007/s00340-008-3313-y

[149] Zhu M and Hall J L 1993 *J. Opt. Soc. Am. B* **10** 802–816 URL http://josab.osa.org/abstract.cfm?URI=josab-10-5-802

[150] Huss A, Lammegger R, Windholz L, Alipieva E, Gateva S, Petrov L, Taskova E and Todorov G 2006 *J. Opt. Soc. Am. B* **23** 1729–1736 URL http://josab.osa.org/abstract.cfm?URI=josab-23-9-1729

[151] Hafiz M, Maurice V, Chutani R, Passilly N, Gorecki C, Guerandel S, de Clercq E and Boudot R 2015 *J. Appl. Phys. (USA)* **117** 184901 ISSN 0021-8979 URL http://dx.doi.org/10.1063/1.4919841

[152] Lukin M D, Fleischhauer M, Zibrov A S, Robinson H G, Velichansky V L, Hollberg L and Scully M O 1997 *Phys. Rev. Lett.* **79**(16) 2959–2962 URL https://link.aps.org/doi/10.1103/PhysRevLett.79.2959

[153] Brazhnikov D, Coget G, Hafiz M, Maurice V, Gorecki C and Boudot R 2018 *IEEE Transactions on Ultrasonics, Ferroelectrics and Frequency Control* **65** 962 – 72 ISSN 0885-3010 URL http://dx.doi.org/10.1109/TUFFC.2018.2811319

[154] Barrett T D, Stuart D, Barter O and Kuhn A 2018 *New Journal of Physics* **20** ISSN 13672630 URL http://dx.doi.org/10.1088/1367-2630/aad14e

[155] Tremblay P, Michaud A, Levesque M, Thériault S, Breton M, Beaubien J and Cyr N 1990 *Phys. Rev. A* **42**(5) 2766–2773 URL https://link.aps.org/doi/10.1103/PhysRevA.42.2766

[156] Rostovtsev Y, Protsenko I, Lee H and Javan A 2020 *J. Mod. Opt. (UK)* **49** 2501 – 16 ISSN 0950-0340 URL http://dx.doi.org/10.1080/09500340210000011400

[157] HAPPER W 1972 *Rev. Mod. Phys.* **44**(2) 169–249 URL https://link.aps.org/doi/10.1103/RevModPhys.44.169

[158] Sekiguchi N and Hatakeyama A 2016 *Applied Physics B* **122**

[159] Xue Y, Hao L, Jiao Y, Han X, Bai S, Zhao J and Raithel G 2019 *Phys. Rev. A* **99**(5) 053426 URL https://link.aps.org/doi/10.1103/PhysRevA.99.053426

[160] Tanner C 1995 Precision measurements of atomic lifetimes 323 (USA) p 130 ISSN 0094-243X

[161] G W and DI P 1969 *Journal of Applied Physics* **40** 3946 – 3949 ISSN 00218979

[162] Madou M 2018 *Fundamentals of Microfabrication and Nanotechnology, Three-Volume Set* (CRC Press) ISBN 9781482274660 URL https://books.google.com/books?id=gPm7DwAAQBAJ

[163] Wei J, Wang Z P, Xie H and Ng Fern Lan 2002 Role of bonding temperature and voltage in silicon-to-glass anodic bonding *4th Electronics Packaging Technology Conference, 2002.* pp 85–90

[164] Berthold A, Nicola L, Sarro P and Vellekoop M 2000 *Sensors and Actuators, A: Physical* **82** 224 – 228 ISSN 09244247 URL http://dx.doi.org/10.1016/S0924-4247(99)00376-3

[165] Nichols C S, Nofs L M, Viray M A, Ma L, Paradis E and Raithel G 2020 *Phys. Rev. Applied* **14**(4) 044013 URL https://link.aps.org/doi/10.1103/PhysRevApplied.14.044013

[166] Arfken G 1985 *Mathematical Methods for Physicists* 3rd ed (San Diego: Academic Press, Inc.)